

ALMA MATER STUDIORUM · UNIVERSITÀ DI BOLOGNA

SCUOLA DI SCIENZE
Corso di Laurea in Astrofisica e Cosmologia
Dipartimento di Fisica e Astronomia

Radio Halos in a mass-selected sample of Galaxy Clusters

Tesi di Laurea Magistrale

Relatore:
Chiar.ma Prof.
Loretta Gregorini

Presentata da:
Virginia Cuciti

Co-relatori:
Dott.ssa Rossella Cassano
Dott.ssa Ruta Kale

Sessione III
Anno Accademico 2012-2013

This Thesis work was done as part of the research activity of the
Istituto di Radioastronomia - Istituto Nazionale di Astrofisica
(INAF) in Bologna.

Contents

List of Tables	9
List of Figures	11
List of Acronyms	13
Abstract	15
Introduction	17
1 Clusters of galaxies	21
1.1 Hierarchical formation of Galaxy Clusters	22
1.1.1 Linear theory of structure formation	22
1.1.2 Spherical collapse model	26
1.1.3 The mass function of DM halos	26
1.2 Emission from Galaxy Clusters	28
1.2.1 Optical properties	28
1.2.2 X-ray properties	29
1.2.3 The Sunyaev-Zel'dovich (SZ) effect	30
1.3 Estimate of the cluster mass	32
1.4 Clusters scaling relations	34
1.5 Cool-core vs. Merging clusters	36
1.5.1 Cool-core Clusters	36
1.5.2 Merging clusters	37
2 Non-thermal emission from Galaxy Clusters	39
2.1 Radio sources in Clusters of Galaxies	39
2.2 High energy emission from Galaxy Clusters	41
2.3 Non-thermal component in Galaxy Clusters	42
2.3.1 Magnetic field in Galaxy Clusters	42
2.3.2 Relativistic particles in the ICM	44
2.4 Models for the non-thermal emission of ICM	46
2.4.1 Secondary Models	47

2.4.2	The re-acceleration scenario	48
2.4.3	Mini-halos and Relics	50
3	A statistical model for the formation of Radio Halos	53
3.1	Cluster formation	56
3.2	Generation of turbulence during mergers	57
3.3	Particle acceleration by magneto-sonic waves	60
3.4	Occurrence of Radio Halos in Galaxy Clusters	63
3.4.1	Probability to form RHs as a function of clusters mass and redshift	63
3.4.2	Occurrence of RHs at different frequencies	66
4	Statistical properties of Radio Halos	71
4.1	The GMRT Radio Halo Survey	71
4.1.1	The Sample	72
4.1.2	Detections and Upper Limits	72
4.2	Main Results	76
4.2.1	Ultra Steep Specrum Radio Halos (USSRH)	76
4.2.2	$P_{1.4} - L_X$ correlation & bimodality of galaxy clusters	78
4.2.3	Occurrence of Radio Halos	81
4.2.4	Merger-Radio Halo connection	83
4.3	The Extended GRHS	86
4.4	Radio-SZ correlation & bimodality	87
5	Sample selection & data analysis	91
5.1	The Planck catalogue	92
5.2	The low redshift sample	94
5.3	The high redshift sample	98
5.4	Radio data analysis	101
5.4.1	Low-z sample	101
5.4.2	High-z sample	109
5.5	X-ray data analysis	113
5.6	The total sample	115
6	Results & Discussion	123
6.1	Occurrence of Radio Halos	123
6.2	Radio Halo-merger connection	128
7	Comparison with model expectations	137
7.1	Basic ingredients of the statistical model	137
7.2	How to derive f_{RH} from Monte Carlo calculations	138
7.3	Adopted parameters and procedures	140
7.4	Results & Discussion	141

Summary & Conclusions	145
Bibliography	150

List of Tables

5.1	Low redshift sample clusters properties	97
5.2	High redshift sample clusters properties	99
5.3	Clusters not included in the high-z sample	100
5.4	NVSS rms after the reprocessing	107
5.5	Total sample clusters properties	117
6.1	Occurrence of RHs in the low-z and high-z samples	125
6.2	Monte Carlo analysis	126
6.3	Clusters with no available Chandra data	132

List of Figures

1.1	Millennium Simulation	23
1.2	Growth factor	25
1.3	DM halos mass function	27
1.4	Coma Multi-Wavelength view	28
1.5	SZ effect	31
1.6	SZ effect in A2163	32
1.7	X-ray luminosity-mass correlation	34
1.8	SZ-mass correlation	36
2.1	A3667 relics	40
2.2	RXC J1504.1-0248 mini-halo	41
2.3	Cosmic Rays life-time	44
3.1	Statistical models main ingredients	55
3.2	Geometry of the merger	57
3.3	Evolution of the thermal energy	59
3.4	CRe spectrum	62
3.5	Expected RH spectra	64
3.6	Magnetic field constraints	65
3.7	Probability to form RHs in superlinear regime	67
3.8	Probability to form RHs in sublinear regime	67
3.9	Fraction of clusters with RHs with $\nu_s > \nu_o$	68
3.10	Fraction of clusters with RHs in different frequency ranges	69
4.1	A697 full resolution and tapered image	73
4.2	RXCJ 2003.5-2323, subtraction of individual sources	74
4.3	Upper Limits, injection of the fake RH	75
4.4	A521 image at 240, 610 MHz and 1.4 GHz.	76
4.5	A521 radio spectrum	77
4.6	$P_{1.4} - L_X$ diagram: <i>radio bimodality</i>	78
4.7	The GRHS sample	81
4.8	Comparison between observed f_{RH} and model expectations	82
4.9	Morphological parameters diagrams	85
4.10	$P_{1.4} - M_{500}$ plane: apparent lack of bimodality	88

4.11	Cool-core correction	89
4.12	$P_{1.4} - M_{500}$ and $P_{1.4} - Y_{500}$ correlations	90
4.13	$P_{1.4} - M_{500}$ plane: apparent lack of bimodality	90
5.1	Sample selection from the Planck catalogue	93
5.2	NVSS detection limit	96
5.3	A1451 radio-X-ray-optical images	102
5.4	NVSS sky coverage	103
5.5	A3888 NVSS map	104
5.6	Diffuse flux densities vs. control fields flux densities	105
5.7	Flux densities distributions	106
5.8	A3888 NVSS reprocessing	107
5.9	Diffuse flux densities vs. control fields average flux densities	109
5.10	Excess	110
5.11	A56	111
5.12	A1443	112
5.13	A1413: 1 Mpc circle extending over the Chandra CCD edges	114
5.14	Chandra CCD gaps	115
5.15	Gallery of Chandra X-ray images	122
6.1	Fraction of clusters with RHs as a function of M_{lim}	124
6.2	Monte Carlo calculations	127
6.3	Morphological diagrams for the low-z subsample	129
6.4	Morphological diagrams for the high-z subsample	130
6.5	Morphological diagrams for the total sample	131
6.6	$c - w$ in two mass bins	133
6.7	XMM-Newton images	135
7.1	Procedure to derive the expected f_{RH}	139
7.2	Formation probability of RHs	142

List of Acronyms

ACT: Atacama Cosmology Telescope
AIPS: Astronomical Image Processing System
AGN: Active Galactic Nuclei
BAT: Burst Alert Telescope
BCG: Brightest Cluster Galaxy
CCD: Charged-Coupled Device
CMB: Cosmic Microwave Background
CR: Cosmic Ray
DM: Dark Matter
eBCS: Extended ROSAT Brightest Cluster Sample
EdS: Einstein De Sitter
EGRET: Energetic Gamma Ray Experiment Telescope
EGRHS: Extended GMRT RH Survey
ESO: European Southern Observatory
FITS: Flexible Image Transport System
GC: Galaxy Cluster
GMRT: Giant Metrewave Radio Telescope
GRHS: GMRT RH Survey
GW: Galactic Wind
HEASARC: High Energy Astrophysics Science Archive Research
HL: High Luminosity
HM: High Mass
HST: Hubble Space Telescope **HXR:** Hard X-Ray
IC: Inverse-Compton
ICM: Intra-Cluster Medium
IR: Infra-Red
LAT: Large Area Telescope
LL: Low Luminosity
LM: Low Mass
LOFAR: Low Frequency Array
MH: Mini-Halo
MHD: Magneto-Hydro Dynamic
MS: Magneto-Sonic

MWA: Murchison Widefield Array
NORAS: Northern Rosat All Sky
NRAO: National Radio Astronomy Observatory
NVSS: NRAO VLA Sky Survey
NuSTAR: Nuclear Spectroscopic Telescope Array
PS: Press-Schechter
PSZ: Plack-SZ catalogue
RASS: ROSAT All-Sky Survey Bright Source
REFLEX: ROSAT-ESO Flux Limited X-ray
RM: Rotation Measure
RH: Radio Halo
ROSAT: Röntgensatellit
RXTE: Rossi X-ray Timing Explorer
SDSS: Sloan Digital Sky Survey
SN: Supernovae
SZ: Sunyaev-Zel'dovich
TTD: Transit Time Damping
UL: Upper Limit
USSRH: Ultra Steep Spectrum Radio Halo
VLA: Very Large Array
XBACs: X-Ray Brightest Abell-type Clusters
XMM: X-ray Multi-Mirror Mission
WENSS: Westerbork Northern Sky Survey **WSRT:** Westerbork Synthesis Radio Telescope

Abstract

Osservazioni nella banda radio rivelano l'esistenza di emissione diffusa su scale di ~ 1 Mpc in un certo numero di ammassi di galassie in fase di merger. Queste sorgenti estese, chiamate aloni radio, sono dovute ad emissione di sincrotrone da parte degli elettroni relativistici spiraleggianti nei campi magnetici del mezzo intracluster, e testimoniano quindi la presenza di componenti non-termiche mischiate col gas termico del mezzo stesso. L'origine degli aloni radio è ancora oscura. Gli elettroni relativistici che emettono in banda radio hanno tempi di vita radiativi ordini di grandezza più piccoli di quelli necessari per ricoprire, attraverso processi di diffusione, le scale tipiche da cui proviene l'emissione diffusa. Gli elettroni non possono quindi essere semplicemente iniettati dalle galassie presenti negli ammassi; è necessario un meccanismo di accelerazione "in-situ" su scale del Mpc. La connessione tra gli aloni radio e i mergers tra ammassi, ha stimolato la nascita del modello di riaccelerazione da turbolenza. In base a questo modello, gli elettroni relativistici, iniettati negli ammassi da galassie/AGN (i cosiddetti elettroni primari) e/o dalle collisioni tra protoni termici e protoni cosmici (i cosiddetti secondari), sono successivamente riaccelerati dalla turbolenza MHD generata nel mezzo intracluster durante gli eventi di merger, fino alle energie necessarie per emettere radiazione di sincrotrone nella banda radio. La quantità di energia disponibile per l'accelerazione degli elettroni relativistici è fornita dall'energia gravitazionale del merger. Nell'ambito di questo scenario la probabilità di formazione di un alone radio dipende dalla massa dell'ammasso e dall'energetica del merger. Ci si aspetta quindi che la frazione di ammassi con alone cresca al crescere della massa degli ammassi e che gli aloni radio siano presenti solo in ammassi in fase di merger.

Lo scopo di questa Tesi è stato quello di calcolare la frazione di ammassi con alone radio, f_{RH} , in un campione di ammassi selezionato in massa e con osservazioni radio, e di confrontare questi risultati con le attese del modello di riaccelerazione da turbolenza. In particolare, ci siamo proposti di studiare la frazione di ammassi con alone radio in funzione della massa degli ammassi e di analizzare la connessione tra la presenza degli aloni e lo stato dinamico degli ammassi. A tale scopo abbiamo selezionato, dal "Planck-SZ catalogue" (PSZ), ammassi di galassie con $M \gtrsim 6 \times 10^{14} M_{\odot}$ a redshift $0.08 < z < 0.33$ e abbiamo investigato la presenza/assenza di aloni radio in questi ammassi utilizzando la survey radio NVSS, per gli ammassi a $z < 0.2$, e l'estensione della "GMRT Radio Halo Survey" (EGRHS),

per gli ammassi a $z > 0.2$. Il campione totale risulta così composto da 54 ammassi di galassie, 23 dei quali ospitano un alone radio. Abbiamo anche ridotto e analizzato i dati in banda X ottenuti dal satellite Chandra, per 44 ammassi, con lo scopo di ricavare informazioni sul loro stato dinamico.

Per derivare l'andamento di f_{RH} in funzione della massa degli ammassi, abbiamo diviso il campione in due intervalli di massa: l'intervallo a bassa massa ($M < M_{lim}$) e quello ad alta massa ($M > M_{lim}$). Abbiamo calcolato f_{RH} nei due intervalli di massa per diversi valori di M_{lim} e abbiamo trovato $f_{RH} \approx 20 - 30\%$ nell'intervallo a bassa massa e $f_{RH} \approx 60 - 80\%$ in quello ad alta massa. Attraverso simulazioni Monte Carlo, abbiamo determinato il valore di M_{lim} che massimizza il rapporto di f_{RH} calcolato nei due intervalli di massa e la sua significatività statistica. Questo valore è $M_{lim} = 8 \times 10^{14} M_{\odot}$, per il quale si ottiene $f_{RH} = 30 \pm 9\%$ nell'intervallo a bassa massa e $f_{RH} = 79 \pm 24\%$ in quello ad alta massa. La probabilità che il crollo di f_{RH} nel bin a bassa massa sia casuale è $< 8 \times 10^{-4}$, che corrisponde ad una significatività statistica del nostro risultato del $\sim 3.2\sigma$.

Facendo uso di codici statistici sviluppati nell'ambito del modello di riaccelerazione, abbiamo derivato l'evoluzione teorica della frazione di ammassi con alone in funzione della massa degli ammassi e abbiamo confrontato queste predizioni con i valori osservati di f_{RH} nei due intervalli di massa. Le nostre osservazioni risultano in accordo con le previsioni teoriche del modello di riaccelerazione, suggerendo che la crescita osservata di f_{RH} con la massa degli ammassi è conseguenza del fatto che l'efficienza dell'accelerazione di particelle è più alta in ammassi massicci che subiscono episodi di merger energetici.

Infine, facendo uso dei dati Chandra, abbiamo analizzato lo stato dinamico degli ammassi del nostro campione e abbiamo trovato, in accordo con studi precedenti, che gli ammassi con alone radio sono in fase di merger, mentre la maggior parte degli ammassi che non mostrano emissione diffusa sono dinamicamente rilassati. Questo risultato evidenzia il ruolo fondamentale degli eventi di merger tra ammassi di galassie nella formazione degli aloni radio.

Introduction

Galaxy clusters are the largest gravitationally bound systems in the Universe. In the hierarchical framework of structure formation they form through accretion of matter and merging between smaller units. A fraction of the energy dissipated during these mergers is channelled into the acceleration of relativistic particles and into the amplification of the magnetic field. The bulk of the information on the non-thermal components in galaxy clusters comes from radio observations, Radio Halos (RH) are indeed the most spectacular evidence of the non-thermal phenomena in the Intra Cluster Medium (ICM). RHs are diffuse Mpc-scale synchrotron sources observed at the centre of a number of merging galaxy clusters. Still, their origin is unclear. According to the most favourite view, RHs trace turbulent regions in the ICM where particles are trapped and accelerated during cluster mergers. This scenario has clear expectations about the statistical properties of RHs, in particular, it predicts that the fraction of clusters with RHs, f_{RH} , increases with the cluster mass, thus RHs should be found in massive/merging clusters, should be rare in smaller merging systems and absent in relaxed systems. To test these expectations large complete samples of galaxy clusters, with adequate information about their mass, redshift and dynamical status and with adequate radio data (to determine the presence/absence of diffuse radio emission) are necessary.

In this context, this Thesis work is aimed at providing an unbiased measure of the fraction of clusters hosting RHs and of its dependence on the cluster mass, in a nearly complete mass-selected sample of galaxy clusters. With this goal in mind, we selected, from the Planck SZ catalogue clusters with $M \gtrsim 6 \times 10^{14} M_{\odot}$ in the redshift range $z = 0.08 - 0.33$ and we searched for the presence of RHs in the radio survey NVSS (plus literature information) for clusters at $z < 0.2$ and in the Extended GMRT RH Survey (EGRHS) for $0.2 < z < 0.33$. We also used the Chandra X-ray data, available for most of the clusters in the sample, to investigate their dynamical status.

Here we provide a brief summary of what is reported in the following Chapters.

- In **Chapter 1** we give a description of the general properties of galaxy clusters: the paradigm of hierarchical structure formation, the properties of the thermal ICM, from X-ray to SZ observations, the derivation of basic scaling relations and the different methods to estimate the cluster mass.

- In **Chapter 2** we review the non-thermal emission from galaxy clusters from both an observational and theoretical point of view. We provide a multi-wavelength description of the non-thermal phenomena in the ICM and we describe the different forms of diffuse radio emission (RHs, relics and mini-halos). Two main models have been proposed for the origin of RHs: (i) the turbulent re-acceleration model, in which relativistic particles are re-accelerated by the turbulence injected during cluster mergers, and (ii) the secondary electrons model, where relativistic electrons are secondary products of the hadronic interaction between Cosmic Rays (CR) and thermal protons. In this Chapter we briefly describe these models and report also on problems and advantages of both.
- In **Chapter 3** we summarize the main steps of the statistical calculations developed in the framework of the turbulent re-acceleration model, that actually provides a powerful tool to interpret current data and to make predictions for further observations.
- In **Chapter 4** we review the principal observational results of the statistical properties of RHs, with particular reference to the EGRHS, which led to the discovery of the bimodality of galaxy clusters in the radio-X-ray and radio-SZ diagrams and also allowed to highlight the connection between RHs and merging clusters. We also critically report on the recent attempts to estimate the occurrence of RHs in mass-selected samples of galaxy clusters. We introduce the aim of the Thesis work that is to provide an unbiased view of the occurrence of RHs in clusters as a function of the cluster mass and compare these results with the theoretical expectations derived from the turbulent re-acceleration scenario.
- In **Chapter 5** we introduce the sample of clusters we selected from the Planck SZ catalogue, with $M \gtrsim 6 \times 10^{14} M_{\odot}$ and at $0.08 < z < 0.33$. We describe the radio data analysis carried out during the Thesis work, on both NVSS and VLA pointed datasets, in order to derive information on the presence of diffuse emission for those clusters without literature information. We also report on the Chandra X-ray data analysis we performed to get information on the dynamical status of clusters. Finally, we define our total sample of 54 galaxy clusters, 23 of which host RHs, that will be used in the next Chapters to derive the statistical properties of RHs.
- In **Chapter 6** we derive the fraction of clusters with RHs, f_{RH} , as a function of the cluster mass. We split our sample into two mass bins, the low mass bin (LM, $M < M_{lim}$) and the high mass bin (HM, $M > M_{lim}$) and we make use of a Monte Carlo based procedure to determine the value of M_{lim} that maximizes the ratio of f_{RH} between the two mass bins. Furthermore, the same Monte Carlo analysis procedure allows to test the statistical validity of

our result. We also report on the morphological analysis of the clusters with available Chandra X-ray data.

- In **Chapter 7** we use a Monte Carlo statistical procedure to derive the theoretical evolution of f_{RH} with the cluster mass in the framework of the turbulent re-acceleration scenario. We compare these expectations with our observational results.
- Finally, we provide a general discussion on the Thesis work, highlighting its main conclusions and giving also some prospects for future studies, that will complete and expand our understanding of non-thermal phenomena in galaxy clusters.

Chapter 1

Clusters of galaxies

Clusters of galaxies are the largest structures in the present Universe in which gravitational force due to the matter overcomes the expansion of the Universe. They extend over 1 – 3 Mpc regions and have typical total masses of the order $10^{15} M_{\odot}$, mostly in the form of dark matter (DM $\sim 70 - 80\%$). Barionic matter is in the form of galaxies (\sim few %) and especially in the form of hot ($T = 10^8\text{K}$) and tenuous ($n_{gas} \sim 10^{-1} - 10^{-4}\text{cm}^{-3}$) gas ($\sim 15 - 20\%$), the intra-cluster medium (ICM).

Galaxy clusters have been first discovered in the optical band, essentially because they contain large concentration of galaxies, first catalogues were indeed based on the visual inspection of photographic plates (e.g. Abell 1958). Clusters of galaxies contain about 50 up to hundreds of galaxies, that move with typical velocity dispersion of the order of $\sigma_v \sim 1000$ km/s. The crossing time for a cluster of size R can be estimated as:

$$t_{cr} = \frac{R}{\sigma_v} \simeq \left(\frac{R}{1\text{Mpc}} \right) \left(\frac{10^3\text{km/s}}{\sigma_v} \right) \text{Gyr} \quad (1.1)$$

Therefore, in a Hubble time (13.7 Gyr), such a system has enough time to dynamically relax, at least in its central ~ 1 Mpc, condition that cannot be achieved in the surrounding ~ 10 Mpc environment.

Assuming virial equilibrium, the typical cluster mass results:

$$M \simeq \frac{R\sigma_v^2}{G} \simeq \left(\frac{R}{1\text{Mpc}} \right) \left(\frac{\sigma_v}{10^3\text{km/s}} \right)^2 10^{15} M_{\odot} \quad (1.2)$$

First optical studies based on Eq. 1.2, noted that the mass implied by the motion of galaxies within the cluster exceeded (about a factor of ~ 10) the sum of the masses of all visible galaxies, providing the first evidence of the presence of dark matter (Zwicky 1933, 1937; Smith 1936). Nowadays indeed it is well known that the 70 – 80% of the cluster mass is in form of DM.

1.1 Hierarchical formation of Galaxy Clusters

Being the largest bound systems in the Universe, galaxy clusters provide excellent probes of structure formation and can be used to constrain cosmological models. According to the hierarchical model of structure formation, galaxy clusters are supposed to form by accretion of smaller units (galaxies, groups etc.). In the current cosmological framework the gravitational field is dominated by the DM component and thus the first non linear systems to form, by gravitational collapse, are dark matter halos. Luminous objects are thought to form by cooling and condensation of baryons within the gravitational potential well created by the DM halos (White & Rees 1978).

The physical properties of galaxy clusters, such as the fraction of dynamically young clusters, the luminosity and temperature functions, the radial structure of both dark and barionic matter, constitute a challenging test for our understanding of how these objects grow from primordial density fluctuations.

There are different ways to model the cosmic structure formation: analytic, semi-analytic and numerical techniques. The analytic techniques were first developed in the '70 years and pose the basis of the present models for structure formation (White & Rees 1978, Fall & Efstathiou 1980). The semi-analytic techniques (Cole 1991; White & Frenk 1991; Kauffmann et al. 1993; Cole et al. 1994) are based on the model of the gravitational clustering developed by Press & Schechter (1974) and its extensions (Bower 1991; Bond et al. 1991; Lacey & Cole 1993). This formalism is extensively used to build up, via Monte Carlo calculations, synthetic populations of DM halos which evolve with time due to mergers and hierarchical clustering. Numerical methods allow a detailed study of the relevant physical processes and of the matter distribution on different scales (Davis et al. 1985; Steinmetz & Muller 1995; Katz et al. 1996, Springel et al. 2006). They are the unique instrument to describe the non-linear evolution of the perturbations (Fig. 1.1).

1.1.1 Linear theory of structure formation

Observations of the Cosmic Microwave Background (CMB) radiation show that the Universe at the recombination epoch ($z \simeq 1300$) was extremely uniform, but also show the presence of spatial fluctuation in the energy density and gravitational potential of roughly one part in 10^5 (Bennet et al. 1996). The gravitational instability can be summarized as follows: starting from an homogeneous and isotropic fluid, small fluctuations in density, $\delta\rho$, and velocity, δv , can grow with time if the self-gravitating force overcomes the pressure force. This condition is satisfied wherever the typical lengthscale of the fluctuations is greater than the Jeans lengthscale, λ_j of the fluid.

There are two different regimes of growth of the perturbations: linear and non linear; they can be distinguished defining the density fluctuation, or the overdensity:

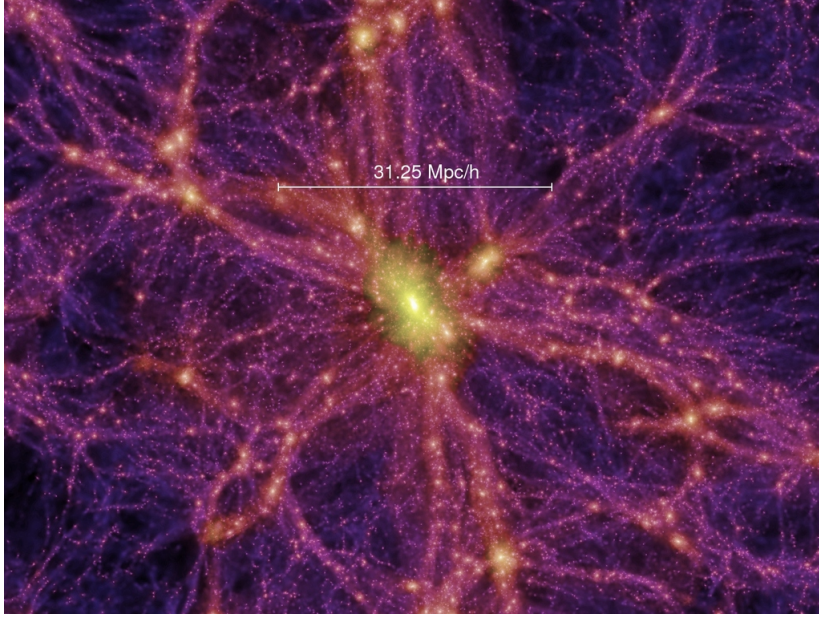


Figure 1.1: The Millennium Simulation: a slice through the density field of the DM at $z=0$ ($t=13.6$ Gy) (Springel et al. 2006).

$$\delta = \frac{\rho - \bar{\rho}}{\bar{\rho}} = \frac{\delta\rho}{\bar{\rho}} \quad (1.3)$$

where ρ is the density of the Universe at a given position and $\bar{\rho}$ in the mean unperturbed density of the Universe. The linear regime acts as long as $\delta \ll 1$. In the linear regime the growth of the perturbation can be described with the Jeans theory, who first demonstrated that small density fluctuations in an homogeneous, isotropic and stationary fluid can grow with time, become unstable and collapse. To describe the evolution of a self-gravitating fluid we can use the continuity, the Euler and the Poisson equations (e.g. Coles & Lucchin 1995):

$$\frac{\partial\rho}{\partial t} + \vec{\nabla} \cdot (\rho\vec{v}) = 0 \quad (1.4)$$

$$\frac{\partial\vec{v}}{\partial t} + (\vec{v} \cdot \vec{\nabla})\vec{v} + \frac{1}{\rho}\vec{\nabla}p + \vec{\nabla}\phi = 0 \quad (1.5)$$

$$\nabla^2\phi - 4\pi G\rho = 0 \quad (1.6)$$

where p and ϕ are the pressure and the gravitational potential. To attempt to understand how the density evolves with time, we start from an unperturbed, uniform and static fluid, with density $\rho = \rho_0 = \text{const}$; we expand these equations for the perturbed quantities ($\rho_0 + \delta\rho, v + \delta v$ and so on) and linearize them to search for solutions in the form of plane waves, we obtain:

$$\ddot{\delta}_k = (4\pi G\rho_0 - c_s^2 k^2)\delta_k \quad (1.7)$$

where k is the wave number and c_s is the sound speed. The solution of Eq. 1.7 is an harmonic oscillator with dispersion equation:

$$\omega^2 = v_s^2 - 4\pi G\rho_0 \quad (1.8)$$

Defining the Jeans length scale as:

$$\lambda_j = c_s \sqrt{\frac{\pi}{G\bar{\rho}}} \quad (1.9)$$

and:

$$k_j = \frac{2\pi}{\lambda_j} \quad (1.10)$$

we have two kinds of solution:

- perturbations with $\lambda < \lambda_j$ ($k > k_j$), produce positive ω^2 and we have the standard propagation of sound waves;
- perturbations with $\lambda > \lambda_j$ ($k < k_j$) produce negative ω^2 and their growth (which depends on the geometry of the Universe) yields a growing and a decaying mode.

We can consider the expansion of the Universe including a variable background density $\rho_0 = \rho_0(t_0)a^{-3(t)}$, where a is the scale factor of the Universe. The linearization yields to:

$$\ddot{\delta}_k + 2\frac{\dot{a}}{a}\dot{\delta}_k + (c_s^2 k^2 - 4\pi G\rho_0)\delta_k = 0 \quad (1.11)$$

For an Einstein-de Sitter (EdS) Universe one has:

$$\bar{\rho} = \frac{1}{6\pi G t^2} \quad (1.12)$$

$$a = a_0 \left(\frac{t}{t_0}\right)^{2/3} \quad (1.13)$$

$$\frac{\dot{a}}{a} = \frac{2}{3t} \quad (1.14)$$

and Eq. 1.11 has two possible solutions: $\delta_+ \propto t^{2/3} \propto a$ and $\delta_- \propto t^{-1} \propto a^{-2/3}$, for the growing and the decaying mode respectively.

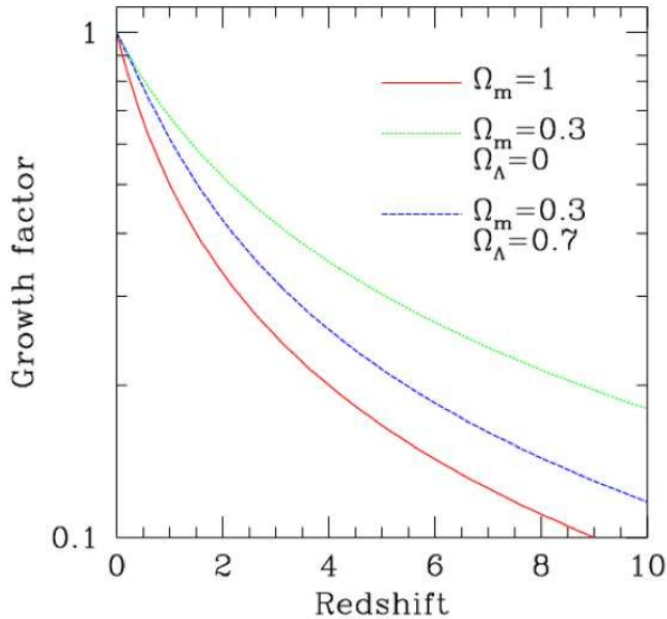


Figure 1.2: The redshift dependence of the linear growth factor of perturbations for an EdS model $\Omega_m = 1$ (solid curve), for a flat $\Omega_m = 0.3$ model with a cosmological constant (dashed curve) and for an $\Omega_m = 0.3$ open model with vanishing the cosmological constant (Borgani 2008).

It is worth introducing the linear growth factor $D(z)$ that gives the growth of fluctuations (normalized to the present epoch) as a function of the redshift z . In the EdS Universe $D(z) = \frac{1}{1+z} = (\frac{t}{t_0})^{2/3} \propto a$. In the Λ CDM model ($\Omega_m \neq 1, \Omega_\Lambda \neq 0$) an useful approximation formula for $D(z)$ is given by (e.g. Carrol et al. 1992):

$$D(z) = \frac{1}{(1+z)} \frac{g(z)}{g(z=0)} \quad (1.15)$$

where $g(z)$ is:

$$g(z) = \frac{5}{2} \Omega_m(z) \left[\Omega_m(z)^{4/7} - \Omega_\Lambda(z) + \left(1 + \frac{\Omega_m(z)}{2}\right) \left(1 + \frac{\Omega_\Lambda(z)}{70}\right) \right]^{-1} \quad (1.16)$$

Fig. 1.2 shows $D(z)$ for an EdS model ($\Omega_m = 1$) and for a Λ CDM model ($\Omega_m = 0.3, \Omega_\Lambda = 0.7$). It is evident that in an Einstein-de Sitter Universe the evolution is faster (i.e. $D(z)$ is steeper), while in a Λ CDM model the evolution is less rapid due to the fact that at some point the cosmic expansion takes place at a quicker rate than the gravitational instability, and this freezes the perturbation growth. The relations described in this section remain valid until the perturbation δ becomes of the order of the unity, at that point non-linear effects become important and the linear theory cannot be applied any more.

1.1.2 Spherical collapse model

Once the strongly non-linear regime ($\delta \gg 1$) is reached (a cluster of galaxies for example corresponds to δ of the order of several hundred), it is necessary to develop techniques for studying the non-linear evolution of perturbations. A simplified way to describe the evolution of structures in the non-linear regime is the spherical collapse model which follows the evolution of a spherically symmetric perturbation with constant density.

At the initial time the perturbation expands with the background Universe. At a given time, t_m , the perturbation ceases to expand and begins to collapse. From the spherical collapse model one finds that the density of the perturbation at t_m is $\rho_p(t_m) \approx 5.6\rho(t_m)$ for an EdS Universe.

For $t > t_m$ the perturbation collapses, the formation of shocks and pressure gradients, which convert some of the kinetic energy of the collapse into heat, leads to a final virial equilibrium state at $t_V \approx 2t_m$ with radius R_V and mass M_V related by the following equation:

$$R_V = \left[\frac{3M_V}{4\pi\Delta_V(z)\bar{\rho}(z)} \right]^{1/3} \quad (1.17)$$

where $\bar{\rho}(z) = 2.78 \times 10^{11} \Omega_m (1+z)^3 h^2 M_\odot \text{ Mpc}^{-3}$ is the mean mass density of the Universe at redshift z and $\Delta_V(z)$ is the overdensity at virial equilibrium computed with respect to the background density. In an EdS Universe the quantity $\Delta_V(z) = 18\pi^2 = 178$, while in the Λ CDM cosmology $\Delta_V(z)$ depends on z and it's given by Kitayama & Suto (1996):

$$\Delta_V(z) = 18\pi^2 (1 + 0.4093\omega(z))^{0.9052} \quad (1.18)$$

where $\omega(z) \equiv \Omega_f(z)^{-1} - 1$ with:

$$\Omega_f(z) = \frac{\Omega_{m,0}(1+z)^3}{\Omega_{m,0}(1+z)^3 + \Omega_\Lambda} \quad (1.19)$$

1.1.3 The mass function of DM halos

To follow the hierarchical evolution of a population of DM halos that undergo a spherical collapse, semi-analytical techniques, as those developed by Press & Schechter (1974) and Lacey & Cole (1993), are necessary. In the Press-Schechter (PS) theory galaxy clusters form via mergers of substructures, which develop by gravitational instability of initial small density fluctuations generated in the early Universe. According to the PS theory, the clusters mass function at a given redshift is:

$$N(M)dM = \sqrt{\frac{2}{\pi}} \frac{\bar{\rho}}{M} \frac{\delta_c(z)}{\sigma^2} \frac{d\sigma}{dM} \exp\left(-\frac{\delta_c(z)^2}{2\sigma^2}\right) dM \quad (1.20)$$

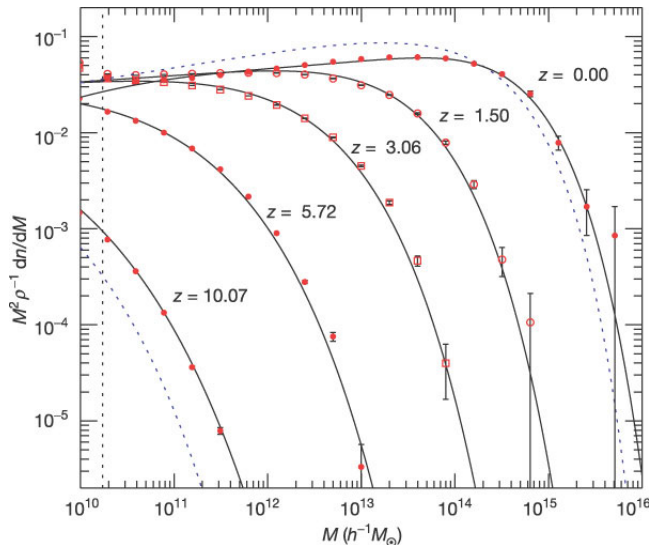


Figure 1.3: Mass function of DM halos of the Millennium simulation at different redshifts (Springel et al. 2005). Solid lines are predictions from an analytic fitting function, the dashed lines represent the Press-Schechter model.

where $\bar{\rho}$ is the median mass density of the Universe at redshift z and $\delta_c(z)$ is the critical linear overdensity for a region to collapse at that redshift, for an EdS Universe is

$$\delta_c(t) = \frac{3(12\pi)^{2/3}}{20} \left(\frac{t_0}{t}\right)^{2/3} \quad (1.21)$$

$\sigma(M)$ is the standard deviation of matter density fluctuations. An useful approximation for $\sigma(M)$ can be obtained in the case of a power-law spectrum of the perturbations (Randall, Sarazin & Ricker 2002):

$$\sigma(M) = \sigma_8 \left(\frac{M}{M_8}\right)^{-\alpha} \quad (1.22)$$

where σ_8 is the present epoch rms density fluctuation on a scale of $8h^{-1}$ Mpc and $M_8 = \frac{4\pi}{3}(8h^{-1}\text{Mpc})^3\bar{\rho}$.

Fig 1.3 shows the comparison between the number density of DM halos given by numerical simulations (Springel et al. 2005) and that derived from the PS model (dashed lines) at different redshifts. One can note some deviations of the PS mass function from the numerical results: the former slightly overestimates the number of halos in the low-mass range, while it underestimates the abundance of halos in the high mass tail. Such discrepancies are believed to be due to the PS approach, which doesn't account for the effects of non-spherical collapse.

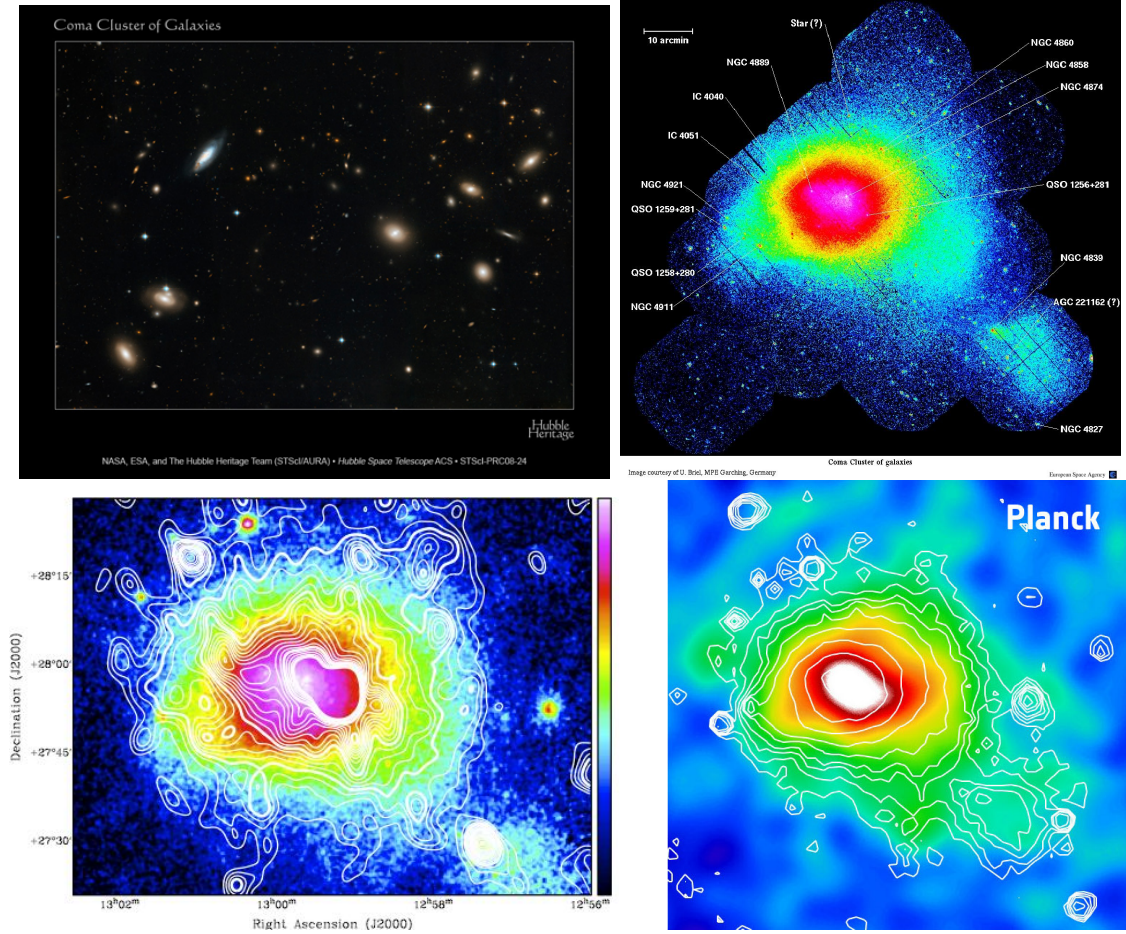


Figure 1.4: Multi-frequency view of the Coma cluster: the optical emission from galaxies in the central region (left top panel, HST); the thermal ICM emitting in the X-rays (right top, XMM-Newton); synchrotron radio emission (contours) overlaid on the X emission (left bottom panel, 350 MHz WSRT map) and the overlay between the thermal SZ signal (colors) and X-ray (contours) (bottom right, Planck Satellite).

1.2 Emission from Galaxy Clusters

In this section we give a brief multiwavelength description of galaxy clusters, focusing mainly on the emission mechanisms generated by the galaxies and by the thermal ICM. A multiwavelength view of the Coma cluster is shown in Fig. 1.4.

1.2.1 Optical properties

Galaxies are not uniformly distributed on the sky, rather they are concentrated in large overdensities, as revealed by optical observations of galaxy clusters. Several studies have been undertaken, since the second half of the last century, to detect and classify galaxy clusters. Abell (1958; 1965) carried out the first catalogue

of galaxy clusters detecting several thousand of them through visual inspection of optical plates from the Palomar All-Sky Survey. This catalogue has been then expanded to include clusters from the southern hemisphere (ACO catalogue, Abell et al. 1989). Abell also introduced a first classification based on the cluster richness, i.e. the approximate number of galaxies composing the cluster. This was estimated as the background-corrected number of galaxies within a projected radius of $R_a = 1.5h^{-1}\text{Mpc}$ (the so-called Abell radius) and with magnitude in the interval $m_3 < m < m_3 + 2$ where m_3 is the observed magnitude of the third most luminous galaxy in the cluster region. Clusters were divided into six “richness group” that goes from “Group 0” (30-49 galaxies) to “Group 5” (more than 299 galaxies).

Abell clusters are typically in the local Universe ($z < 0.2$), with some very bright members up to $z \sim 0.4$. Abell also divided clusters of galaxies in:

- regular: evolved, virialized, symmetric systems;
- irregular: dynamically disturbed objects, showing asymmetric morphology with the presence of substructures.

Zwicky (1961-1968) proposed a classification based on the cluster apparent shape on the plates. Depending on the number of galaxies in apparent contact, clusters are thus classified as compact, partly compact or open.

Another interesting classification was suggested by Bautz & Morgan (1970), based on the dominance of the Brightest Cluster Galaxy (BCG):

- Type I: dominated by a single dominant very bright galaxy (cD);
- Type II: the brightest galaxy is a giant elliptical galaxy;
- Type III: have multiple BCGs or non detectable BCG.

Any kind of optical classification tries to link in some way the cluster with its mass, assuming that the more rich a cluster is, the largest is its mass. Indeed, the mass of a cluster is the most desirable parameter by which to classify clusters, thus defining complete mass-selected catalogues and samples is of fundamental importance. However, if redshift data are not available in large numbers, a direct link between mass and richness is difficult to establish.

1.2.2 X-ray properties

Clusters of galaxies were detected clearly as bright X-ray sources since the first high-energy experiments successfully detected X-ray sources in the sky. In 1966, for the first time, X-ray radiation from a region surrounding M87 (the central galaxy of the Virgo cluster) was detected, by means of X-ray balloons. After that, X-ray sources were found to be associated also with the Perseus and the Coma clusters.

In the '70 years the Uhuru satellite allowed to build up the first all sky survey in X-ray band, which revealed that the majority of galaxy clusters are X-ray luminous objects, with X-ray luminosities $L_X \sim 10^{43} - 10^{45}$ erg/s. This emission comes from the Intra Cluster Medium (ICM): a hot ($T \sim 10^8$ K), optically thin, ionised plasma with mean density $n_e \sim 10^{-3} - 10^{-4}$ cm $^{-3}$. If the ICM, permeating the cluster potential well, shares the same dynamics as member galaxies, then it is expected to have a typical temperature:

$$K_B T \simeq \mu m_p \sigma_v^2 \simeq 6 \left(\frac{\sigma_v}{10^3 \text{ km/s}} \right)^2 \text{ keV} \quad (1.23)$$

where m_p is the proton mass and μ is the mean molecular weight. X-ray observations actually confirm this relation, despite some scatter, which indicates that the idealised picture of clusters as relaxed systems where both gas and galaxies feel the same dynamics is a simplified, but reasonable, description.

The ICM emits primarily via thermal bremsstrahlung; the emissivity for this process at frequency ν is:

$$\epsilon_\nu \propto n_e n_i g(\nu, T) T^{1/2} \exp(-h\nu/k_B T) \quad (1.24)$$

where n_e and n_i are the number density of electrons and ions, respectively and $g(\nu, T) \propto \ln(k_B T/h\nu)$ is the Gaunt factor. The spectral shape of the emissivity $\epsilon_\nu(r)$ provides a measure of $T(r)$, while its normalization gives a measure of n_e . Since bremsstrahlung emission is basically proportional to the squared density of the ICM, clusters of galaxies clearly stand out as X-ray sources in the sky. For systems with $T > 3$ keV the pure bremsstrahlung emissivity is a good approximation, while for lower temperature line emission becomes more relevant (essentially because not all the heavy nuclei are completely ionised at that temperature).

1.2.3 The Sunyaev-Zel'dovich (SZ) effect

The ICM is a hot and ionised gas, thus it contains extremely energetic electrons. When photons from the Cosmic Microwave Background (CMB) radiation encounter these electrons, they can undergo the Inverse Compton (IC) effect: the ‘‘cold’’ photon gains energy by interacting with the ‘‘hot’’ electron and hence it increases in frequency and it is blue-shifted. In practice, only about 1% of the CMB photons undergoes IC scattering as it passes through the cluster gas.

The Sunyaev-Zel'dovich (SZ) effect is a small distortion of the CMB spectrum caused by the IC scattering of the CMB photons with the energetic ICM electrons. The SZ effect appears as a decrease in the CMB intensity at frequencies lower than ~ 218 GHz and as an increase at higher frequencies (Fig. 1.5). The observed spectral distortion of the CMB spectrum by the SZ effect is shown in Fig. 1.6.

The Compton y -parameter is defined as:

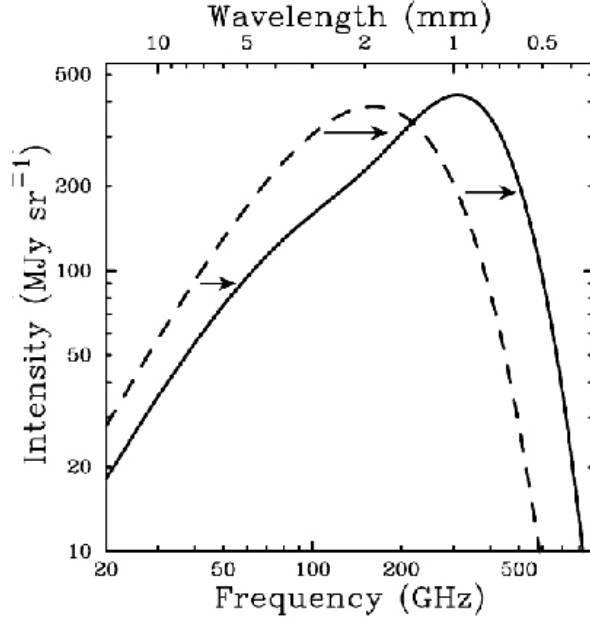


Figure 1.5: Standard CMB spectrum (dashed line) and distorted by the SZ effect (solid line). The SZ effect determines a decrease in intensity at low frequencies ($\nu < 218\text{GHz}$) and an increase at high frequencies (Carlstrom et al. 2002). This is a schematic representation: the actual distortion is much smaller.

$$y \propto \int_0^{\infty} n_e T_e dl \quad (1.25)$$

where n_e and T_e are the electron density and temperature and the integration is taken along the line of sight. Expressed in unit of intensity, the SZ effect can be written as:

$$\Delta I_{SZ} \propto I_0 y \quad (1.26)$$

where I_0 is the CMB intensity unaffected by the IC scattering. A peculiar characteristic of the SZ effect is that it is independent on redshift, as show by the combination of Eq. 1.26 and 1.25.

Integrating the y -parameter over the solid angle Ω subtended by the cluster, one obtains the integrated Compton parameter, that corresponds to the CMB intensity decrement due to the SZ effect:

$$\text{SZ flux} \propto Y \equiv \int_{\Omega} y d\Omega \propto \frac{1}{D_A^2} \int_0^{\infty} dl \int_A n_e T_e dA \quad (1.27)$$

where A is the area of the cluster in the plane of the sky and D_A is the angular diameter distance.

Another crucial characteristic of the SZ effect is its correlation with the cluster

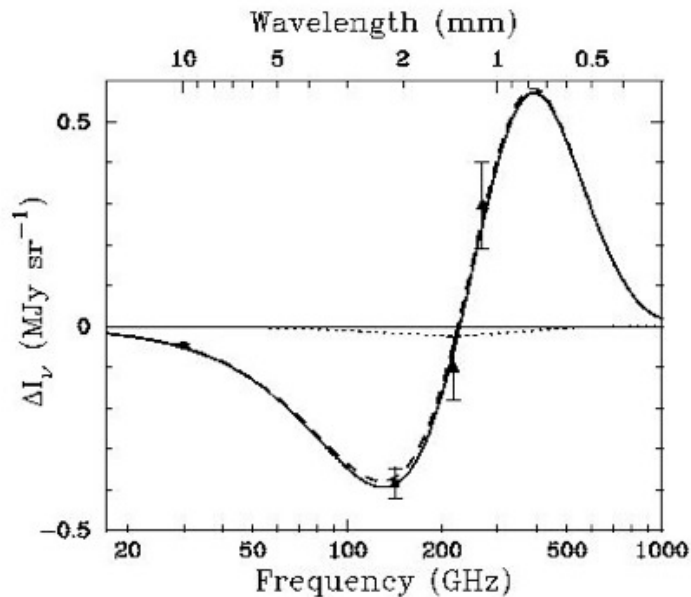


Figure 1.6: The measured SZ effect in A2163 (Carlstrom et al. 2002).

mass, due to the fact that the SZ signal integrated over the solid angle of the cluster provides the sum of the electrons weighted by temperature (Eq. 1.27), which is a measure of the total thermal energy of the cluster. We will give details on the SZ effect-cluster mass correlation in Sec. 1.4.

1.3 Estimate of the cluster mass

From an historical point of view, the dynamics traced by member galaxies has been the first method applied to measure masses of galaxy clusters (Smith, 1936; Zwicky, 1937). Under the assumption of virial equilibrium, the mass of the cluster can be estimated by knowing the position and redshift for a high enough number of member galaxies (see also Eq. 1.2):

$$M \propto \frac{3\sigma_v^2 R_V}{G} \quad (1.28)$$

where σ_v is the galaxies velocity dispersion along the line of sight and R_V is the virial radius, which depends on the positions of the galaxies (recognised as true cluster members) with measured redshifts.

The condition of hydrostatic equilibrium determines the balance between the pressure force and gravitational force: $\nabla P_{gas} = -\rho_{gas} \nabla \phi$, where P_{gas} and ρ_{gas} are the gas pressure and density and ϕ is the gravitational potential. Under the assumption

of spherically symmetric gas distribution, the previous equation becomes:

$$\frac{dP_{gas}}{dr} = -\rho_{gas} \frac{d\phi}{dr} = -\rho_{gas} \frac{GM(< r)}{r^2} \quad (1.29)$$

where r is the radial coordinate (i.e. the distance from the cluster centre) and $M(< r)$ is the mass contained within r . Thus, using the equation of state of ideal gas to relate pressure to gas density and temperature, $P = (K_B \rho T) / \mu m_p$, the mass is given by:

$$M(< r) = \frac{r K_B T}{G \mu m_p} \left(\frac{d \ln \rho_{gas}}{d \ln r} + \frac{d \ln T}{d \ln r} \right) \quad (1.30)$$

where μ is the mean molecular weight of the gas and m_p is the proton mass. A common way to describe the gas density profile is assuming the β model (Cavaliere & Fusco-Femaino 1976):

$$\rho_{gas}(r) = \frac{\rho_0}{[1 + (r/r_c)^2]^{3\beta/2}} \quad (1.31)$$

where r_c is the core radius and $\beta = \mu m_p \sigma_v^2 / (k_B T)$. If we assume the gas to be isothermal, the combination of Eq. 1.31 and 1.30 gives:

$$M(< r) = \frac{3 K_B T r^3 \beta}{\mu m_p G} \left(\frac{1}{r^2 + r_c^2} \right) \quad (1.32)$$

A third independent method to estimate the cluster mass is based on weak and/or strong gravitational lensing, i.e. on the images of distant objects that result distorted by the gravitational potential of the cluster. A simple spherical lensing model provides a good estimate of the cluster mass within the radius r_{arc} which is the distance between the arc-like image and the cluster centre (e.g. Bartelmann 2003):

$$M_{lens}(< r_{arc}) \approx \pi r^2 \Sigma_{crit} \quad (1.33)$$

where

$$\Sigma_{crit} = \frac{c^2}{4\pi G} \frac{D_S}{D_{LS} D_L} \quad (1.34)$$

D_L , D_{LS} and D_S are the distances from the observer to the lens, from the lens to the source and from the observer to the source, respectively. Observations of weak lensing aim at reconstructing the cluster mass distribution from the weak ellipticity that the cluster gravity induces on faint background galaxies. This method is made difficult by the fact that galaxies are intrinsically elliptic, therefore it requires several source images to be averaged, under the assumption of random orientation of these sources.

1.4 Clusters scaling relations

The simplest model to explain the physics of the ICM is by assuming that gravity only determines the thermodynamical properties of the hot diffuse gas (Kaiser et al. 1986). Since gravity doesn't have preferred scales, it is expected that clusters of different sizes are scaled version of each other. In this sense the ICM model, based on the effect of gravity only, is said to be *self-similar*. The existence of scaling

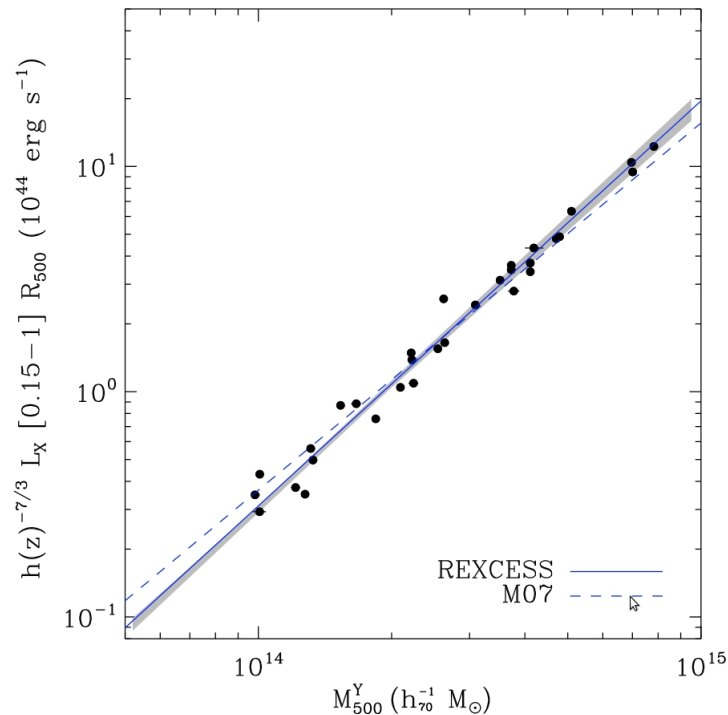


Figure 1.7: $L_X - M_{500}$ relation for emission in the $[0.15-1]R_{500}$ aperture, for the REXCESS sample (Pratt et al. 2009).

relations between different global properties, such as mass, velocity dispersion of the galaxies, X-ray luminosity, and temperature, proves that different components (gas and galaxies) experiment the same approximate dynamical equilibrium inside the gravitational potential well of the cluster.

In order to establish relationships between mass, SZ effect, L_X and other cluster properties, one needs to define a radius out to which all quantities will be calculated. The best physical candidate is the virial radius, unfortunately it is usually unreachable with current X-ray and SZ measurements, so one is forced to perform measurements on smaller radii. Here we decide to use R_{500} which is defined as the radius within which the average density is 500 times the critical density at the cluster redshift, $\rho_{cr} = \frac{3H(z)^2}{8\pi G}$.

Assuming that only gravity determines the hot gas thermodynamical properties

(Kaiser, 1986), one can derive the relation between the total mass M and the gas temperature kT , starting from the virial equilibrium $\frac{3kT}{2\mu m_p} = \frac{GM}{R}$:

$$kT = 3.23 \left(\frac{\mu}{0.6}\right) \left(\frac{\delta}{500}\right)^{1/3} \left(\frac{M}{10^{14}h^{-1} M_{\odot}}\right)^{2/3} \text{ keV} \quad (1.35)$$

where δ is the mean overdensity of the cluster with respect to the critical density of the Universe.

Assuming $n_e = n_{ion} \equiv n = \frac{f_{gas}\rho}{\mu m_p}$, where f_{gas} is the fraction of mass in form of ICM and ρ is the total mass density of the cluster, we can write the X-ray luminosity as:

$$L_X = 1.33 \times 10^{43} \left(\frac{f_{gas}}{0.1h^{-3/2}}\right)^2 \left(\frac{0.6}{\mu}\right) \left(\frac{n}{10^{-3}h^2\text{cm}^{-3}}\right) \left(\frac{T}{\text{keV}}\right)^{0.4} \times \\ \times \left(\frac{M}{10^{14}h^{-1} M_{\odot}}\right) h^{-2} \text{ erg s}^{-1} \quad (1.36)$$

Eq. 1.36 shows the relation between the X-ray luminosity and the total mass of clusters. For this reason X-ray observations have been of fundamental importance: they represent a tool for the determination of the cluster mass, which is the principal parameter of theoretical models concerning the formation and the evolution of galaxy clusters. Fig. 1.7 shows the correlation between the X-ray luminosity and the mass of galaxy clusters from Pratt et al. (2009).

Finally, there is a tight correlation between the SZ effect and the cluster mass. Indeed, in the context of an isothermal model, the integrated Compton parameter, Y , can be written as:

$$Y_{500} D_A^2 \propto T_e \int n_e dV = M_{gas} T_e = f_{gas} M_{tot} T_e \quad (1.37)$$

Including Eq. 1.35 in Eq. 1.37 we find a correlation between the integrated Compton parameter and the cluster mass:

$$Y_{500} D_A^2 \propto f_{gas} M_{tot}^{5/3} E(z)^{2/3} \quad (1.38)$$

with $E^2(z) = \Omega_{m0}(1+z)^3 + \Omega_{\Lambda} + \Omega_{k0}(1+z)^2$. Fig. 1.8 demonstrates the existence of this correlation from an observational point of view, thus confirming that the Compton parameter can be used as a proxy of the cluster mass.

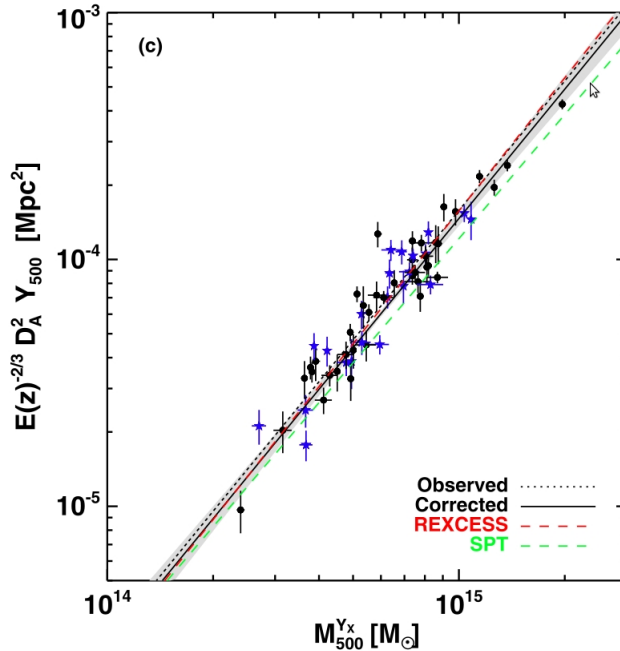


Figure 1.8: $Y_{500} - M_{500}$ scaling relation for the 62 clusters in the Planck-XMM-Newton archive sample (Planck collaboration 2011).

1.5 Cool-core vs. Merging clusters

X-ray observations reveal that galaxy clusters show a variety of morphologies, connected to the cluster dynamical status. We can identify two main extreme cases: Cool-core clusters, which are relaxed clusters with very peaked X-ray emission at their centres, and merging clusters, characterised by irregular morphologies and the presence of substructures in their X-ray brightness distributions. In this Section we will briefly describe the main characteristics of these two classes of objects.

1.5.1 Cool-core Clusters

As we discussed in Sec. 1.2.2, the ICM primarily loses energy via thermal bremsstrahlung, emitting X-ray radiation. The cooling time-scale for this process can be defined as $t_{cool} = (d \ln T / dt)^{-1}$; if the gas cools isobarically, the cooling time is (Sarazin, 1986):

$$t_{cool} \simeq 8.5 \times 10^{10} \left[\frac{n_p}{10^{-3} \text{cm}^{-3}} \right]^{-1} \left[\frac{T}{10^8 \text{k}} \right]^{1/2} \text{ [yr]} \quad (1.39)$$

which is longer than the Hubble time. However the bremsstrahlung emissivity depends on the square of the gas density (Eq. 1.24), which rises towards the cluster centre, implying that in some cases t_{cool} becomes $< 10^{10}$ yr in the central 100 kpc or so. In absence of any balancing heating, as the gas cools it is compressed by the

surrounding ICM, further increasing its X-ray emissivity. To balance the pressure from the overlying ICM, slow inflow of gas, known as “cooling” flow were expected. X-ray based observations (e.g. Fabian 1994) seemed to be consistent with the cooling flow picture until the advent of Chandra and XMM-Newton, that have substantially changed the cooling flow scenario. As a matter of fact, there is clear evidence that the gas temperature drops by a factor of ~ 3 (down to 2-3 keV) in the central 100 kpc region, but the gas does not appear to flow towards the centre and to be piling up at lower temperature, rather the gas temperature profile seems to be frozen, and it seems to have been so for some Gyrs (e.g. Bauer et al. 2005). This suggests the presence of a continuous central source of heating, at least on time scales of 10^8 yr. Some mechanism of heating may balance radiative cooling, but the source of heating is still unsolved. Several candidates have been proposed: Supernovae (e.g. Domainko et al. 2004), AGNs (e.g. Fabian et al 2002; Bîrzan et al 2004), Thermal conduction (e.g. Voigt et al. 2002, Cho et al. 2003). Nowadays the term “cooling flow” has been replaced by the term “cool-core” that better indicates those clusters where the gas temperature drops sharply in the centre. Some cool-core clusters show holes in the X-ray surface brightness, coincident with radio lobes (e.g. Fabian et al. 2005), which are commonly referred to as radio bubbles. They are interpreted as bubbles of relativistic gas blown by the AGN into the thermal ICM and they have been considered evidence of the heating mechanisms driven by the central radio source and propagating through the ICM.

1.5.2 Merging clusters

ROSAT and ASCA observations revealed, for the first time, that many clusters show evidence of the accretion of smaller masses and other undergo major mergers of two nearly equal component (e.g. Briel et al. 1991; Böhringer et al. 1994; Markevitch et al. 1999; Henriksen et al. 2000). Major cluster mergers are energetic events in which clusters collide at velocities of ~ 2000 km/s. Merger-driven shocks pass through the ICM and dissipate energies of $\sim 3 \times 10^{63}$ erg. The angular resolution of Chandra has provided further insight into the merging process, revealing for the first time the unequivocal signature of a few shock fronts in clusters of galaxies (Markevitch et al, 2005, 2006).

The kinematics of an individual binary merger collision can be simply described by imaging two subclusters with mass M_{max} and M_{min} that merge at some time t_m after having fallen together from a large distance d_0 . It can be assumed that the subclusters are point masses and their radial velocity was zero at the largest separation d_0 . The collapse can be treated as the orbit of two point masses and their largest separation is given by the third Kepler’s law:

$$d_0 \simeq (2G(M_{max} + M_{min}))^{1/3} \left(\frac{t_m}{\pi} \right)^{2/3} \quad (1.40)$$

As the centres of the two subclusters reach a distance of the order of the virial radius of the most massive cluster, R_{max} , the relative impact velocity is given by:

$$v_i \simeq (2G(M_{max} + M_{min}))^{1/2} \left(\frac{1}{R_{max}} - \frac{1}{d_0} \right)^{1/2} \left[1 - \left(\frac{b}{d_0} \right)^2 \right]^{-1/2} \quad (1.41)$$

where b is the impact parameter. In the simplest case of central collision ($b = 0$):

$$v_i \simeq \left[2G \frac{(M_{max} + M_{min})}{R_{max}} \left(1 - \frac{1}{\eta_v} \right) \right]^{1/2} \quad (1.42)$$

where $\eta_v \simeq 4 \left(\frac{M_{max} + M_{min}}{M_{max}} \right)^{1/3}$. Eq. 1.42 will be used to calculate the impact velocity between clusters in Chapter 3.

The virial theorem implies that the square of the thermal velocity (sound speed) of the ICM scales with the gravitational potential. During a merger, since the infalling subclusters are driven by the gravitational potential, the velocity of the infall should be $\sim 1.5 - 2$ the sound speed of the main cluster. Consequently, motions in cluster mergers are expected to be moderately supersonic. Shocks thus represents the imprint of merging events in galaxy clusters and their study is of fundamental importance. Semi-analytical calculations (Gabici & Blasi 2003) and cosmological simulations (e.g. Pfrommer et al. 2006) of merger driven shocks in the hierarchical scenario of structure formation show that the bulk of the shocks in galaxy clusters should have Mach number $M = v_s/c_s \sim 1.5$.

Chapter 2

Non-thermal emission from Galaxy Clusters

There is now firm evidence that non-thermal components, magnetic field and relativistic particles, are present in the ICM. Although Radio Halos are the most spectacular evidence of the non-thermal phenomena acting in the ICM, non-thermal emission is also expected at higher energy (Hard-X-ray and γ -ray).

2.1 Radio sources in Clusters of Galaxies

The detection of diffuse radio emission (i.e Radio Halos, relics and mini-halos) in a growing number of galaxy clusters reveals the presence of relativistic particles and magnetic field extending throughout the cluster volume. They open fundamental questions about their origin as well as their impact on both the physics of the ICM and the evolution of galaxy clusters. It is nowadays well established that halos and relics are strictly connected to the cluster formation history, therefore our understanding of their origin and evolution is not only relevant itself, but it represents a crucial issue to understand the mechanisms at play during the process of structure assembly.

Radio Halos (RH) are large diffuse non-thermal radio sources permeating the cluster center which are not associated with any single galaxy, but rather with the diffuse ICM. RHs are Mpc-scale synchrotron emitting regions located at the cluster centres; they exhibit a fairly regular morphology, in good spatial coincidence with the distribution of the hot X-ray emitting gas. RHs have typical luminosity of $\sim 5 \times 10^{23} - 5 \times 10^{25} h^{-2}$ Watt/Hz at 1.4 GHz. Their emission is unpolarised, or at most, they have very low polarised emission (<10%). RHs are low surface brightness radio sources ($\sim \mu\text{Jy}/\text{arcsec}^2$ at 1.4 GHz) and they show steep radio spectra ($\alpha \approx 1.2 - 1.3$ with $J(\nu) \propto \nu^{-\alpha}$); these characteristics, plus their large angular dimension, make RHs very difficult to detect.

The prototype of this class of sources and the best studied one is Coma C (Fig. 1.4,

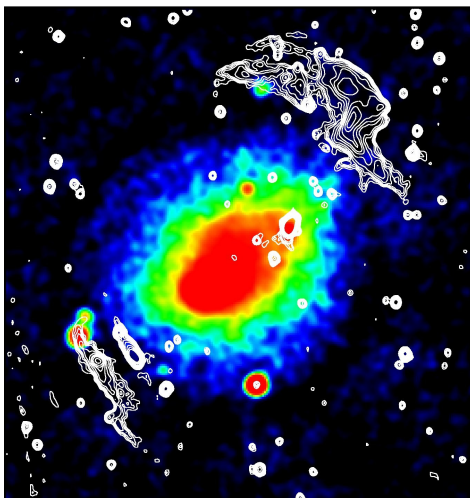


Figure 2.1: 20 cm ATCA contours of A3667 overlaid with the ROSAT image (Röttgering et al. 1997).

bottom left panel) in the Coma cluster (Willson 1970; Schlickeiser et al. 1987; Kim et al. 1990; Giovannini et al. 1993; Deiss et al. 1997; Thierbach et al. 2003).

Relics are similar to RHs in the low surface brightness, large size, luminosity and steep spectrum, but they show a variety of morphologies (the most common are elongated or arc-shaped) and are located at the cluster periphery. Furthermore, Relics are generally linearly polarised at a level of $\sim 10 - 30\%$ at 1.4 GHz (e.g. Giovannini & Feretti 2004).

A spectacular example of two almost symmetric relics in the same cluster can be found in A3667 (Röttgering et al. 1997), showed in Fig. 2.1. It is worth mentioning that, in some clusters, both RHs and relics have been detected, e.g. Coma, A2255, A2256, A1300, A2744 and RXC J1314.4-2515.

Mini-halos are diffuse extended radio sources of moderate size ($\lesssim 500h^{-1}\text{kpc}$) surrounding a dominant powerful radio galaxy at the cluster centre. One could think they are related to the central radio source, but mini-halos do not appear as extended symmetric lobes maintained by an AGN, therefore the presence of relativistic particles and magnetic field at the cluster center is necessary to explain their existence.

Example of this class of objects are found in Perseus (Burns et al. 1992; Sijbring 1993) and Virgo (Owen et al. 2000) and in the recently studied cluster RXC J1504.1-0248 (Giacintucci et al. 2011) which is presented in Fig. 2.2.

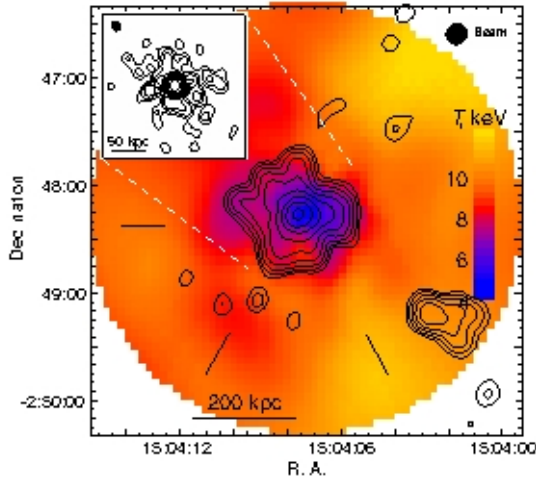


Figure 2.2: GMRT 327 MHz contours of the mini-halo in RXC J1504.1-0248 overlaid on the gas temperature map (Giacintucci et al. 2011).

2.2 High energy emission from Galaxy Clusters

Non-thermal high energy emission from galaxy clusters is an unavoidable consequence of the presence of CRe in the ICM. Standard mechanism for the production of high energy photons in the ICM are bremsstrahlung from supra-thermal and primary CRe, IC of seed photons from primary and secondary electrons and the decay of π^0 generated by p-p collisions (see Sec. 2.3.2). Furthermore the CRe produced by the interaction between ultra-high-energy CRs and ambient CRp should produce both synchrotron and IC emission at high energies. In this Section we discuss the current observational constraints and future prospects in the field of the high energy emission from galaxy clusters.

Hard X-ray emission

Thermal emission dominates in the ICM in the keV energy range, however it declines rapidly at higher energies, allowing to detect non-thermal emission at energies >10 -20 keV. IC scattering of CMB photons and supra-thermal bremsstrahlung are expected to be the most important mechanisms responsible for Hard X-ray emission in galaxy clusters (Sarazin 1999; Blasi 2000, Petrosian et al. 2008).

Hard X-rays have been claimed for the Coma cluster by Rephaeli & Gruber (1999, 2002) with the Rossi X-ray Timing Explorer (RXTE) and by Fusco-Femiano et al. (1999, 2004) with BeppoSAX. More recently, Wik et al. (2011) performed a joint analysis of 58-months Swift Burst Alert Telescope (BAT) and XMM-Newton spectrum derived from mosaic observation of Coma and found no evidence for IC emission at the level expected from previous detections.

Actually, there is no compelling evidence for a detection of Hard X-ray emission

from the ICM with current instruments.

Hopefully, in the next years the detector on-board on NuSTAR and ASTRO-H will allow to solve the current controversies, with improving the sensitivity in the Hard X-ray band by more than one order of magnitude with respect to present facilities.

Gamma-ray emission

The interest in γ -ray emission from galaxy clusters arose from the possibility of significant confinement of CRp in the ICM (see Sec. 2.3.2). A natural byproduct of the CRp confinement is the emission of γ -ray radiation from the decay of π^0 and the IC scattering with CMB photons by high energy of secondary electrons. In the last decade numerical simulations have provided useful estimates of the expected γ -ray emission from galaxy clusters, they predict that clusters would be potentially detectable in γ -ray by Fermi-LAT telescope (Miniati 2001, 2003; Pfrommer 2008). Subsequent simulations have attempted to reconcile expectations with the limits from 18 months observations with Fermi-LAT (Aleksić et al. 2010; Pzinke et al. 2010, 2011). However, most recent limits, derived from 5 years of Fermi-LAT data, are definitely inconsistent with the prediction of these simulations (The Fermi-LAT Collaboration: Ackermann et al. 2013; Huber et al. 2013).

Actually, no detection of galaxy clusters in γ -ray have been obtained so far.

2.3 Non-thermal component in Galaxy Clusters

The RH radiation coming from a number of galaxy clusters can only be due to synchrotron emission of relativistic electrons in the ICM. Consequently, to understand the origin and the evolution of these sources, it is necessary to know how Cosmic Rays and magnetic fields are connected to the cluster dynamics and evolution.

2.3.1 Magnetic field in Galaxy Clusters

The existence of a magnetic field associated with the ICM in galaxy clusters is now well established by means of different methods, which essentially lead typical field strength of the order of $\approx \mu\text{G}$. Since the magnetic pressure in galaxy clusters is about one or two order of magnitude below the thermal gas pressure, magnetic fields are not dynamically important, but in all clusters they have a significant effect on energy transport in the ICM (Sarazin 1986; Tribble 1989) and relevant implications for the life-times of relativistic particles in the ICM.

Even though there is no compelling reason why one should expect the magnetic field to be in equipartition, the equipartition condition is frequently assumed in literature to estimate the magnetic field intensity from the observed radio emission, giving $\langle B \rangle \sim 0.1 - 1\mu\text{G}$. For a few clusters it has been possible to estimate the magnetic field strength through the observation of hard-X-ray (HXR) emission that, if

interpreted as the outcome of IC scattering of relativistic electron on CMB photons, implies $\langle B \rangle \sim 0.2 - 0.4 \mu\text{G}$ (Fusco-Femiano et al. 1999; Rephaeli et al. 1999).

Additionally, Faraday rotation measure (RM) of several moderately extended background and embedded synchrotron sources, distributed across an area comparable or larger than the cluster core, have been computed, with typical resulting central ICM magnetic field values $B_0 \sim 1\text{--}few \mu\text{G}$, and even larger in cool-core clusters (Vogt & Enßlin 2005; Govoni et al. 2006; Vacca et al. 2012; Bonafede et al. 2013). The ICM magnetic field seems to have a radial profile similar to that of the gas density, studies based on radio emission, as well as RM, indeed indicate that its strength declines with radius (Dolag et al. 2001; Murgia et al. 2004; Guidetti et al. 2008; Bonafede et al. 2010).

Physical processes responsible for the origin of the magnetic field in galaxy clusters are still poorly understood. The combination of relatively “high” (μG level) magnetic field with its complex topology requires a non-linear amplification of the ICM field, which probably happens during the process of cluster formation. Still a seed magnetic field to be amplified is required in galaxy clusters. Three main classes of models have been proposed to explain the origin of this seed field:

- I) magnetic fields are assumed to be produced “locally” and at relatively low redshift ($z \sim 2 - 3$) by the ejecta of galaxies (e.g. Völk & Atoyan 2000) or AGNs (e.g. Furlanetto & Loeb 2001).
- II) The seed is produced at higher redshift, before galaxy cluster formation, then it is amplified by the adiabatic compression of the gas, driven by accretion of structures.
- III) The third scenario assumes that merger-driven shocks, produced by the hierarchical structure formation process, give rise to small electric currents which may generate magnetic fields (Kulsrud et al. 1997; Ryu et al. 1998).

All the proposed models for the origin of the seed field require a following amplification process to reproduce the principle properties of the observed magnetic fields. Several simulations about the amplification processes have been carried out (Röttiger et al. 1999; Dolag et al. 1999, 2002, 2004; Brüggen et al. 2005). These studies demonstrate that amplification occurs in principle during accretion processes and merging events (Birk et al. 1999), therefore the final value of the magnetic field in clusters of galaxies strongly depends on their merging history. In particular, higher the cluster mass (meaning that they have undergone more energetic and numerous merger events) higher the magnetic field (Dolag et al. 1999, 2005b). Simulations predict a median magnetic field $\langle B \rangle$ scaling with temperature as $\langle B \rangle \propto T^\alpha$ with $\alpha \approx 2$ (Dolag et al. 2002, 2005b).

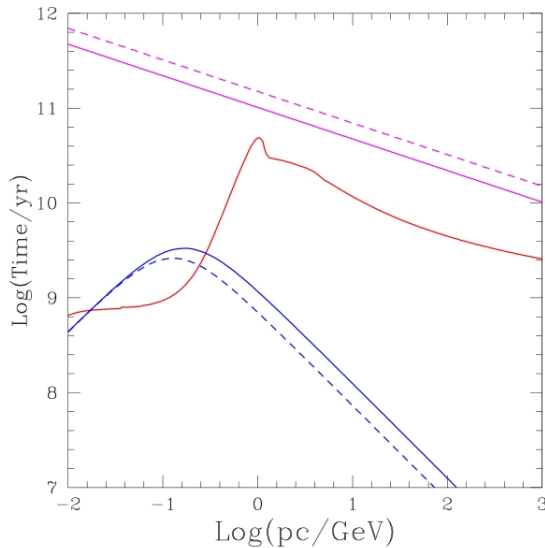


Figure 2.3: Life-time of CRp (red) and CRe (blue) in the ICM at $z=0$, compared with the CR diffusion time on Mpc scales (magenta). The magnetic field is $1\mu\text{G}$ (solid line) and $3\mu\text{G}$ (dashed line) (Blasi et al. 2007).

2.3.2 Relativistic particles in the ICM

Consensus has been reached in the past decade that shocks produced during the hierarchical formation of large scale structure in the Universe are likely sources of cosmic rays (CR) in galaxy clusters (e.g. Ryu et al. 2003), thus implying a direct connection between the generation of CRs and the formation and evolution of the hosting cluster.

Several additional sources can inject relativistic particles populations (electron, hadrons or both) into the ICM. For instance, particles can be accelerated in ordinary galaxies as an outcome of supernovae (SN) and then expelled into the ICM. Alternatively high velocity outflows from AGNs may supply the ICM with a large amount of energy in CRs and magnetic field (Enßlin et al. 1997). Powerful galactic wind (GW) at high redshift can also inject particles and magnetic field in the Intra Cluster Medium (Völk & Atoyan 1999).

Apart from the specific scenario of injection, relativistic particles are subject to energy losses that limit their life-time and the maximum energy at which they can be accelerated by acceleration mechanisms.

The energy losses of ultra-relativistic electrons (CRe) in the ICM are essentially dominated by ionization and Coulomb losses at low energies (Sarazin 1999):

$$\left[\frac{dp}{dt} \right]_i = -3.3 \times 10^{-29} n_{th} \left[1 + \frac{\ln(\gamma/n_{th})}{75} \right] \quad (2.1)$$

where n_{th} is the number density of the thermal plasma, and by synchrotron and IC losses at higher energies:

$$\left[\frac{dp}{dt} \right]_{rad} = -4.8 \times 10^{-4} p^2 \left[\left(\frac{B_{\mu G}}{3.2} \right)^2 + (1+z)^4 \right] \quad (2.2)$$

where $B_{\mu G}$ is the magnetic field strength in units of μG and isotropic magnetic fields and distribution of CRe momenta are assumed. The factor inside square brackets can be also expressed as $B_{IC}^2 + B^2$, where $B_{IC} = 3.2(1+z)^2 \mu G$ is the equivalent magnetic field strength for energy losses due to IC with CMB photons.

Defining the life-time of CRe as $\tau_e \sim \frac{p}{dp/dt}$, from Eq. 2.1 and 2.2 we obtain:

$$\tau_e(\text{Gyr}) \sim 4 \times \left\{ \frac{1}{3} \left(\frac{\gamma}{300} \right) \left[\left(\frac{B_{\mu G}}{3.2} \right)^2 + (1+z)^4 \right] + \left(\frac{n_{th}}{10^{-3}} \right) \left(\frac{\gamma}{300} \right)^{-1} \left[1.2 + \frac{1}{75} \ln \left(\frac{\gamma/300}{n_{th}/10^{-3}} \right) \right] \right\}^{-1} \quad (2.3)$$

This depends on the number density of the thermal medium, that can be estimated from X-ray observations, on the IC-equivalent magnetic field (i.e. the redshift of the cluster) and on the magnetic field strength, that is important only in the case $B^2 \gg B_{IC}^2$ and can be constrained from Faraday rotation measures.

Cosmic Rays protons (CRp) lose energy mainly through inelastic p-p collisions. This sets a CRp life-time:

$$\tau_{pp} \simeq \frac{1}{cn_{th}\sigma_{pp}} \quad (2.4)$$

where σ_{pp} is the inclusive p-p cross section (Dermer, 1986).

Fig. 2.3 shows the (total) time-scales for losses of CRe and CRp. CRp with energy 1 GeV-1 TeV are long-living particles with life-times in the core of galaxy clusters of several Gyrs. At higher energy the CRp time-scale gradually drops below 1 Gyr, while at very high energy, in the regime of ultra high energy CRp, the life-time is limited by inelastic collisions between CRp and CMB photons.

CRe instead are short-living particles at the energies where they emit observable radiation, due to unavoidable IC and synchrotron losses. The maximum life-time of CRe (~ 1 Gyr) is reached at energies ~ 100 MeV, where radiative losses are roughly equivalent to Coulomb losses. On the other hand, CRe with energy \sim several GeV that emit synchrotron radiation in the radio band (GHz), have shorter life-times, ~ 0.1 Gyrs. The CRe life-time for weak magnetic fields is determined by the unavoidable IC losses due to the scatter with the CMB photons, so that at high energies it doesn't vary much from cluster core to periphery. On the contrary, CRe IC life-times will scale strongly and inversely with cluster redshift according to $(1+z)^{-4}$ (Eq. 2.3, 2.2).

All the particles having escape times longer than the cluster life-time, which can

be assumed to be a fraction of the Hubble time ($t \sim 5 - 10$ Gyr) remain trapped within the cluster volume. For most of the CRp in the ICM both the time-scales of energy losses and diffusion out of the cluster is larger than the Hubble time (Berezinsky et al. 1997; Völk et al. 1996); as a consequence, once injected in the ICM, protons should remain confined and accumulate in the ICM during the cluster life-time. This confinement enhances the probability of having inelastic p-p collisions, implying that the generation of secondary particles due to inelastic collision between CRp and thermal protons in the ICM is an important source of CRe.

The decay chain for the injection of secondary particles is (Blasi & Colafrancesco 1999):

$$\begin{aligned}
 p + p &\longrightarrow \pi^0 + \pi^+ + \pi^- + \text{anything} \\
 \pi^0 &\longrightarrow \gamma\gamma \\
 \pi^\pm &\longrightarrow \mu^\pm + \nu_\mu \quad \mu^\pm \longrightarrow e^\pm \nu_\mu \nu_e
 \end{aligned}$$

2.4 Models for the non-thermal emission of ICM

The main difficulty in explaining the extended RHs arises from the combination of their Mpc size and the relative short radiative lifetime of the radio emitting electrons (Fig. 2.3). Indeed the diffusion time necessary for the electrons to cover such distances is much larger than their radiative life-time; quantitatively, radio emission at ~ 1 GHz is typically due to electrons of $\approx 10 B_{\mu G}^{-1/2}$ GeV, which have a radiative life-time of $\sim 10^8$ yrs (Sec. 2.3.2). We can calculate that, during this time, these electrons can reach at most a diffusion distance of few tens of kpc (Blasi 2001; Brunetti 2003), which is several orders of magnitude smaller than the typical size of RHs. This argument, known as the *diffusion problem*, leads to the requirement that the emitting particles in halos are continuously accelerated or generated *in situ* in the emitting regions (Jaffe 1977).

In this section we will briefly describe the theoretical scenarios advocated to explain the observed non-thermal radio emission in galaxy clusters in form of RH. Two principal mechanisms are presently proposed to explain the origin of CRe emitting in RHs:

- Secondary models, in which secondary electron-positron pairs are continuously produced by inelastic hadronic collisions between accumulated CRp and thermal protons in the ICM (Blasi & Colafrancesco 1999; Miniati et al. 2001; Keshet & Loeb 2010; Ensslin et al. 2011) ;
- Re-acceleration models, in which relativistic particles are continuously re-accelerated by Magneto-Hydro dynamic (MHD) turbulence in the ICM (Petrosian 2001; Fujita et al. 2003; Cassano & Brunetti 2005; Brunetti et al. 2008; Beresnyak et al. 2013, Donnert et al. 2013).

More recently, *Hybrid Models* have been developed (Brunetti & Blasi 2005; Brunetti & Lazarian 2011), they include in a self-consistent way, secondary electrons and MHD waves.

2.4.1 Secondary Models

Secondary electron models were first suggested by Dennison (1980) and then considered in detail by Blasi & Colafrancesco (1999); more recently these models have been revisited by many authors in the framework of numerical simulations (e.g. Pfrommer et al. 2008; Donnert et al. 2010) where they can be easily implemented. There is growing consensus on the fact that, although the general feature of the observed RHs could be reproduced by secondary models, some of the spectral, morphological and statistical properties of RHs are hard to be explained by these models.

The maximum energies of the accelerated protons are expected to be >1 Tev and thus the relativistic electrons spectrum is expected to have maximum energies ≥ 100 Gev. Consequently the emission spectrum of a halo in the radio band should be a power law spectrum. For this reason the discovery of a synchrotron break in the integrated spectrum of a few RHs (e.g. Schlickeiser et al. 1987; Thierbach et al. 2003; Giacintucci et al. 2005) represents a challenge for secondary models, as well as the evidence of spatial steepening and/or patchiness which come from maps of synchrotron spectral index of a few RHs (Giovannini et al. 1993; Feretti et al. 2004; Orrù et al. 2007).

In some cases RHs have broad synchrotron profiles, flatter than the X emission of the cluster (Govoni et al. 2001) and this is again challenging for secondary models. Indeed, in order to reconcile such profiles with theoretical models, the magnetic field intensity should be almost constant on scales comparable to the cluster size (Brunetti et al. 2003,2004; Marchegiani et al. 2007), which contrasts with the amplification scenario described in Sec. 2.3.1.

Finally, present radio data allow to conclude that the typical life-time of RHs should be of the order of 1 Gyr (Hwang 2004; Brunetti et al. 2009), in contrast with a secondary origin of electrons which would produce very long living RHs, being the protons life-times (electrons sources) very long.

An unavoidable consequence of this scenario is the emission of γ -rays due to the decay of π^0 that are produced by the same decay chain that is responsible for the injection of secondary CRe (Sec. 2.3.2). γ -ray upper limits from EGRET observations provide limits $E_{CR}/E_{ICM} < 0.3$ in several nearby galaxy clusters (Reimer et al. 2004). The recent advent of the orbiting FERMI-LAT observatory has greatly improved the detection prospects thanks to its unprecedented sensitivity at Mev/GeV energies. However, after almost 5 years of operations, no galaxy cluster has been detected. Only upper limits to the γ -ray emission from cluster of galaxies have been obtained, constraining $E_{CR}/E_{ICM} < \text{about } 1\%$ (The Fermi-LAT Collabora-

tion: Ackerman et al. 2013).

Radio observations of galaxy clusters also provide limits on E_{CR}/E_{ICM} (Reimer 2004, Brown 2011), indeed only a fraction of clusters host diffuse, Mpc scale synchrotron emission. Radio upper limits constrain the combination of the energy densities of the magnetic field and secondary CRe, and consequently the energy budget in form of primary CRp as a function of the magnetic field. Faraday RM indicate that galaxy cluster are magnetised at $\approx \mu\text{G}$ level (Sec. 2.3.1) and this information allows one to break degeneracy between CRp and magnetic field energy densities. As a result one can constrain $E_{CR}/E_{ICM} \leq \text{few} \times 0.01$ (Brunetti et al. 2007).

Present FERMI plus radio upper limits significantly constrain the role of secondary electrons, challenging an hadronic origin of RHs. However, as we outlined in Sec. 2.2, γ -ray emission from galaxy clusters is a natural expectation of theoretical models due to the confinement of CRp in the ICM. Contrary to the transient nature of RHs and Hard X-ray emission, the γ -ray emission is expected to be common at a moderate level in all clusters, independently on their dynamical status and not directly correlated with the presence of RHs. The level of this emission is still unclear, since the CRp population of a cluster reflects its integrated history there should be a moderate range in γ -ray luminosities (Miniati et al. 2001). In this respect, future observations with Fermi-LAT and with the Cerenkov Telescope Array (CTA) are extremely important as they will definitely clarify the role of CRp and their secondaries for the origin of non-thermal emission in galaxy clusters.

2.4.2 The re-acceleration scenario

Turbulence can be generated during cluster mergers on large scales, $L_0 \sim 100 - 400$ kpc and might have typical turbulent velocities around $V_0 \sim 300 - 700$ km/s (e.g. Subramanian et al. 2006). Numerical simulations suggest that turbulence may store an appreciable fraction (5-30%) of the thermal energy of the ICM (e.g. Dolag et al. 2005, Vazza et al. 2006).

Theoretically, a fluid becomes turbulent when the rate of viscous dissipation at the injection scale, L_0 , is much smaller than the energy transfer rate, i.e. when the Reynolds number is $R_e = \frac{V_L L_0}{\nu_K} \gg 1$, where V_L is the injection velocity and ν_K is the kinetic fluid viscosity. Without considering the effect of magnetic field, the Reynolds number is formally just sufficient for initiating the developing of turbulence; however the ICM is magnetised and it has been demonstrated (e.g. Brunetti & Lazarian 2007) that the effective Reynolds number in presence of magnetic field is much larger than that estimated in the unmagnetised case. These considerations allow to conclude that the effective Reynolds number in the inner ICM is $R_e \gg 10^3$, suggesting that a cascade of turbulence could be established from large to smaller scales without being significantly dissipated by viscosity. When the frequency of the turbulent modes is larger than the ion-ion collision frequency, the collisionless

regime starts and the main source of turbulent dissipation is collisionless damping with particles in the ICM, i.e. particle acceleration.

Turbulence in the ICM can potentially trigger several mechanisms of particle acceleration. Actually, acceleration of CRs directly from the thermal pool to relativistic energies by MHD turbulence in the ICM is very inefficient and faces serious problems associated to energy arguments (Petrosian & East 2008; Chernyoshev et al. 2012); consequently turbulent acceleration in the ICM is rather a matter of re-acceleration of pre-existing CRs rather than *ab initio* acceleration of CR (Brunetti et al. 2001; Petrosian 2001). The non-linear interplay between particles and turbulent modes is a stochastic process that drains energy from plasma turbulence into particles (Melrose 1980; Schlickeiser 2002). Re-acceleration models are basically second order Fermi acceleration, in which charged particles are stochastically accelerated due to random interaction with the perturbations (waves) in the structure of the magnetic field. According to this scenario, particles could interact with either large scale compressible (magnetosonic) modes or small scale Alfvén modes.

Alfvén waves are transversal, incompressible waves, circularly polarised propagating along, or at some angle, to the magnetic field lines. They efficiently accelerate relativistic particles through resonant interactions. The condition for resonance between a wave of frequency ω and wavenumber projected along the magnetic field k_{\parallel} , and a particle of type α with energy E_{α} and projected velocity $v_{\parallel} = v\mu$ is (Melrose 1968; Eilek 1979):

$$\omega - n \frac{\Omega_{\alpha}}{\gamma} - k_{\parallel} v_{\parallel} = 0 \quad (2.5)$$

where Ω_{α}/γ is the relativistic gyrofrequency. The most important resonance for electron interaction with Alfvén waves is the $n = -1$ resonance, while for protons is $n = +1$ (Melrose 1968).

Magneto-sonic waves, instead are compressible waves propagating across, or at an angle, to the magnetic field. Large scale magneto-sonic waves can interact with particles through the $n = 0$ resonance (Melrose 1968; Eilek 1979):

$$\omega - k_{\parallel} v_{\parallel} = 0 \quad (2.6)$$

which is called *Transit Time Damping* (TTD, Eilek 1979; Schlickeiser & Miller 1998).

Even though the physics of particles acceleration is very complex and it is not completely understood yet, it is worth stressing that re-acceleration models clearly predict simple properties of RHs which are almost independent of the detail of the adopted physics:

- The predicted maximum Lorentz factor of the re-accelerated electrons is $\gamma \leq \text{few} \times 10^4$ producing a high frequencies cut-off in the spectral distribution (e.g. Petrosian 2001), which provides a unique possibility to explain the steepening

of the integrated synchrotron spectrum observed in several RHs (Feretti 2005; Dallacasa et al. 2009) and the complex behaviour revealed on the spectral index maps of RHs (Feretti et al. 2004, Orrù et al. 2007).

- The possibility to detect a RH depends on the observational frequency, which must be lower than the cut-off frequency. The cut-off frequency is determined by the maximum energy ($\propto \gamma_{max}^2$) of the radiating electrons defined by the balance between the energy gains (acceleration processes) and synchrotron and IC losses. As a consequence, there is a threshold in the efficiency, which has to be overcome by the re-acceleration processes, in order to accelerate electrons up to energies necessary to produce radio emission at the observed frequency in the cluster magnetic fields.
- Since turbulence is believed to be injected in the ICM during merger events, a natural expectation of the turbulent re-acceleration scenario is a connection between the presence of RHs and clusters mergers. We will deal with this argument in detail, but it is worth mentioning that nowadays it is clear that RHs are statistically more probable to be found in merging systems than in relaxed ones (Cassano et al. 2010; 2013).
- Most importantly, RHs should be transient phenomena in dynamically disturbed clusters. The time-scale of the RH phenomenon comes from the combination of the time necessary for the cascading of the turbulence from large to small scales (relevant for particle acceleration), of the time-scale for dissipation of the turbulence and of the cluster-cluster crossing time. Recent calculations, based on the observed clusters bimodality on the $P_{1.4} - L_X$ diagram show that RHs are short living, with $\tau_{RH} \leq 1$ Gyr (Brunetti et al. 2009).

Current X-ray observations don't allow to derive stringent constraints on the turbulent motions in dynamically disturbed clusters, this will hopefully change with the advent of the ASTRO-H satellite that will be able to measure the ICM turbulence through the Doppler broadening and shifting of metal lines induced by turbulence.

2.4.3 Mini-halos and Relics

RHs are the main topic of this Thesis work and they are extensively illustrated throughout all Chapters. RHs, however are not the unique radio diffuse emission from galaxy clusters. Here we provide a brief description of the main properties of mini-halos and relics and of the theoretical models suggested to explain their origin.

Mini-Halos

A number of relaxed, cool-core clusters host faint, diffuse radio emission with steep spectrum and a size comparable to that of the cool-core region (of the order of few 100 kpc)(Feretti et al. 2012). In contrast to RHs, Mini Halos (MH) are always found in relaxed systems, suggesting that the cluster mergers don't play a major role for their formation. Moreover, the synchrotron volume emissivity of MHs is typically larger than that of RHs (Cassano et al. 2008; Murgia et al. 2009). Physical mechanism that accelerate CRe in MHs are still poorly understood and whether they differ substantially from those acting in RHs is still unclear.

Clusters hosting MHs have always central AGNs whose outflows, in form of relativist electrons, could represent the primary source of CRs in MHs, however they are insufficient by themselves to explain the diffuse radio emission. As in the case of RHs, the energy loss time-scale of the emitting electrons is still much shorter than the time needed by these particles to diffuse across the emitting volume of the MH. Similarly to RHs, two principal models have been suggested to explain the origin of MHs: (i) re-acceleration of CRe (leptonic models or re-acceleration models) and (ii) generation of secondary CRe (hadronic or secondary models).

According to leptonic models, MHs originate due to the re-acceleration of pre-existing relativistic electrons in the ICM by turbulence in the core region (Gitti et al. 2002). The key question of this model is the origin of the turbulence in the cluster central region. Recent observations suggest that even relatively relaxed clusters have large-scale gas motions in their cores. The cold gas of the core sloshing in the cluster deep potential well can produce turbulence there (Ascasibar & Markevitch 2006; ZuHone et al. 2010,2011). In support for this scenario, a correlation between cold fronts in cluster cores and MHs has been discovered for a few clusters (Mazzotta & Giacintucci, 2008) and simulations have shown that turbulence generated by core sloshing in galaxy clusters cores can re-accelerate CRe (ZuHone et al 2013).

Future observations with ASTRO-H will provide much better constraints as they will be able to reveal the presence of small-scale turbulence from the study of X-ray lines (Takahashi et al. 2010; Zhuravleva et al. 2012).

The second mechanism proposed for the origin of MHs is based on the generation of secondary particles via inelastic collisions between CRp and thermal protons (Pfrommer & Enßlin 2004; Keshet & Loeb 010; Zandanel et al. 2013).

Discrimination between hadronic and leptonic models is very challenging because of the lack of observational constraints. Better spectral constraints might come from future observations at low (LOFAR) and high (JVLA) radio frequencies.

Relics

Some merging clusters host peripheral, giant radio relics, which are believed to trace shocks outside clusters cores (e.g. Brügggen et al. 2012; Kang et al. 2011,2012; Hoeft et al. 2008; van Weeren et al. 2010).

The association between relics and shocks is due to their elongated shape, additionally in some cases relics occurs in pairs on opposite sides of the cluster and an emerging merger shock is expected to form in such pairs. Relics are strongly polarised with an orientation that implies the magnetic field is aligned with the relic long axis, suggesting that they originate in regions where the magnetic field is compressed in the shock plane. Most important, in a few cases, merger shocks have been revealed by X-ray observations and they coincide with radio relics.

Presumably the observed CRe are accelerated at these shocks and can travel a maximum distance from the shock $= V_d \tau$, where V_d is the velocity of the downstream flow and τ is the radiative life-time of the emitting electrons at the observed frequency: $\tau \propto \nu_0^{-1/2}$. Without considering the detailed physical mechanism on which models of shock acceleration are based, we note that a spectral steepening with distance from the shock front is expected in relics as a consequence of the fact that the oldest population of CRe is also the most distant from the shock. This expectation is in agreement with several observations that provide evidence of steepening in radio relics along their transverse direction, from their front to the back (e.g Clake & Enßlin 2006; Giacintucci et al. 2008).

Radio relics are also important probes of the magnetic field properties in the ICM periphery, since they are found at distances up to a large fraction of the cluster virial radius and the CRe life-time depends also on the magnetic field.

Chapter 3

A statistical model for the formation of Radio Halos

In this chapter we attempt to summarize the statistical model proposed by Cassano & Brunetti (2005) and Cassano, Brunetti & Setti (2006) (CB05, CBS06 hereafter) to describe the evolution of the non-thermal emission from galaxy clusters in the framework of the turbulent re-acceleration scenario.

Statistical models have a fundamental role in our understanding of the physical processes involved in the formation and evolution of RHs, since they provide unique and unavoidable expectations that can be compared with statistical observational studies. This comparison provides stringent constraints on the physical parameters of these models and allows to explore the details of the complex physics involved in the ICM, that is still poorly understood.

CB05 and CBS06 modelled the statistical properties of RHs in a self consistent approach, i.e, an approach which should describe, at the same time, the evolution of the thermal properties of the ICM of the hosting galaxy clusters and the generation and evolution of the non-thermal phenomena.

The main ingredients of this model can be summarized as follows:

- (i) *Cluster formation.* The evolution and formation of galaxy clusters is computed following the extended Press-Schechter (1974) theory of structure formation developed by Lacey & Cole (1993). Given the present-day mass and temperature of clusters, the cosmological evolution of the clusters properties are obtained with Monte Carlo simulations. The large number of merger trees built up with this procedure, allows to describe the statistical cosmological evolution of galaxy clusters (Sec. 3.1).
- (ii) *Turbulence in galaxy clusters.* The turbulence in galaxy clusters is supposed to be injected during merger events and then dissipated on time-scales of the order of the cluster crossing time. The energetics of the turbulence injected in the ICM is estimated from the PdV work done by the infalling subcluster in passing through the volume of the most massive one.

- (iii) *Particle acceleration.* It is assumed that AGNs and/or galactic winds continuously inject relativistic electrons into the ICM, these electrons constitute the population of supra-thermal particles to be re-accelerated. At each time-step, the time evolution of relativistic electrons is computed by solving the Fokker-Planck equation, including the effect of electron acceleration and the energy losses (Sec. 3.3).

Given a population of galaxy clusters, by combining the three steps above, it is possible to follow statistically the cosmological evolution of the spectrum of the relativistic electrons in the volume of these clusters, the properties of the thermal ICM and the properties of the non-thermal emission.

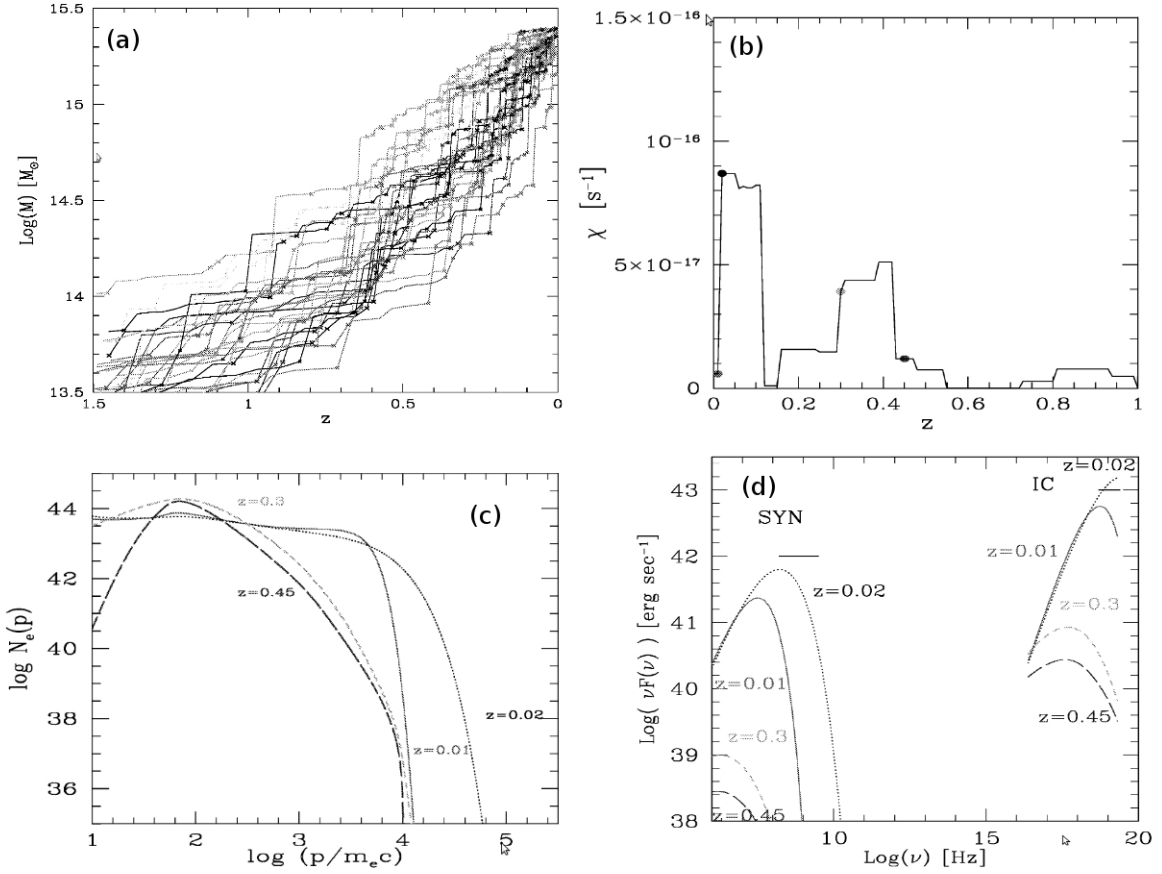


Figure 3.1: (a) Merger trees obtained from Monte Carlo simulations in an EdS Universe for clusters with present-day mass $M_0 = 2.5 \times 10^{15} M_\odot$. (b) Evolution with redshift of the electron-acceleration coefficient due to MS waves. (c) Electrons spectra calculated at different redshift for the same cluster. (d) Synchrotron and IC corresponding spectra. Calculation are performed assuming $\eta_e = 0.003$, $\eta_t = 0.26$, $R_H = 500$ kpc and $B = 0.5 \mu\text{G}$ (CB05).

3.1 Cluster formation

In the extended PS formalism (Lacey & Cole 1993) the probability that a “parent” cluster of mass M_1 at a time t_1 had a progenitor of mass in the range $M_2 \rightarrow M_2 + dM_2$ at some earlier time t_2 , with $M_1 > M_2$ and $t_1 > t_2$ is given by:

$$P(M_2, t_2 | M_1, t_1) = \frac{1}{\sqrt{2\pi}} \frac{M_1}{M_2} \frac{\delta_{c2} - \delta_{c1}}{(\sigma_2^2 - \sigma_1^2)^{3/2}} \left| \frac{d\sigma_2^2}{dM_2} \right| \exp \left[-\frac{(\delta_{c2} - \delta_{c1})^2}{2(\sigma_2^2 - \sigma_1^2)} \right] dM_2 \quad (3.1)$$

where $\delta_c(z)$ is the critical linear overdensity for a region to collapse at that redshift (Eq. 1.21, for EdS model) and $\sigma(M)$ is the standard deviation of matter density fluctuations. Considering a power-law spectrum of the perturbations, $\sigma(M)$ is given by (Randall, Sarazin & Ricker 2002):

$$\sigma(M) = \sigma_8 \left(\frac{M}{M_8} \right)^{-\alpha} \quad (3.2)$$

where σ_8 is the present epoch rms density fluctuation on a scale of $8h^{-1}$ Mpc and $M_8 = \frac{4\pi}{3}(8h^{-1} \text{Mpc})^3 \bar{\rho}$; $\bar{\rho}$ is the present epoch mean density of the Universe, i.e. the mass contained in a sphere of radius $8h^{-1}$ Mpc.

It is convenient to replace the mass M and time t with variables $S \equiv \sigma^2(M)$ and $x \equiv \delta_c(t)$; with these definitions, S decreases as the mass increases and x decreases with increasing the cosmic time. Eq. 3.1 can be written as:

$$K(\Delta S, \Delta x) d\Delta S = \frac{1}{\sqrt{2\pi}} \frac{\Delta x}{(\Delta S)^{3/2}} \exp \left(-\frac{(\Delta x)^2}{2\Delta S} \right) d\Delta S \quad (3.3)$$

with $\Delta S = \sigma_2^2 - \sigma_1^2$ and $\Delta x = \delta_{c2} - \delta_{c1}$.

Following a relatively standard procedure (Randall et al. 2002; Gabici & Blasi 2003) CB05 employ Monte Carlo techniques to construct merger trees. The Monte Carlo procedure selects a uniformly distributed random number, $0 < r < 1$, then, solving numerically the equation $P(< \Delta S, \Delta x) = r$, one determines the corresponding value of ΔS . $P(< \Delta S, \Delta x)$ is the cumulative probability distribution of subcluster masses, which represents the probability that a merger with a given ΔS occurs at a given time, it is given by:

$$P(< \Delta S, \Delta x) = \int_0^{\Delta S} K(\Delta S', \Delta x) dS' \quad (3.4)$$

The value of S_2 of the progenitor will be $S_2 = S_1 + \Delta S$. The mass of one of the subclusters is given by $\sigma^2(M_2) = S_2$, while the mass of the other subcluster is $\Delta M = M_1 - M_2$.

This procedure is thus iterated until either the mass of the larger cluster drops below the mass of the smallest subcluster that can be resolved individually in the tree (ΔM_c) or a maximum redshift is reached. An example of merger tree produced performing this procedure is shown in Fig. 3.1 (a).

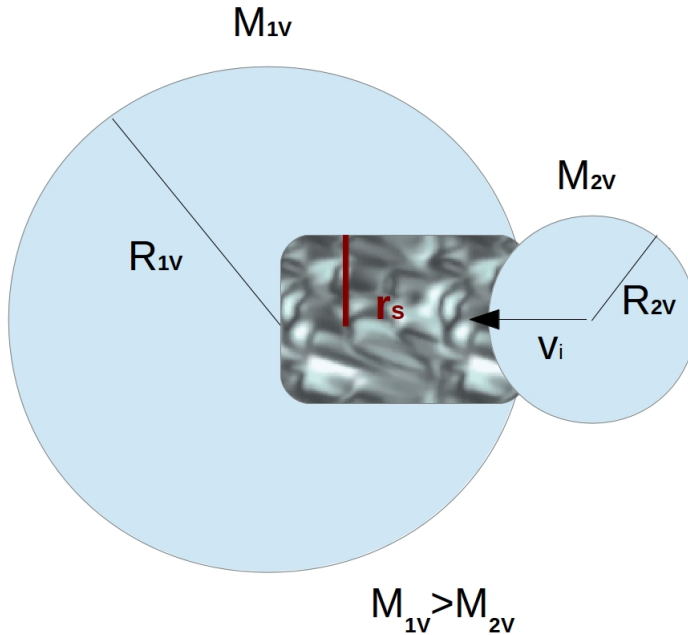


Figure 3.2: Cartoon of the geometry assumed for the binary clusters mergers: turbulence is injected in the ICM driven by the PdV work done by the infalling subcluster (M_2) passing through the volume of the most massive one (M_1).

3.2 Generation of turbulence during mergers

Numerical simulations found that mergers of subclusters with a main cluster generates large-scale bulk flows with velocities of the order of ~ 1000 km/s (e.g. Ricker & Sarazin 2001; Tormen, Moscardini & Yoshida 2004). Kelvin-Helmholtz instabilities can be generated at the interface of the bulk flows and the primary cluster gas (see Fig. 3.2 for a schematic picture of the merger geometry). These instabilities redistribute the energy of the mergers through the cluster volume in a few Gyr by injecting random and turbulent velocity fields.

The physics involved in these events is very complicated, nevertheless turbulence should be basically driven by the PdV work done by the infalling subcluster through the volume of the primary one and turbulent motions should be initially injected into the volume swept by the passage of the subhaloes (e.g. Fujita et al. 2003). Following this streamlined process one can estimate the rate of turbulence injected during a merger event.

If two subclusters with mass M_{max} and M_{min} collide at a distance R_{max} between the centres, with R_{max} being the virial radius of the cluster of mass M_{max} , the relative impact velocity is given by (Sarazin 2002):

$$v_i \simeq \left[2G \frac{(M_{max} + M_{min})}{R_{max}} \left(1 - \frac{1}{\eta_v} \right) \right]^{1/2} \quad (3.5)$$

where

$$\eta_v \simeq 4 \left(\frac{M_{max} + M_{min}}{M_{max}} \right)^{1/3} \quad (3.6)$$

During merging events the infalling haloes may be stripped due to the effect of the ram pressure; the stripping is efficient outside a radius r_s (the so-called stripping radius) at which equipartition between static and ram pressure is established.

Assuming that turbulence is injected into the swept volume $V_t \sim \pi r_s^2 R_{max}$ with a maximum turbulence length-scale of $2r_s$, the total energy injected in turbulence during a merger event is $E_t \simeq \bar{\rho}_{max,s} v_i^2 V_t$. It is assumed that turbulence is injected for a time of the order of the crossing time, $\tau_{cross} \simeq \frac{R_{max}}{v_i}$, and then dissipated in relatively short time (\sim Gyr). Under these hypothesis, the injection rate per unit time of turbulence is given by:

$$\frac{E_t}{\tau_{cross} \times V_H} \simeq \frac{\bar{\rho}_{max,s}}{R_{max}} v_i^3 \left(\frac{V_t}{V_H} \right) \quad (3.7)$$

where $V_H = (4\pi R_H^3)/3$ and R_H are the volume and the radius of the radio halo, respectively. $\bar{\rho}_{max}$ is the density of the ICM averaged on the swept cylinder.

Fig. 3.3 (a) shows the cosmological evolution of the thermal energy of galaxy clusters with different masses (solid lines), together with the total energy injected in the form of turbulence in the ICM (dashed lines). As a self-consistency check, we note that the energy injected in turbulence is well below ($\sim 15\%$) the thermal energy budget. Moreover, the turbulent energy is found to roughly scale with the cluster thermal energy and this yield to a fundamental expectation, indeed given the relation between the thermal energy and the cluster mass ($M \propto T^{3/2}$), the turbulent energy is expected to scale with the cluster virial mass (with slope $\simeq 5/3$). Simulations (Vazza et al. 2006) confirm that the energy in form of turbulence scales with the thermal energy of clusters (Fig. 3.3 (c)).

The energy of turbulence in Fig. 3.3 (a) is calculated integrating the contributions of all the merger events that the cluster experiences during its life-time, Fig. 3.3 (b), instead shows the differential turbulent energy, i.e. the energy in turbulence present at a given z . A crucial expectation coming out from this diagram is that turbulence in galaxy clusters should be a transient phenomenon (with typical time-scales of the order of the cluster crossing time) associated with merging events.

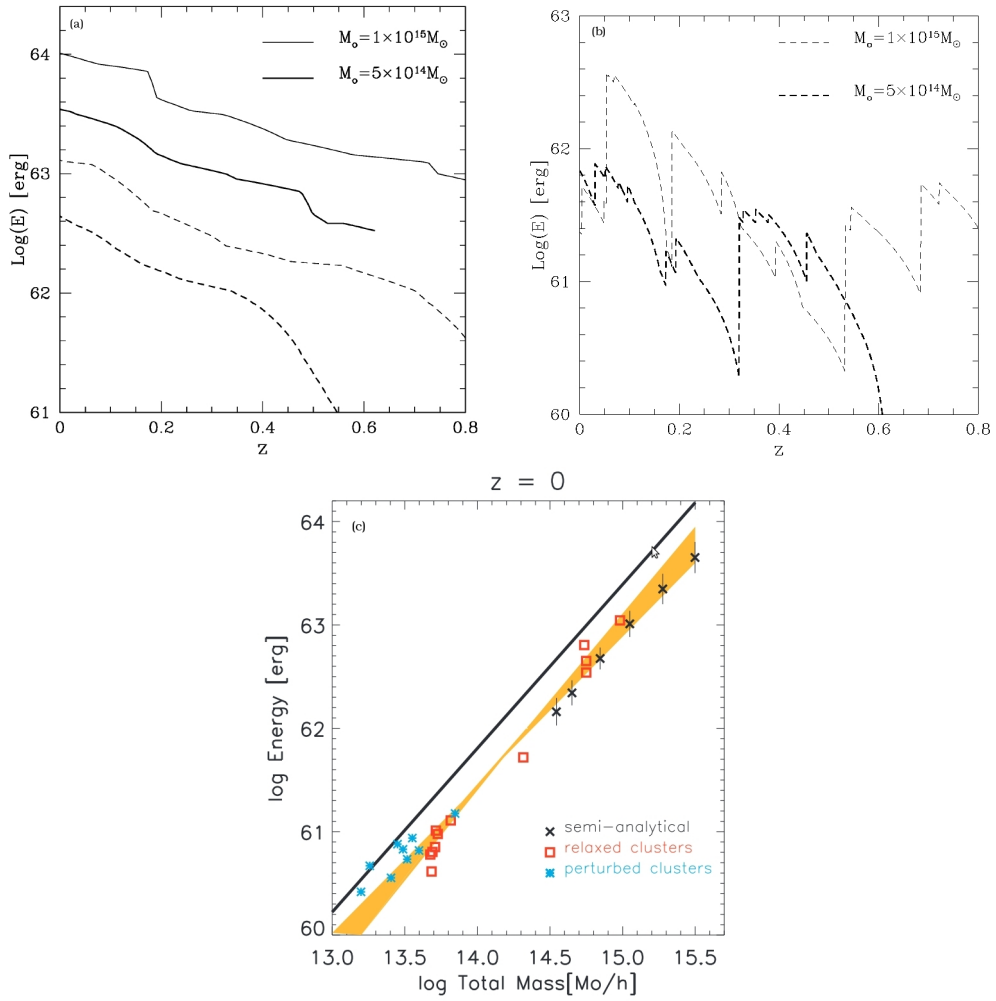


Figure 3.3: (a) Evolution of the thermal energy (solid lines) and of the energy injected in turbulence (dashed lines) integrated over the cluster life-time in typical Galaxy Clusters. (b) Evolution of the differential turbulent energy as a function of z (CB05). (c) Comparison between the turbulent energy injected in the ICM up to $z = 0$ and the cluster mass up to $z = 0$ (Vazza et al. 2006).

3.3 Particle acceleration by magneto-sonic waves

As discussed, cluster mergers are likely to generate turbulence in the ICM. CB05 assumed that a fraction η_t of this turbulence goes into magneto-sonic (MS) waves, with $\eta_t < 1$ being a free parameter of this model.

In the case MS waves are driven by plasma instabilities generated by turbulence developed during cluster mergers, it can be assumed a power-law injection spectrum for these waves:

$$I(k) = I_0 k^{-\alpha} \quad (3.8)$$

with $k > k_{min} \sim \pi/r_s$.

It can be estimated that the decay time of this turbulence at the maximum injection scale is of the order of the crossing time (~ 1 Gyr) and this allows the turbulence to diffuse filling a volume of the order of that of RHs with a rather uniform intensity. The turbulent energy injected per unit time and volume in form of MS waves is estimated as

$$I(k) = \int_k I_0 k^{-\alpha} dk = \eta_t \frac{E_t}{\tau_{cross} \times V_H} \quad (3.9)$$

where the terms on the right hand side of Eq. 3.9 are given by Eq. 3.7.

In general, the spectrum W_k of the waves evolves due to wave-wave and wave-particle coupling damping processes. Under the physical condition typical of the ICM, the most important damping of the MS waves is that with the thermal electrons (Eilek 1979, CB05), that is a function of the ICM temperature, $\Gamma_{th,e} = f(T)k$. Since for each merger event we are interested in the evolution of the turbulence on time-scale ~ 1 Gyr, order of magnitude larger than the damping time-scale, the spectrum of the waves approaches a stationary solution ($\frac{\partial W_k}{\partial t} = 0$). This solution is given by (CB05):

$$W_k \simeq \frac{I(k)}{\Gamma_{th,e}(k)} = \frac{I(k)}{f(T)k} \quad (3.10)$$

Given the spectrum of MS waves and the physical conditions of the ICM and assuming that the ICM is continuously supplied with relativistic particles by AGNs, Galactic Winds and merger shocks, we can compute the time evolution of relativistic electrons at each time step by solving the Fokker-Planck equation:

$$\frac{\partial N(p, t)}{\partial t} = \frac{\partial}{\partial p} \left[N(p, t) \left(\left. \frac{dp}{dt} \right|_{rad} + \left. \frac{dp}{dt} \right|_c - \frac{2}{p} D_{pp} \right) \right] + \frac{\partial}{\partial p} \left[D_{pp} \frac{\partial N(p, t)}{\partial p} \right] + Q_e(p, t) \quad (3.11)$$

where D_{pp} is the electron diffusion coefficient in momentums space due to interaction with MS waves and $\left. \frac{dp}{dt} \right|_{rad}$ and $\left. \frac{dp}{dt} \right|_c$ are the ionization (Coulomb losses term due to

the interaction with thermal plasma) and radiative losses (due to synchrotron and IC scattering of the CMB photons) terms.

$Q_e(p)$ is the injection rate of relativistic electrons, that can be modelled with a power law spectrum:

$$Q_e(p, t) = K_e(t)p^{-s} \quad (3.12)$$

where $s = 2.5$ is assumed. Approximate forms for the spatial diffusion coefficient can be written in different circumstances; for example, considering that the acceleration occurs via Transit Time Damping (TTD, Sec. 2.4) interaction between particles and MS waves D_{pp} is given by:

$$D_{pp} = F \frac{c_s^2 p^2}{P} \int kW(k)dk \quad (3.13)$$

giving an acceleration time-scale

$$\tau_{acc}^{-1} = \chi \simeq 4 \frac{D_{pp}}{p^2} \quad (3.14)$$

where χ is the electron acceleration coefficient, [s^{-1}].

Thus the systematic energy gain of particles interacting with MS waves will be:

$$\left(\frac{dp}{dt} \right)_{acc}^{sys} = \chi p \quad (3.15)$$

Once large-scale turbulence is injected in the ICM, magneto-sonic modes takes a relatively long time (~ 1 Gyr) to cascade at collisionless scales. When turbulence reaches collisionless scales the acceleration process starts and particles take a time, of the order of the re-acceleration time, to be significantly boosted in energy. An example of the time evolution of the electron spectrum during the re-acceleration process is reported in Fig. 3.4: the seed electrons initially accumulated at $\gamma \sim 10^2 - 10^3$ are efficiently accelerated up to $\gamma \sim 10^4 - 10^5$. As time proceeds during the acceleration, CRe gain energy extracting an increasing energy budget from the turbulent cascade.

The electron-acceleration coefficient at redshift z can be obtained by combining all merger events that contribute to the injection of turbulence at that redshift:

$$\chi(z) \propto \frac{\eta_t}{R_H^3} \sum_j \left[\left(\frac{M_V + \Delta M}{R_V} \right)^{3/2} \frac{r_s^2}{\sqrt{k_b T}} \right]_j \times \begin{cases} 1 & \text{if } r_s \leq R_H \\ (R_H/r_s)^2 & \text{if } r_s \geq R_H \end{cases} \quad (3.16)$$

In Fig. 3.1 we report (b) an example of the redshift evolution of the electron acceleration coefficient and (c) the corresponding spectra of the electrons at different times which is computed by solving the Fokker-Plank equation (Eq. 3.11). The synchrotron and IC emission are then calculated assuming that a fraction of the

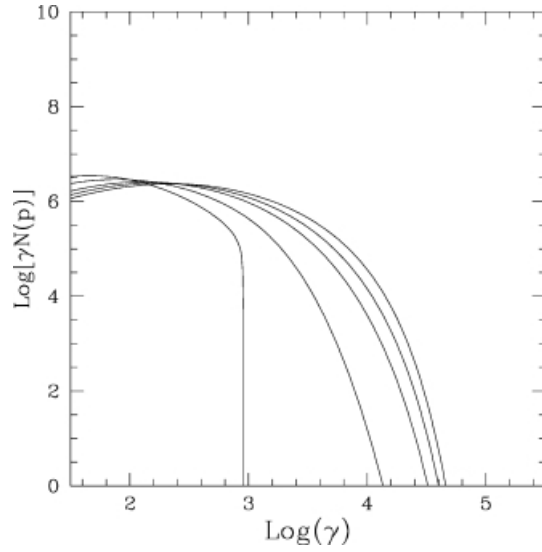


Figure 3.4: Example of the time evolution of the spectrum of relativistic electrons as a function of the Lorentz factor. Calculations are reported for : $t = 0.4 \times 10^{15}, 8 \times 10^{15}, 10^{16}, 1.2 \times 10^{16}$ s from the start of the re-acceleration phase (Brunetti & Lazarian 2007).

energy injected in relativistic electrons during the cluster life-time is a fraction η_e of the present-day thermal energy of the cluster (Fig. 3.1 (d)). η_e is a free parameter of the model, and its value can be constrained by requiring that the model reproduces the typical luminosities of RH in of galaxy clusters: $L_R = 10^{40} - 10^{41}$ erg s $^{-1}$. It has been found that $\eta_e = 10^{-4} - 10^{-3}$ is sufficient to match the observed luminosities.

3.4 Occurrence of Radio Halos in Galaxy Clusters

An important expectation of the turbulent re-acceleration scenario arises from the fact that particle acceleration by turbulence is a poorly efficient process. As a consequence, electrons can only be accelerated up to energies of $m_e c^2 \gamma_{max} \leq$ several GeV, causing a high frequencies cut-off in the synchrotron spectra of RHs. For this reason, the possibility to observe a RH in a cluster should be related to the frequency of observation, indeed the spectral steepening makes very challenging the detection of RHs at frequencies higher than the frequency ν_s at which the steepening becomes severe (Fig. 3.5). ν_s is expected to be \sim few times the break frequency, ν_b , which is defined as:

$$\nu_b \propto \langle B \rangle \gamma_b^2 \propto \frac{\langle B \rangle \chi^2}{(\langle B \rangle^2 + B_{CMB}^2)^2} \quad (3.17)$$

with γ_b being the maximum energy of the emitting electrons. ν_b is a function of the cluster magnetic field and depends on the electron acceleration coefficient, χ (Eq. 3.16) which in turn is related to the mass of the cluster and on the kind of merger (ΔM). Therefore higher values of the break frequency are expected in more massive clusters and in connection with major mergers. As a consequence, RHs with $\nu_s \geq$ GHz should be generated in the most massive clusters undergoing energetic merger events, that however are rare in the Universe. Less energetic mergers involving clusters of smaller mass are instead more common and are expected to generate RHs emitting at lower frequencies. Therefore a key expectation of this scenario is that the number of RHs should increase going from GHz to lower observational frequencies.

A unique expectation of this scenario is thus the existence of a complex population of RHs made by RHs with very different synchrotron spectra (Fig. 3.5). In particular, observing at frequency $\nu_o \approx$ GHz, one should expect to find also RHs with extremely steep spectra ($\alpha \simeq 1.9$), the so-called Ultra Steep Spectrum Radio Halos (USSRH).

3.4.1 Probability to form RHs as a function of clusters mass and redshift

In order to derive statistically the expected occurrence of RHs from this model one needs to fix the magnetic field in galaxy clusters. In this model the cosmological evolution of the magnetic field is accounted for by scaling the field with the cluster mass, as suggested by cosmological MHD simulations (e.g. Dolag et al. 2002):

$$B = B_{\langle M \rangle} \left(\frac{M}{\langle M \rangle} \right)^b \quad (3.18)$$

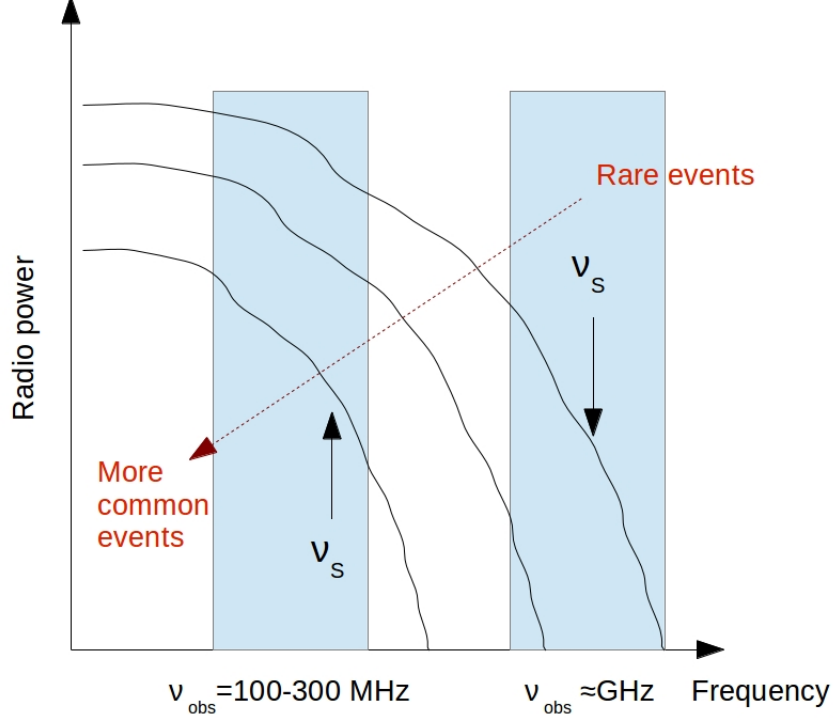


Figure 3.5: A schematic representation of the theoretical spectra of RHs with different values of ν_s (and consequently ν_b). Coloured regions indicate different frequency ranges of observation.

where $B_{\langle M \rangle}$ is the magnetic field of a cluster with mass $\langle M \rangle$. To constrain this scaling-law, CBS06 compare the expected scaling between the bolometric radio power, P_R and the virial cluster mass:

$$P_R \propto \frac{M_v^{2-\Gamma} B_{\langle M \rangle}^2}{(B_{\langle M \rangle}^2 + B_{CMB}^2)^2} \quad (3.19)$$

(with $T \propto M^\Gamma$, $\Gamma \approx 2/3$ in the virial scale) with the observed one: $P_R \propto M_V^{2.9 \pm 0.4}$. From this comparison they constrained the possible values that $B_{\langle M \rangle}$ and b can assume to match the observed slope of the $P_R - M_v$ correlation. In the allowed region of the $(B_{\langle M \rangle}, b)$ diagram (Fig. 3.6 shaded area) one can immediately identify two allowed regime:

- a *superlinear scaling* ($b > 1$) with relatively high values of B
- a *sublinear scaling* ($b > 1$) with lower values of B

A free parameter in the computation of the RH statistics is the parameter η_t (i.e. the fraction of turbulence injected in MS waves). To constrain the value of η_t , CBS06 derived the occurrence of RHs by assuming different values of $(B_{\langle M \rangle}, b)$ and

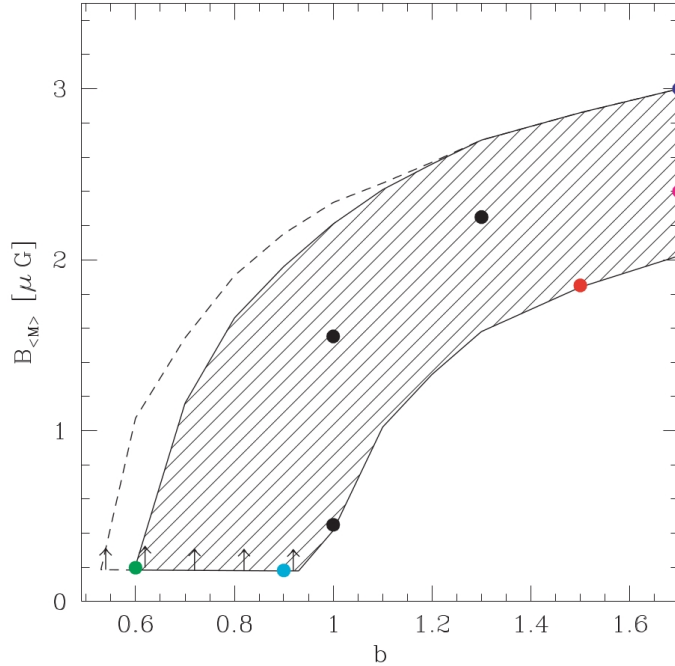


Figure 3.6: The shadowed area represents the region in the $(B_{\langle M \rangle}, b)$ plane allowed from the observed $P_{1.4} - M_v$ and the $P_{1.4} - T$ correlations. The dashed line indicates the upper bound of the allowed region obtained considering only the $P_{1.4} - M_v$ correlation. The vertical arrows indicate the IC limits on B (CBS06).

compared the expectations with the observed fraction of clusters with RH at $z < 0.2$ (Giovannini et al. 1999). They found that the requirement in terms of energy of MS waves increases with decreasing the magnetic field intensity: $\eta_t \sim 0.15 - 0.2$ for intermediate large values of B and up to $\eta_t \sim 0.5$ at the lower bound of the allowed B strengths.

The scaling of the magnetic field with the cluster mass is reflected in the dependence of the RH occurrence on the cluster mass and redshift. In particular, when the rms magnetic field strength in the emitting volume is smaller than the equivalent magnetic field strength of the CMB ($B < B_{CMB}$, IC dominance), electron energy losses are mainly due to the IC mechanism. In this case an increase of B does not significantly affect the electrons energy losses, it causes an increase of ν_b and thus an increase of the probability to form RHs (see Eq. 3.17). When B overcomes B_{CMB} , the synchrotron emission becomes the dominant process (synchrotron dominance). In this case an increase of the field implies a decrease of ν_b . The scaling $B \propto M^b$, adopted by CBS06, implies that the synchrotron dominance occurs first in more massive objects. Clusters of smaller mass have $B \ll B_{CMB}$ implying, from the combination of Eq. 3.17 and 3.16, that the probability to form RHs in these clusters increases with the cluster mass and decreases with redshift.

The case of more massive clusters may be more complicated, because for these

clusters there is a value of the mass, M_* , for which the cluster magnetic field equals B_{CMB} . For $M > M_*$ one finds that the probability to form RH would decrease with increasing the cluster mass.

Consequently, going from smaller to larger masses, we expect that the probability should reach a maximum value around M_* and then it should start to smoothly decrease. The value of this critical mass increases with z and depends on the scaling law between B and M :

$$M_*(z) \simeq \langle M \rangle \left[\frac{3.2(1+z)^2}{B_{\langle M \rangle}(\mu G)} \right]^{1/b} \quad (3.20)$$

To analyse this complex behaviour we can distinguish two cases:

- *superlinear regime* ($b > 1$): Fig 3.7 (a) shows that at lower redshift ($z \lesssim 0.1$) the probability to form RHs increases with the cluster mass up to $M_* \sim 2 \times 10^{15} M_\odot$, i.e. up to $B \sim B_{CMB}$, while for $M \gtrsim M_*$ synchrotron losses become dominant and cause the decrease of the probability. Since $M_* \propto (1+z)^{2/b}$, as the cluster mass increases the maximum probability is reached at higher redshift. In Fig. 3.7 (b) one can see the different behaviour of the probability as a function of z depending on the cluster mass. Clusters in the high mass bin have $B \gtrsim B_{CMB}$ at any redshift thus the behaviour of the probability with z is essentially driven by the fact that the bulk of turbulence in these massive clusters is injected preferentially between $z \sim 0.2$ and 0.5. In the lower mass bin instead, the occurrence of RHs decreases with z because clusters have always $B < B_{CMB}$.
- *sublinear regime* ($b < 1$): In this case, at any redshift, the probability to form RHs increases with the cluster mass (Fig 3.8). This is due to the fact that in these clusters $B \ll B_{CMB}$ for all redshift and masses and IC losses are always dominant. Furthermore, as expected, the probability decreases as a function of z , because of the increasing IC losses.

3.4.2 Occurrence of RHs at different frequencies

As qualitatively discussed at the beginning of this Section, an important expectation of this model is that the fraction of clusters hosting RHs should increase with decreasing the observing frequency. Results based on Monte Carlo simulations are presented in Fig. 3.9, here it is shown the fraction of clusters with RHs with $\nu_s \geq \nu_o$ (with ν_o being the observing frequency as a function of the cluster mass). In general, the probability to form RHs increases with increasing the cluster mass and, as expected, the occurrence of RHs increases at lower frequencies. Furthermore, this increase is greater for relatively low massive systems and at higher redshifts. This is due to the presence of a population of USSRH which are only visible at low radio

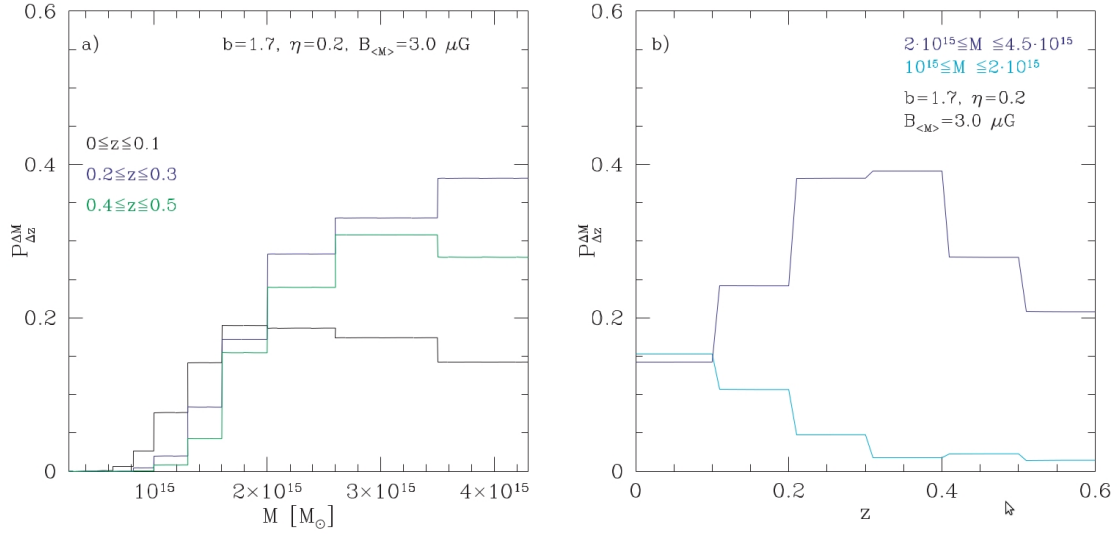


Figure 3.7: (a) Occurrence of RHs as a function of the cluster mass in three redshift bins: 0-0.1 (black line), 0.2-0.3 (blue line) and 0.4-0.5 (green line). (b) Occurrence of RHs as a function of redshift in two mass bins: $1 - 2 \times 10^{15} M_{\odot}$ (cyan line) and $2 - 4 \times 10^{15} M_{\odot}$ (blue line). Calculations have been performed assuming: $b = 1.7$, $B_{\langle M \rangle} = 3 \mu\text{G}$, $\langle M \rangle = 1.6 \times 10^{15} M_{\odot}$ and $\eta_t = 0.2$ in both panels (CBS06).

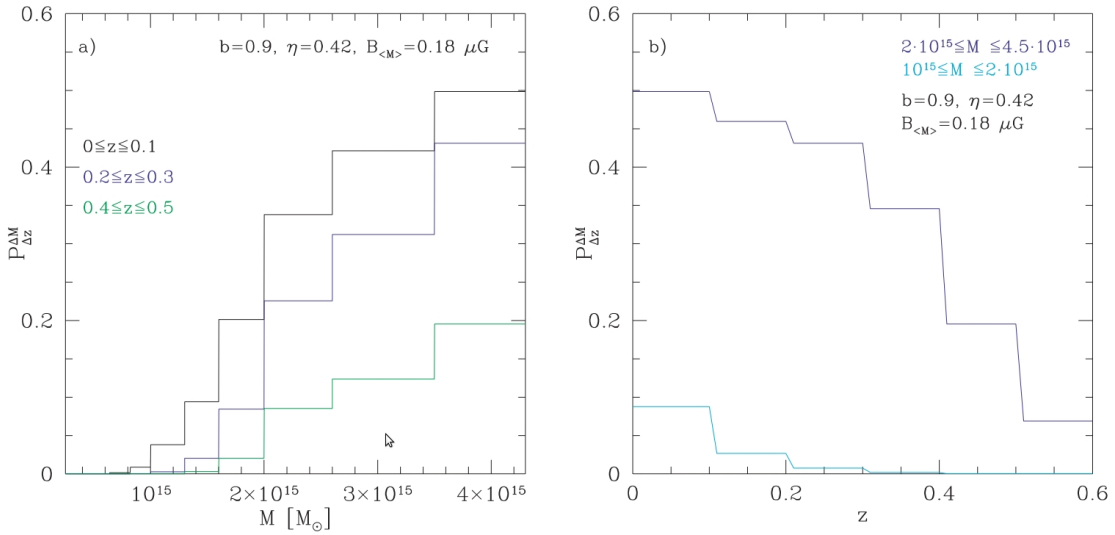


Figure 3.8: (a) Occurrence of RHs as a function of the cluster mass in three redshift bins: 0-0.1 (black line), 0.2-0.3 (blue line) and 0.4-0.5 (green line). (b) Occurrence of RHs as a function of redshift in two mass bins: $1 - 2 \times 10^{15} M_{\odot}$ (cyan line) and $2 - 4 \times 10^{15} M_{\odot}$ (blue line). Calculations have been performed assuming: $b = 0.9$, $B_{\langle M \rangle} = 0.2 \mu\text{G}$, $\langle M \rangle = 1.6 \times 10^{15} M_{\odot}$ and $\eta_t = 0.42$ in both panels (CBS06).

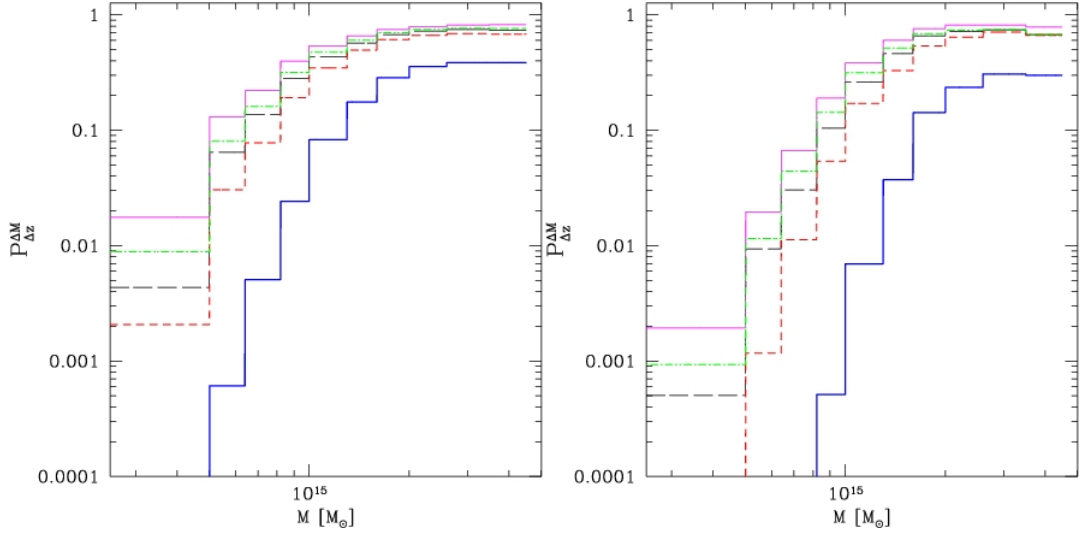


Figure 3.9: Fraction of clusters with RHs with $\nu_s \geq \nu_o$ as a function of the cluster mass in the redshift range 0-0.1 (left panel) and 0.4-0.5 (right panel). Calculations assume $\nu_o = 1.4$ GHz, 240 MHz, 150 MHz, 120 MHz, and 74 MHz (from bottom to top). $\langle B \rangle = 1.9 \mu\text{G}$, $b = 1.5$, $\langle M \rangle = 1.6 \times 10^{15} M_{\odot}$, $\eta_t = 0.2$ are assumed (Cassano et al. 2010).

frequency and that are potentially generated in smaller systems and at relatively higher z with respect to RHs emitting up to GHz frequencies. This is because turbulence generated in smaller systems ($M \lesssim 10^{15} M_{\odot}$) is not sufficient to boost particle acceleration up to the energy necessary to emit synchrotron radiation at GHz frequencies, and at high redshift IC losses get into play, limiting the maximum energy of the accelerated electrons and thus decreasing the break frequency.

In Fig. 3.10 we report the fraction of clusters with RHs with $\nu_s \geq 120$ MHz (black upper line) and the differential contribution to this fraction from RHs with ν_s in four frequency ranges (see caption for details). The great majority of clusters with mass $\gtrsim 10^{15} M_{\odot}$ are expected to host RHs with $\nu_s > 600$ MHz (magenta line), while few of them are expected to have $120 < \nu_s < 240$ MHz (black line). On the other hand in the low mass bin ($M \lesssim 10^{15} M_{\odot}$) RHs with $120 < \nu_s < 240$ MHz are largely dominant with respect to RHs with higher value of ν_s .

A similar situation is expected in the high redshift range (Fig. 3.10, right panel), where however high values of ν_s become rare due to IC losses. Higher value of the mass are required to have a sizeable fraction of clusters hosting RHs with $\nu_s > 600$ MHz.

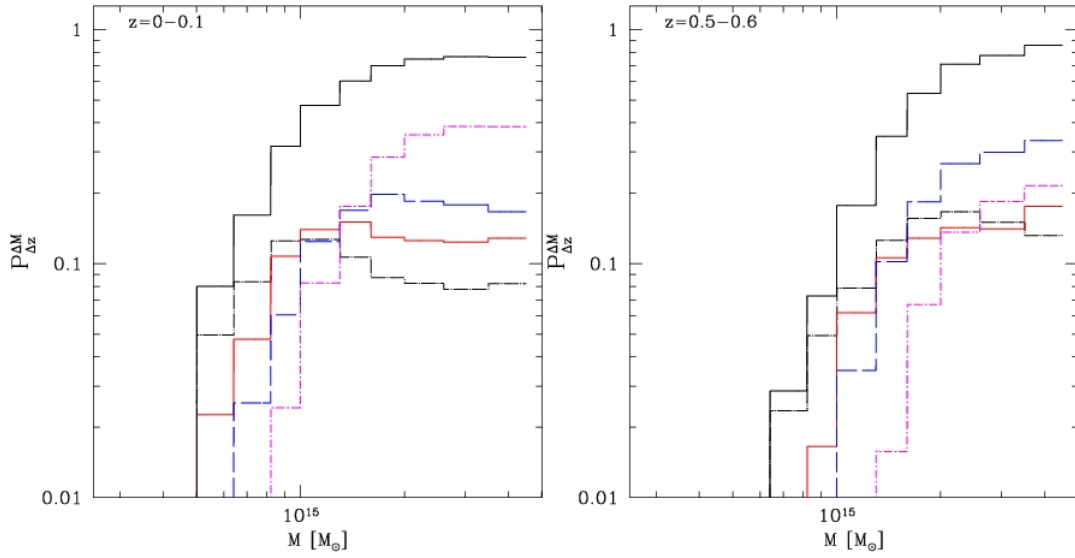


Figure 3.10: Fraction of clusters hosting RHs with $\nu_s \geq 120$ MHz (black, upper, solid lines) as a function of the cluster mass in the redshift range 0-0.1 (left panel) and 0.5-0.6 (right panel). The fractions of clusters with RHs ν_s in different frequency ranges are also shown: $\nu_s \geq 1400$ MHz, $600 < \nu_s < 1400$ MHz, $240 < \nu_s < 600$ MHz, and $120 < \nu_s < 240$ MHz (from top to bottom). $\langle B \rangle = 1.9 \mu G$, $b = 1.5$, $\langle M \rangle = 1.6 \times 10^{15} M_{\odot}$, $\eta_t = 0.2$ are assumed (Cassano et al. 2010).

Chapter 4

Statistical properties of Radio Halos

The knowledge of the statistical properties of RHs, namely their formation rate in the Universe and their link with clusters evolution (mass, dynamics, redshift) is fundamental to address their origin.

Pioneering studies using Arecibo, the NVSS and WENSS radio surveys to identify candidates RHs in clusters suggested that RHs are not ubiquitous in clusters of galaxies (Hanish 1982; Giovannini et al. 1999; Kempner & Sarazin 2001). Giovannini et al. (1999) derived the occurrence of RHs in the X-ray-brightest Abell-type clusters (XBACs) by inspection of the NRAO VLA Sky Survey (NVSS, Condon et al. 1998) at 1.4 GHz for cluster at $z < 0.2$. They found also that the occurrence of RHs increases with increasing the X-ray luminosity of the parent cluster. Yet it remains unclear the role of selection biases due to the brightness limit of the used radio surveys (Kempner & Sarazin 2001; Rudnick et al. 2005, 2006).

In this respect an important step has been achieved in the last few years, thanks to the GMRT Radio Halo Survey (GRHS, hereafter) (Venturi et al. 2007, 2008), a unique survey dedicated to the search of RHs at 610 MHz in X-ray selected clusters. These observations were designed to avoid problem in the detection of large-scale emission due to the missing of short baselines in the interferometric observations and to image, at the same time, both compact and extended sources in the selected clusters. In this Chapter we briefly describe the GRHS and its main results, that are considered observational milestones for the origin and evolution of RHs.

4.1 The GMRT Radio Halo Survey

Carried out with the Giant Metrewave Radio Telescope (GMRT, Pune, India) at 610 MHz, the GRHS was a necessary step to start a statistically solid investigation of the RH properties in the Universe. In this Section we briefly describe the survey and its major results.

4.1.1 The Sample

Venturi et al. (2007, 2008) (V07, V08, hereafter) selected a sample of galaxy clusters at $0.2 \leq z \leq 0.4$ from the combination of two X-ray subsamples: the ROSAT-ESO flux limited X-ray galaxy clusters catalogue (REFLEX, Böhringer et al. 2004) and the Extended ROSAT Brightest Cluster Sample catalogue (eBCS, Ebeling et al. 1998, 2000). The selection criteria are:

- L_X (0.1-2.4 keV) $\geq 5 \times 10^{44}$ erg/s
- $0.2 \leq z \leq 0.4$
- $-30^\circ < \delta < +2.5^\circ$ for the REFLEX sample and $-15^\circ < \delta < +60^\circ$ for the eBCS sample.

The limit in X-ray luminosity is aimed at selecting massive clusters, which are expected to host giant RHs (Cassano, Brunetti & Setti 2004; CB05). It corresponds to a lower limit in the virial mass of $M_v > 1.4 \times 10^{15} M_\odot$ if the $L_X - M_V$ derived in CBS06 is assumed, i.e.:

$$\log \left(\frac{L_X}{10^{44} h_{70}^{-1} \text{erg s}^{-1}} \right) = A_f + b_f \log \left(\frac{M_v}{3.16 \times 10^{14} h_{70}^{-1} M_\odot} \right) \quad (4.1)$$

where the best fitting values of the parameters are: $A_f = -0.229 \pm 0.051$ and $b_f = 1.47 \pm 0.08$ (CBS06). The value $\delta = 2.5^\circ$ is the REFLEX declination limit. The lower limit of $\delta = -30^\circ$ is chosen in order to ensure a good $u-v$ coverage with the GMRT. The choose of the declination range $-15^\circ < \delta < +60^\circ$ for the eBCS sample is imposed by the necessity to reach a compromise between the need to obtain a large sample and the observational effort to complete the requested radio information implied.

The full final sample includes 50 clusters, 27 from the REFLEX and 23 from the eBCS catalogue.

4.1.2 Detections and Upper Limits

The full resolution of the GMRT at 610 MHz is $\sim 5''$ and the largest nominal detectable structure is $17'$. This scale is much larger than the typical angular size of Mpc-scale RHs in the considered redshift bin, which is $\sim 3'$ at $z = 0.4$ and $\sim 5'$ at $z = 0.2$. This ensures the detection of the Mpc sized radio sources, which are the target of the GRHS.

Beyond the full resolution image, for each field, V07 and V08 produced also images with different resolution, tapering the $u-v$ data. A tapered image is essentially an image where the resolution has been decreased in order to increase the sensitivity to the diffuse emission. The rms noise (1σ level) is of the order of $50 - 80 \mu\text{Jy}/\text{beam}$

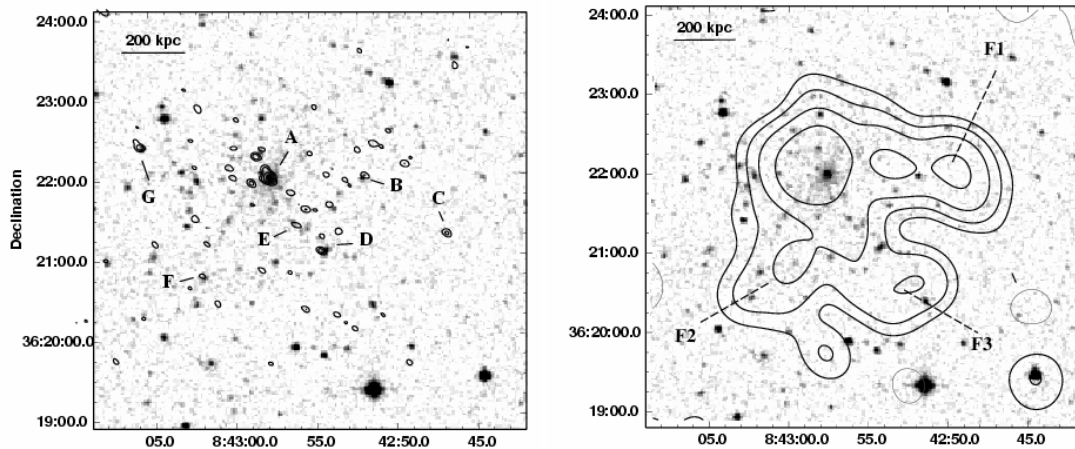


Figure 4.1: Left panel: 610 MHz GMRT radio contours of A697, overlaid on the DSS-2 optical image. The resolution of the image is $6'' \times 5''$, the contour levels are $\pm 0.075, 0.15, 0.3, 0.6, 1.2, 2.4, 4.8, 9.6 \text{ mJy b}^{-1}$. The rms level is $25 \mu\text{Jy b}^{-1}$. Right panel: Same portion of the radio sky with 610 MHz $40'' \times 35''$ image overlaid. The radio contours are $\pm 0.15, 0.3, 0.6, 1.2, 2.4, 4.8, 9.6 \text{ mJy b}^{-1}$. The rms level is $50 \mu\text{Jy b}^{-1}$ (V08).

both in the full resolution and tapered images. An example of the effect of tapering is shown in Fig. 4.1 for the RH cluster A697.

When the inspection of the cluster image and the measure of the flux density suggest the presence of some extended emission within a 1 Mpc region around the cluster centre, but this region contains individual sources, further data handling is necessary to blank the contribution of these sources. In these cases, in order to highlight the diffuse emission, V07 and V08 subtracted all the individual sources visible in the full resolution image from the $u-v$ data and then convolved the residuals with the HPBW. We report the case of RXCJ 2003.5-2323 for example (Fig. 4.2): the sources with a clear optical counterpart (B to H) were subtracted from the $u-v$ data when producing the image shown in the right panel.

Most of the clusters of the GRHS do not exhibit any hint of diffuse emission on the cluster scale, anyway if one manages to place firm upper limits on their radio power, they provide useful quantitative information. The procedure for placing upper limits on the flux density of extended emission was first used by V08: it consists of introducing a simulated (fake) RH of a given size and brightness in the $u-v$ data and then re-imaging the data. The fake RH of 1 Mpc diameter, which is the typical size of RHs, is modelled using optically thin concentric spheres to match the average profile of well studied RHs. The model is added to the $u-v$ data, then the new $u-v$ dataset is used to make images to be examined. Once the angular size of 1 Mpc diameter at the cluster redshift has been fixed¹ a series of images

¹The largest angular size (LAS) of the fake RHs range from $180''$ to $320''$, so as to cover the angular scale corresponding to a linear size of 1 Mpc in the redshift range 0.2-0.4.

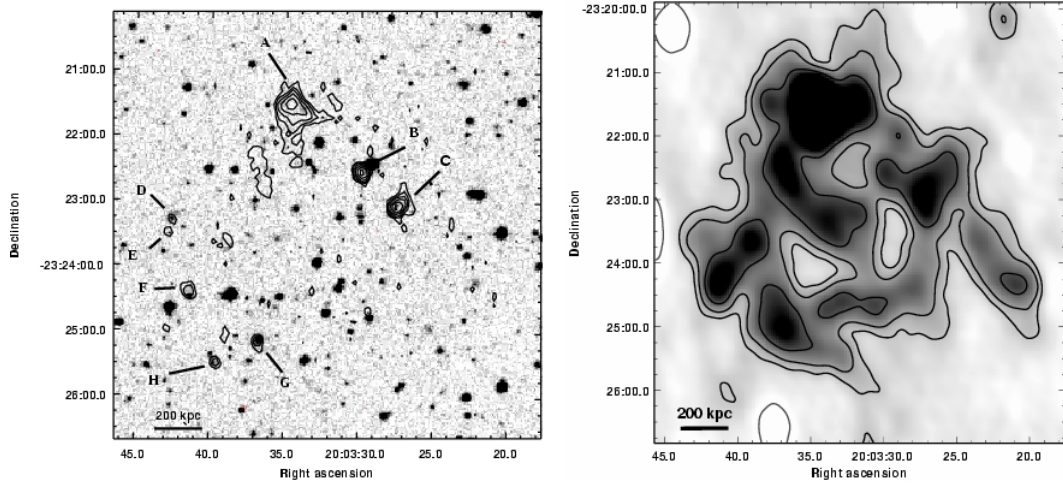


Figure 4.2: Left panel: full resolution GMRT 610 MHz contours of the central region of RXCJ 2003.5-2323, superposed to the POSS-2 optical image. The resolution of the radio image is $6.9'' \times 5.0''$, the 1σ level is $40 \mu\text{Jy b}^{-1}$. Contours are $0.12 \times (\pm 1, 2, 4, 8, \dots)$ mJy b^{-1} . Individual sources are labelled from A to H. Right panel: GMRT 610 MHz gray scale and radio contours of the RH in RXCJ 2003.5-2323 after subtraction of the individual sources (from B to H in the left panel). The HPWB is 32.0×23.0 . Contours are $0.3 \times (\pm 1, 2, 4, 8, \dots)$ mJy b^{-1} . The 1σ level in the image is $100 \mu\text{Jy b}^{-1}$ (V07).

are produced injecting total flux densities S_{inj} from 30 to 3 mJy (Fig. 4.3) until the diffuse emission results only in positive residuals which would lead to “suspect” emission. Therefore that value of S_{inj} is considered the upper limit to the RH flux density of that cluster where no evidence of central residual emission is found.

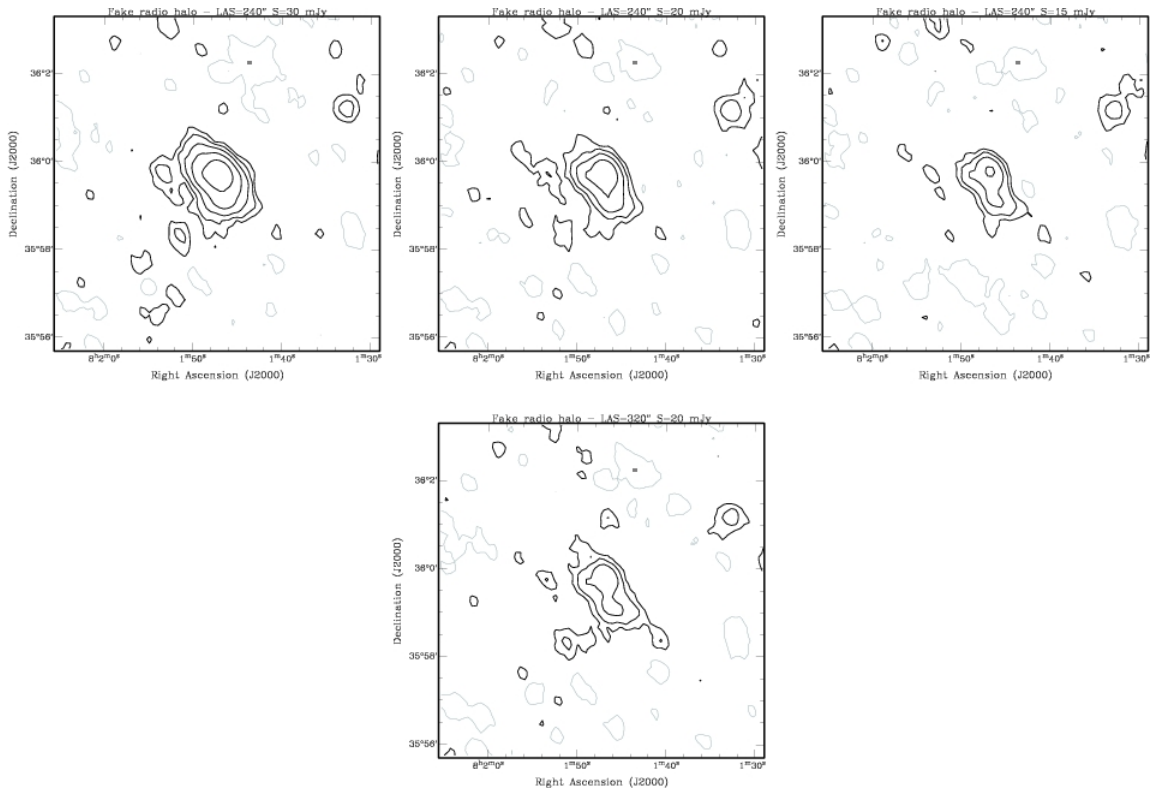


Figure 4.3: 610 MHz contours of fake RHs. Upper frame: Sequence with fixed $\text{LAS}=240''$ and decreasing S_{inj} (30, 20, 15 from left to right). Lower frame: An example with $S_{inj} = 20$ mJy and $\text{LAS}=320''$, to be compared to the central panel in the upper frame (V08).

4.2 Main Results

The GRHS led to the discovery of new RHS, mini-halos and relic/halo candidates. Most importantly, however, it allowed to achieve first statistical results and to test theoretical predictions derived from the turbulent acceleration model.

4.2.1 Ultra Steep Spectrum Radio Halos (USSRH)

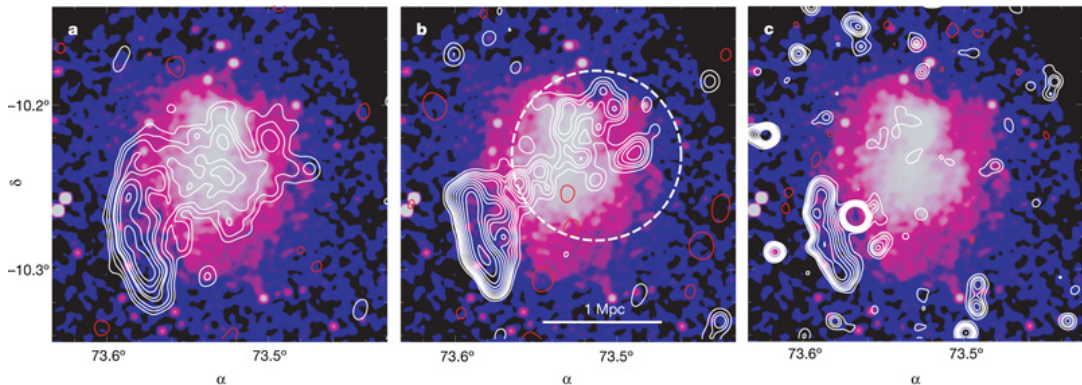


Figure 4.4: A521 low resolution radio contours overlaid to the Chandra X-ray image. (a) GMRT 240 MHz contours at a resolution of $35'' \times 35''$, $\text{rms}=220 \mu\text{Jy b}^{-1}$. (b) GMRT 610 MHz contours at a resolution of $35'' \times 35''$, $\text{rms}=58 \mu\text{Jy b}^{-1}$. (c) VLA 1.4 GHz contours at a resolution of $25'' \times 25''$, $\text{rms}=25 \mu\text{Jy b}^{-1}$. The RH can be seen as a patchy structure in the 610 MHz image (b), while it actually disappears in the 1.4 GHz image (c).

The analysis of the radio spectrum of RHs is important to investigate their origin. However, the spectral properties of RHs are hard to constrain, because of the observational difficulties in obtaining reliable measurements of RH flux densities spanning a large frequency range. During the last decade it has been found that the observed spectral index, α , of RHs spans a broad range of values: $\alpha \sim 1 - 2$, with $F(\nu) \propto \nu^{-\alpha}$ (Feretti et al. 2012; Venturi, 2011; Venturi et al. 2013). This implies that the synchrotron spectrum of RHs is not a universal power law and puts constraints on the mechanisms responsible for the origin of RHs. Particularly stringent constraints come from the discovery of RHs with extremely steep spectra ($\alpha \gtrsim 1.6$), the so-called Ultra Steep Spectrum Radio Halos (USSRH). The prototype of these sources is the USSRH in the galaxy cluster Abel 521 (Brunetti et al. 2008; Dallacasa et al. 2009), which is an X-ray luminous (8.2×10^{44} erg/s in the 0.1-2.4 keV band) cluster at $z = 0.25$ with ongoing multiple merging episodes (Arnaud et al. 2000; Ferrari et al. 2003). The discovery of a giant RH in this cluster has been achieved by means of deep GMRT observations at 240, 325 and 610 MHz (Brunetti et al. 2008). Fig. 4.4 clearly shows that at 1.4 GHz only the relic in A521 can be detected, while the RH becomes progressively more evident at lower frequencies (from the right panel to the left). These observations, plus deep VLA array D

observations at 1.4 GHz, allowed to reconstruct the spectrum of the RH (Fig. 4.5) and to measure the average value of the spectral index, $\alpha = 1.86 \pm 0.08$ (Dallacasa et al. 2009).

Another example of USSRH in the one found in A697 (Macario et al. 2010). In

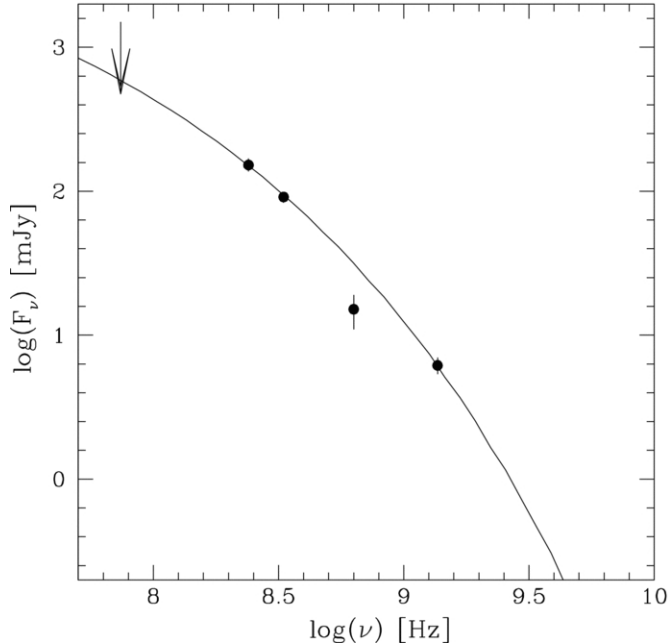


Figure 4.5: Synchrotron spectrum of the RH in A521. Measurement at 74, 240, 330, 610 MHz are taken from Brunetti et al. (2008), the flux density at 1.4 GHz is taken from Dallacasa et al. (2009). The line represents the re-acceleration model calculated following Brunetti & Lazarian (2007), assuming a central value for the magnetic field $B_0 = 3.5 \mu\text{G}$ and assuming that 18% of the thermal energy is in magneto-sonic waves.

addition, there are other cases of candidates USSRH (see Tab. 1 in Cassano et al. 2013).

Such extremely steep spectra (for comparison the typical slope of RHs are $\alpha \sim 1.2 - 1.3$, e.g. Feretti et al. 2004) and the downward spectral curvature imply a spectral cut-off frequency, which is a key feature of the turbulent acceleration in merging clusters (Schlickeiser et al. 1987; Brunetti et al. 2004). The turbulent re-acceleration scenario indeed predicts the existence of RHs with extremely steep spectra, when observed at GHz frequency, generated by less energetic merger events and/or in less massive clusters.

On the other hand, such steep spectra are not consistent with a secondary origin of the emitting electrons, that predict power-law spectra for RHs. Indeed, to explain for example the steep spectrum of the RH in A521 through synchrotron radiation from secondary electrons, the primary protons must have very steep spectral energy distribution ($N(p) \propto p^{-\delta}$, with $\delta \sim 4.2$, p is the particle momentum). In this case, the energy density of relativistic protons required to match the observed synchrotron

flux density is estimated to be $\sim 3 - 100$ times the energy density of the thermal plasma. Therefore the existence of USSRH can be used to rule out secondary electron models, because they would require an energy budget of CRs unacceptably large, even larger than the thermal energy budget of the cluster, which is clearly unphysical.

4.2.2 $P_{1.4} - L_X$ correlation & bimodality of galaxy clusters

The presence of a correlation between the radio power and the X-ray luminosity is well known (Liang et al. 2000; Esslin & Röttgering 2002). CBS06 also obtained the correlation between the X-ray luminosity in the 0.1-0.2 keV energy band and the radio power at 1.4 GHz for their sample of 17 RHs

Successively the existence of this correlation has been confirmed also for clusters belonging to the larger sample of the GRHS (e.g. Brunetti et al. 2009). However, one of the most important results obtained by means of the $P_{1.4} - L_X$ diagram with the GRHS clusters is the discovery of the *radio bimodality* of galaxy clusters (e.g. Brunetti et al. 2007, 2009). RH clusters indeed trace the $P_{1.4} - L_X$ correlation, while clusters without extended radio emission populate the region of the upper limits, lying about an order of magnitude below the correlation (Fig. 4.6).

It is worth noticing that the discovery of such bimodal behaviour was made possi-

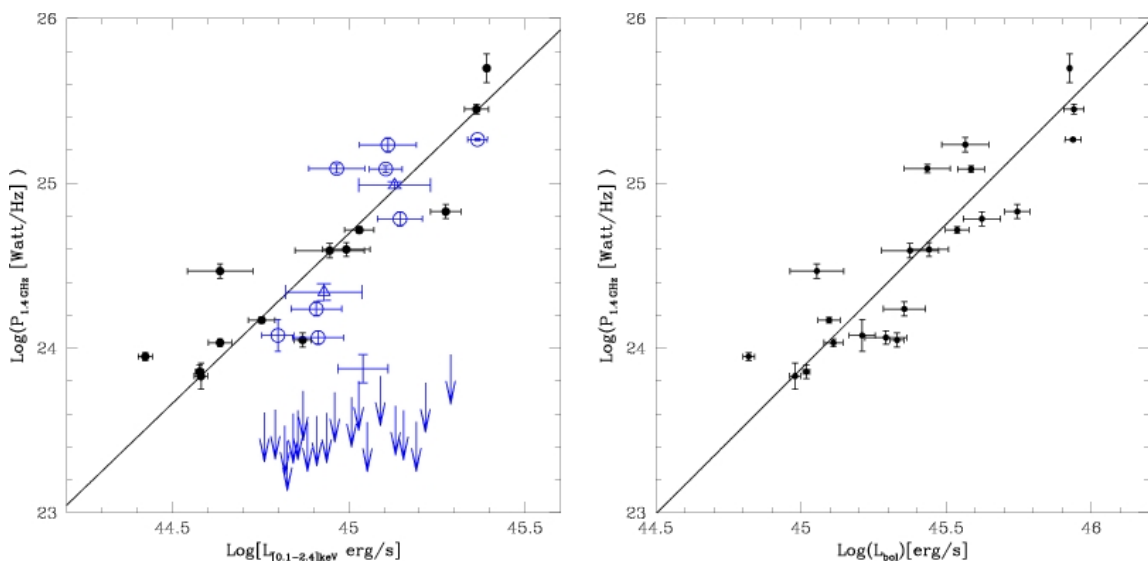


Figure 4.6: Left panel: distribution of GMRT galaxy clusters (blue) and of RH clusters from literature (filled black symbols) in the $P_{1.4} - [0.1 - 2.4]$ keV luminosity plane. Empty circles mark RHs from the GMRT sample, arrows mark upper limits for GMRT clusters with no evidence of Mpc-scale radio emission. The solid line gives the best fit of the distribution of RHs. Right panel: distribution of RHs (GMRT+literature) in the $P_{1.4} -$ bolometric X-ray luminosity plane. The solid line gives the best fit of the distribution of RH (Brunetti et al. 2009).

ble by the fact that firm upper limits on the diffuse emission of cluster without RH have been established. Fig. 4.6 essentially shows that clusters with similar redshift and L_X have a clear bimodal distribution. This is a very crucial issue for the understanding of the origin and evolution of RHs, indeed clusters with similar thermal properties (X-ray luminosity, mass..) are expected to have similar probability to host RHs. In this case the observed difference on the non-thermal properties should be understood in terms of different evolutionary stages.

The RH-merger connection, suggested by e.g. V08, may explain the separation between RH and “radio quiet” clusters in term of different dynamical status. Apart from the detailed mechanisms that origin RHs, the evolutionary cycle can be summarized as follows:

- (1) galaxy clusters host RHs for a period of time, in connection with merger events, and populate the $P_{1.4} - L_X$ correlation;
- (2) then, when clusters become dynamically relaxed, the synchrotron emission is gradually suppressed and clusters fall into the region of the upper limits.

In this framework, the empty region is expected to be populated by (a) “intermediate” systems at late merging phase where synchrotron emission is being suppressed, or (b) by very young systems at the beginning of the merging phase, where synchrotron emission is increasing. Hence, assuming that RHs are transient phenomena connected with the cluster merging phase, the emptiness of the region between RHs and upper limits in the $P_{1.4} - L_X$ diagram becomes a tool to constrain the time-scale of the evolution (amplification and suppression) of the synchrotron emission in galaxy clusters. The significant lack of clusters in the intermediate region suggests that this time-scale is much shorter than both the cluster life-time and the RH life-time (which is the time clusters spend on the correlation). Brunetti et al. (2007) found that the life-time of RHs is $\tau_{RH} \approx 1$ Gyr (in agreement with theoretical models, see Sec. 3.2) and the time-scale for the suppression (or amplification) of synchrotron emission from the level of RHs to that of radio quiet (or vice versa) is $\tau \approx 90$ Myr. Monte Carlo analysis of the distribution of clusters in the $P_{1.4} - L_X$ plane shows that the time interval that clusters spend in the empty region is $\tau_{evol} \approx 200$ Myr with the probability that τ_{evol} being as large as $1 \text{ Gyr} \leq 1\%$ (Brunetti et al. 2009). This statistical analysis provides more quantitative support to the previous results.

The evolution of the radio properties of galaxy clusters in the $P_{1.4} - L_X$ diagram reflects the evolution of relativistic particles and magnetic field in the ICM. The tight constraints on the time-scale of this evolution provides crucial information on the physics of the particle acceleration and magnetic field amplification.

If we consider the secondary electron model, we can explain the clusters radio bimodality by assuming that the passage of mergers shock through the ICM may increase the protons energy density enhancing the rate of production of secondary electrons and the resulting cluster-scale synchrotron emission. However, protons

have very long life-time and the production rate of secondary electrons would remain basically unchanged during cosmic time, moreover, this mechanism doesn't predict the suppression of the synchrotron emission when clusters turn back to the relaxed phase. Therefore, in the context of secondary electron models, RHs are expected to be long-living and common phenomena and there is no reason to expect a radio bimodality².

A possible explanation of the bimodality is that cluster mergers amplify the cluster magnetic field in the ICM enhancing the synchrotron emission on Mpc scales. To explain a suppression ≥ 10 of the synchrotron emission from the RH phase to the radio quiet one (Fig. 4.6) the ratio between the magnetic field in RHs, $B + \delta B$ and that in clusters with upper limit, B , must be:

$$\left(\frac{B + \delta B}{B}\right)^{\alpha-1} \frac{1 + (B_{CMB}/B)^2}{1 + (B_{CMB}/(B + \delta B))^2} \geq 10 \quad (4.2)$$

In the case $B + \delta B \ll B_{CMB}$ secondary models must admit that the energy density of the magnetic field in radio quiet clusters is ≥ 100 times smaller than that in RHs, and even larger if $B + \delta B \gg B_{CMB}$. Even if, theoretically, it is possible to admit that the magnetic field is amplified by turbulence during mergers and later dissipated, this scenario is not supported by present observations. Faraday rotation measurements (e.g. Carilli & Taylor 2002) and more recent studies of polarization (Bonafede et al. 2011) indeed don't show any statistical difference between the energy density of the large scale magnetic field in radio quiet clusters and clusters hosting RHs. Furthermore, even if the magnetic field is amplified by cluster mergers, the dissipation of this magnetic field through the decay of cluster-MHD turbulence is expected to take too long time (\approx a few Gyr, Subramanian et al. 2006). Such a time is inconsistent (larger than) with the time-scale of the suppression of the synchrotron emission inferred from the $P_{1.4} - L_X$ diagram analysis.

Present data suggest that the magnetic field does not play a fundamental role in the evolution of non-thermal properties in galaxy clusters, therefore relativistic electrons must drive the generation and suppression of RHs.

As discussed in Sec. 3.2, cluster mergers inject turbulence on large scale in the ICM and, as soon as turbulence reaches small, resonant, scales, particles are accelerated and generate synchrotron emission at GHz frequencies. The cascading of turbulence from large to small scales is expected to take ≈ 100 Myr, during this time the clusters move from the region of the upper limits to the $P_{1.4} - L_X$ correlation and should appear dynamically disturbed. At the end of the merging phase turbulence starts to dissipate, the synchrotron power is suppressed and the synchrotron emission at higher frequencies falls below the detection limit of radio observations. Clusters move back to the region of the upper limits and appear as relaxed systems in the X-rays.

²Although some attempts have been made assuming that spatial diffusion of CR plays a role, decreasing the level of synchrotron emission in relaxed clusters (Enßlin et al. 2011)

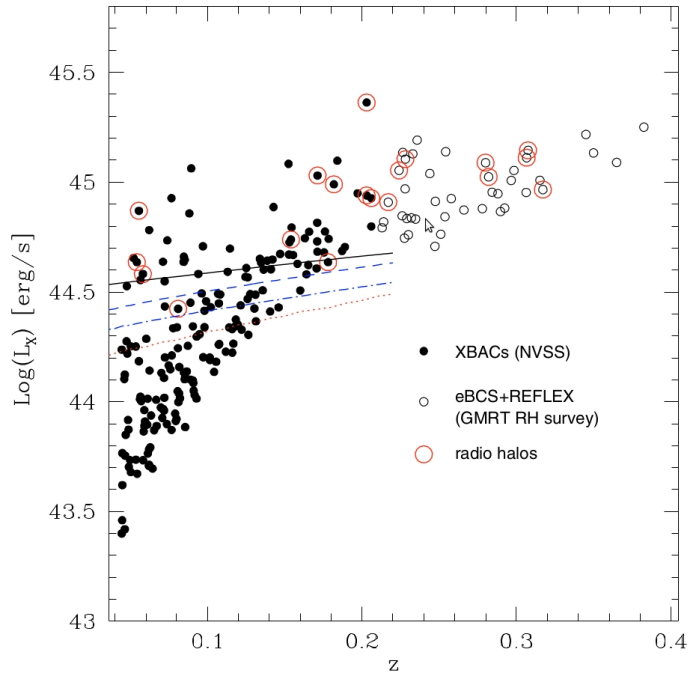


Figure 4.7: X-ray luminosity (0.1-2.4 keV) versus z for the total sample of clusters (XBACs+REFLEX+eBCS) used by Cassano et al. (2008). Open black circles are clusters belonging to the GRHS. Open red circles indicate the clusters with known giant RHs. The lines give the lower limit to the cluster X-ray luminosities calculated by adopting three different approaches (Cassano et al. 2008).

4.2.3 Occurrence of Radio Halos

Seminal attempts were made to understand whether the fraction of clusters hosting RHs depends on cluster X-ray luminosity (Giovannini et al. 1999; Kempner & Sarazin 2001). However it is not clear how much those results were affected by the sensitivity limit of the adopted radio survey.

More recently, Giovannini et al. (2009, 2011) discussed the possible presence of RHs in underluminous X-ray clusters ($L_X < 2 \times 10^{44}$ erg/s), but the number of these cases is still low and statistical studies are necessary to understand their nature and connection with RHs hosted by X-ray luminous galaxy clusters. An important step forward in this sense has been achieved by Cassano et al. 2008 that presented a statistical analysis of the occurrence of RHs in a X-ray-selected sample of galaxy clusters accounting for both radio and X-ray selection biases. They combined the NVSS-XBAC sample at $z < 0.2$ (Giovannini et al. 1999) and the GMRT subsample at $0.2 \leq z \leq 0.4$ (Fig. 4.7). They calculated the fraction of clusters with RHs in the population of low luminosity (LL) and high luminosity (HL) clusters. $L_X = 10^{44.9}$ was chosen as the transition value for the luminosity between the two bins because such value provides a good statistic in both the LL and HL bin and ensures that

the HL clusters cover the luminosity interval where the occurrence of RHs seems to increase.

Their main finding was that the fraction of clusters hosting RHs increases with increasing the X-ray luminosity (hence the mass) of the cluster, in particular they claimed that the percentage of clusters at $z \approx 0.044 - 0.32$ with $4 \times 10^{44} \text{erg/s} < L_X < 8 \times 10^{44} \text{erg/s}$ hosting RHs is $7.5 \pm 3.8\%$, while the percentage of clusters with $L_X \geq 8 \times 10^{44} \text{erg/s}$ hosting RHs is $40.6 \pm 11.2\%$.

In order to test the statistical strength of this result, they ran Monte Carlo simulations finding that the observed difference in percentage between the two luminosity bins is real, with a significance of 3.7σ . This means that the probability to have the observed fraction of clusters with RHs by chance is $\leq 0.2 \times 10^{-3}$.

The increase of the probability to form RHs with increasing the cluster mass is a unique expectation of the turbulent re-acceleration scenario, since a more efficient particle acceleration is triggered in massive (X-ray luminous) systems during clusters mergers (see Sec 3.4). Therefore the jump in the occurrence of RHs from the LL bin to the HL one gives clear support to the model of turbulent re-acceleration, once the $L_X - M_V$ correlation is assumed.

In Fig. 4.8 we report the fraction of clusters hosting RHs (f_{RH}) derived by Cas-

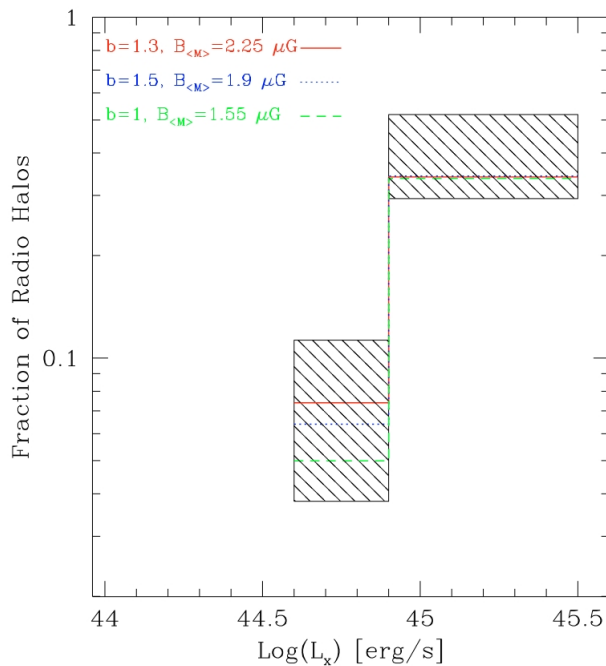


Figure 4.8: Expected fraction of clusters with RHs in the HL and LL subsamples (different coloured lines) vs the X-ray luminosity, overlaid on the observed value of f_{RH} , with 1σ Poissonian errors (shadowed regions)(Cassano et al. 2008).

sano et al. (2008) for different values of the model parameters (different lines) as a function of the X-ray luminosity, overlaid on the observed values of f_{RH} (shadowed

region). The theoretical behaviour of the occurrence of RHs with the cluster mass matches the observed f_{RH} , meaning that the observed jump in the fraction of clusters with RH in the two mass bins can be well reconciled with model expectations.

4.2.4 Merger-Radio Halo connection

There is general consensus on the fact that RHs are found in clusters showing evidence of dynamical activity, such as substructure in the X-ray images, as well as complex gas temperature distribution (Schuecker et al. 2001; Govoni et al. 2004; Markevitch & Vikhlinin 2001). In particular Buote (2001) performed the first quantitative evaluation of the dynamical status of RH clusters discovering a correlation between the RH luminosity at 1.4 GHz and magnitude of the dipole ratio P_1/P_0 . Venturi et al. (2008) extended the analysis of the dipole ratios to the P_3/P_0 parameter, which is related to the presence of multiple peaks in the X-ray image, and to the P_2/P_0 ratio, that can be considered a measurement of the clusters ellipticity. They found a sort of separation in the $P_1/P_0 - P_3/P_0$ plane between relaxed and disturbed clusters, with all RH clusters in the “merging region” and all the relaxed ones lacking extended radio emission.

The very first demonstration that clusters with RH and clusters without RH can be quantitatively differentiated according to their dynamical status was provided by Cassano et al. (2010), using archival Chandra X-ray data of clusters belonging to the GRHS. Their sample consisted of 32 clusters with $0.2 < z < 0.4$, $L_X \geq 10^{44} \text{erg s}^{-1}$ all with radio (GMRT+VLA) and X-ray (Chandra) data. Since they were interested in the cluster dynamical properties on those scales where energy is mostly like dissipated, they studied the cluster substructure inside an aperture radius of 500 kpc.

To provide a quantitative measurement of the dynamical status and the degree of disturbance of galaxy clusters, Cassano et al. (2010) used three methods: power ratios (e.g., Buote & Tsai 1995; Jeltama et al. 2005; Ventimiglia et al. 2008; Böhringer et al. 2010), the emission centroid shift (e.g. Mohr et al. 1993; Poole et al. 2006; O’Hara et al. 2006; Ventimiglia et al. 2008; Maughan et al. 2008; Böhringer et al. 2010), and the surface brightness concentration parameter (e.g. Santos et al. 2008). It is worth describing here these methods since they have been used during the Thesis work (see Chapter 5).

1) *The power ratio method*

The basic idea of the power ratio method is that the X-ray surface brightness represents the projected mass distribution of the galaxy cluster. The power ratio represents the multipole decomposition of the two-dimensional mass distribution inside a circular aperture R_{ap} . Power ratio can be defined as:

$$P_0 = [a_0 \ln(R_{ap})] \quad (4.3)$$

where a_0 is the total intensity inside the aperture radius: $A_0 = s(< R_{ap})$, $S(x)$ is the X-ray surface brightness, and

$$P_m = \frac{1}{2m^2 R_{ap}^{2m}} (a_m^2 + b_m^2) \quad (4.4)$$

where the moments a_m and b_m are given by:

$$a_m(R) = \int_{R' \leq R_{ap}} S(x')(R') \cos(m\phi') d^2x' \quad (4.5)$$

and

$$b_m(R) = \int_{R' \leq R_{ap}} S(x')(R') \sin(m\phi') d^2x' \quad (4.6)$$

we will only make use of the P_3/P_0 parameter that is related to the presence of multiple peaks in the X-ray distribution providing a clear substructure measure (Buote et al. 2001, Böhringer et al. 2010).

2) *The centroid shift method*

The centroid shift is computed in a series of circular apertures centred on the cluster X-ray peak. Starting from $R_{ap} = 500$ kpc, the radius of the aperture is decreased of 5% at every step until $0.05R_{ap}$, and the centroid shift, w , was defined as the standard deviation of the projected separation between peak and the centroid in unit of R_{ap} , i.e.:

$$w = \left[\frac{1}{N-1} \sum (\Delta_i - \langle \Delta \rangle)^2 \right]^{1/2} \times \frac{1}{R_{ap}} \quad (4.7)$$

Δ_i is the distance between the X-ray peak and the centroid of the i th aperture. The shift between the centroid and the X-ray peak is very sensitive to the dynamical status of the cluster (Poole et al. 2006).

3) *The concentration parameter method*

Following Santos et al. (2008) we define the concentration parameter as the ratio between the peak and the ambient surface brightness:

$$c = \frac{S(r < 100 \text{ kpc})}{S(< 500 \text{ kpc})} \quad (4.8)$$

The concentration parameter allows to distinguish clusters with compact core (not disrupted by recent mergers) from cluster with a spread distribution of gas in the core, that suggests that a recent episode of merging has disturbed the cluster dynamics.

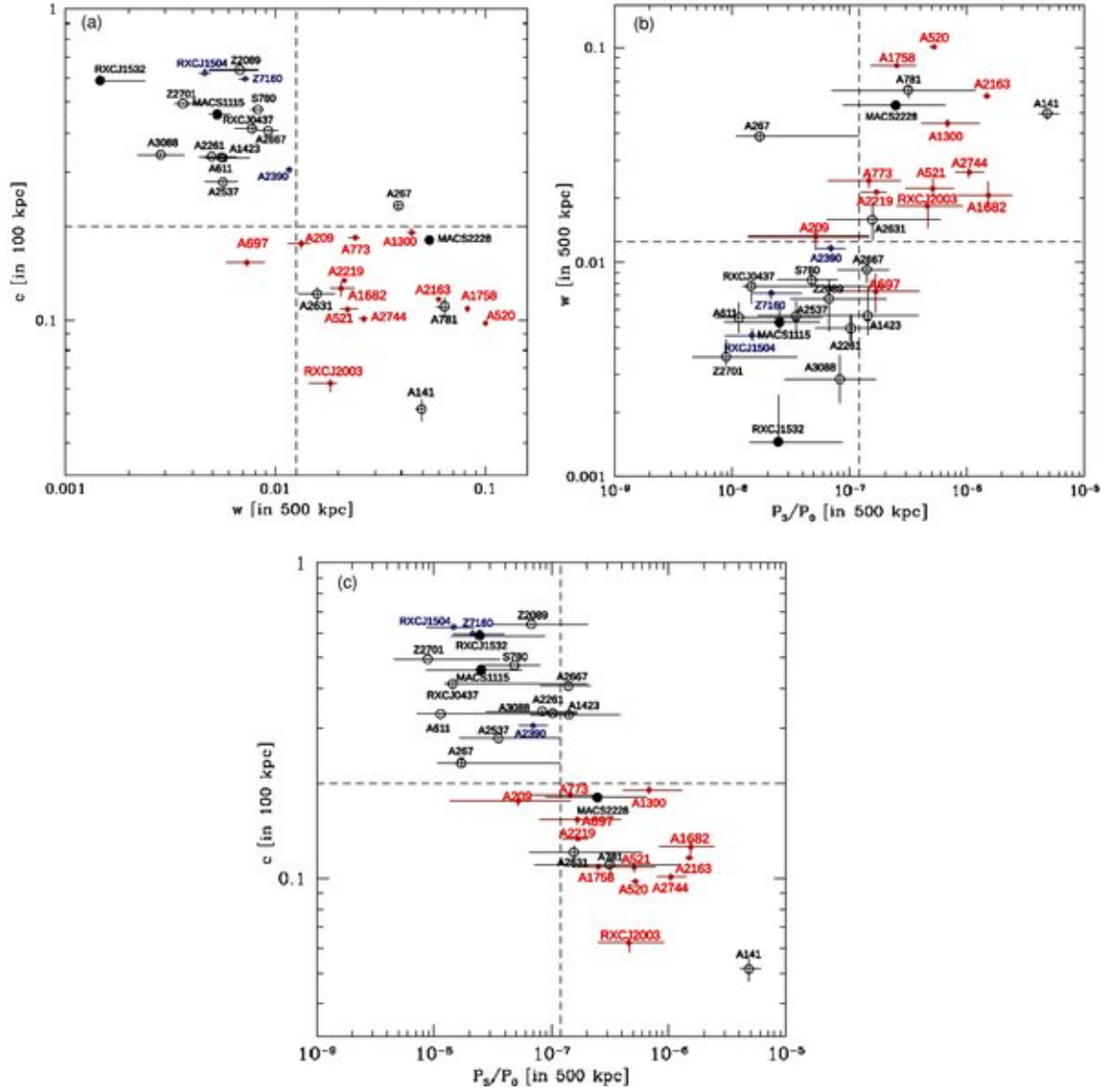


Figure 4.9: (a) Concentration parameter, c , vs. centroid shift, w ; (b) w vs. power ratio parameter, P_3/P_0 ; (c) c vs. P_3/P_0 . Symbols: RH (red filled dots), no RH (black open dots), mini-halos (blue open dots), and $z > 0.32$ (gray filled dots). Vertical and horizontal dashed lines: $c = 0.2$, $w = 0.012$ and $P_3/P_0 = 1.2 \times 10^{-7}$ (Cassano et al. 2010).

It is worth noticing that, since everything we measure is projected on the sky, these methods are no sensitive to the presence of substructures (and thus mergers) along the line of sight.

Basically, higher is the value of c , more relaxed is the cluster, while higher are the values of w and/or P_3/P_0 , more disturbed is the cluster.

Cassano et al. (2010) found a clear anti-correlation between the concentration and the centroid shift parameters (c, w), and between the concentration parameter and the power ratio ($c, P_3/P_0$), while they found a correlation between the centroid shift and the power ratio parameters ($w, P_3/P_0$) (Fig. 4.9 (a),(c) and (b) respectively). Vertical and horizontal lines in Fig. 4.9 represent the median value of each parameter. Most importantly, RH clusters (red filled dots) can be well separated from clusters without RH (black open dots) in all diagrams. However c is the parameter that provides the best separation between RH and no-RH clusters, indeed no RH is found in clusters with $c > 0.2$. These diagrams confirm the hypothesis that RHs form in dynamically disturbed clusters, while clusters without diffuse radio emission are relaxed systems. To test quantitatively this result, Cassano et al. (2010) ran Monte Carlo simulations on the (c, w) plane, finding that the probability to have such segregation between RH and non RH clusters by chance is of the order of $(3 - 4) \times 10^{-5}$, thus ensuring, from a statistical point of view, the connection between RHs and cluster mergers.

4.3 The Extended GRHS

The GMRT Radio Halo Survey had an extraordinary success in the statistical analysis of the observational properties of RHs, as demonstrated by the results shown in previous Sections. To improve the statistical significance of these results, Kale et al. (2013) have undertaken the Extended GMRT Radio Halo Survey (EGRHS). From the REFLEX and the eBCS X-ray catalogues, they selected clusters with:

- L_X (0.1-2.4 keV) $\geq 5 \times 10^{44}$ erg/s
- $0.2 \leq z \leq 0.4$
- $\delta \geq -30^\circ$ for the REFLEX and EBCS samples.

Basically, the declination limit while selecting clusters from the X-ray samples has been extended with respect to the GRHS. These new selection criteria added 17 clusters to the 50 clusters of the GRHS leading to a final sample of 67 clusters, which we will refer to as the EGRHS.

The extension of the sample essentially confirmed previous findings:

- new upper limits lye factors ~ 3 -20 times below the expected radio power based on the $P_{1.4} - L_X$ correlation;

- The fraction of RHs in the EGRHS sample is $31\pm 11\%$ in clusters with high X-ray luminosity ($L_X > 8 \times 10^{44}$ erg/s) and $11\pm 7\%$ in clusters with lower X-ray luminosity ($5 - 8 \times 10^{44}$ erg/s).

4.4 Radio-SZ correlation & bimodality

The principal parameter of the theoretical models for the origin and evolution of RHs is the cluster mass. In order to have a prompt comparison between observation and model expectations, large mass-selected samples of galaxy clusters with adequate radio and X-ray data are necessary. The recent advent of the Planck satellite allows to investigate the formation of RHs in SZ-selected cluster samples (Basu 2012; Cassano et al. 2013; Sommer & Basu 2014). The attempt to better constrain RHs statistical properties by selecting clusters using the SZ effect is driven by the fact that the SZ signal is a better indicator of the cluster mass with respect to the cluster X-ray emission (Carlstrom et al. 2002).

Basu (2012) cross correlated the Planck ESZ cluster catalogue (Panck Collaboration 2011a) with radio data from GRHS. He found a correlation between the radio power and the integrated SZ signal, but he did not find a strong indication of a bimodal behaviour of galaxy clusters in the $P_{1.4} - Y_{SZ}$ plane (Fig. 4.10). To explain the apparent lack of bimodality, Basu (2012) suggested that X-ray observations could be biased towards the detection of low mass cool-core clusters, whereas the SZ selection picks up the most massive systems independently on their dynamical status. Cassano et al. (2013) suggested, however, that this result was rather due to the small completeness ($\sim 25\%$) of the cluster sample used by Basu (2012). In particular, to test the bimodality against the presence of cool-core clusters in the EGRHS, they corrected the X-ray luminosity of the parent cluster by modelling the X-ray brightness distribution and excising the cool-core and then they derived the distribution of clusters in the $P_{1.4} - L_{500,cor}$ diagram: as expected, the X-ray luminosity of cool-core clusters is significantly reduced by the correction (cool-core clusters shift to lower luminosities going from L_{500} to $L_{500,cor}$). However, the bimodal behaviour is still present in both the diagrams in Fig. 4.11. This allows to conclude that the observed radio bimodality is not driven by the presence of cool-core (X-ray luminous, but not necessary massive) clusters without diffuse radio emission.

The PSZ catalogue used by Cassano et al. 2013 (Planck collaboration 2013) is six times the size of the PSZ catalogue used by Basu (2012) and it is 80% complete for $M_{500} \gtrsim 6 \times 10^{14} M_\odot$ at $z \simeq 0.2 - 0.35$, typical values for the EGRHS. Fig. 4.12 shows the distribution of clusters in the $P_{1.4} - Y_{500}$ (right panel) and in the $P_{1.4} - M_{500}$ (left panel) planes. A clear correlation between the radio power of RHs and both Y_{500} and M_{500} of the hosting cluster is present. In a generic form we can write:

$$\log \left(\frac{P_{1.4}}{10^{24.5} \text{Watt/Hz}} \right) = B \log \left(\frac{Y_{500}}{10^{-4} \text{Mpc}^2} \right) + A \quad (4.9)$$

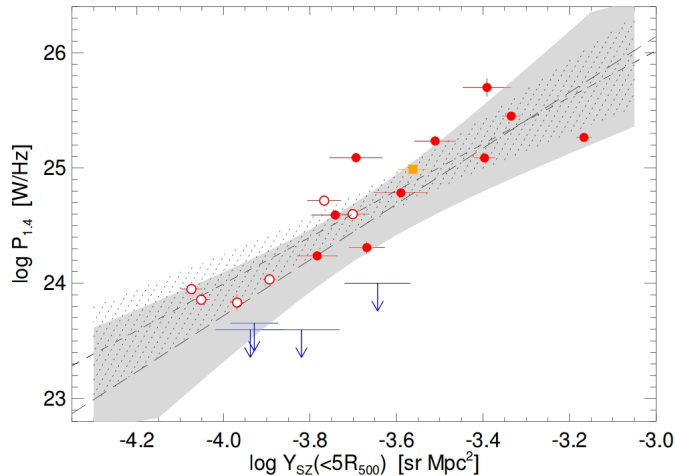


Figure 4.10: Correlation of radio power against the total SZ signal: filled symbols are for $z > 0$ cluster halos, and open symbols are for lower redshifts. The sample is from Brunetti et al. (2009) (Basu 2012).

and

$$\log \left(\frac{P_{1.4}}{10^{24.5} \text{ Watt/Hz}} \right) = B \log \left(\frac{M_{500}}{10^{14.9} M_{\odot}} \right) + A \quad (4.10)$$

The slope of the $P_{1.4} - Y_{500}$ correlation is ~ 2 , in agreement with precedent findings (Basu 2012). The slope of the $P_{1.4} - M_{500}$ correlation is 3.77 ± 0.57 or 4.51 ± 0.78 , depending on the fitting method, in both cases steeper than the previous estimates based on different definitions of the cluster mass (Feretti 2003; Cassano et al. 2006). At variance with Basu (2012), Cassano et al. (2013) found a clear bimodality in both diagrams (Fig. 4.12). At least for $Y_{500} \gtrsim 6 \times 10^{-5}$ (corresponding to $M_{500} \gtrsim 5.5 \times 10^{14} M_{\odot}$), RH clusters follow the trend between their radio power and the SZ signal, while clusters with upper limits lie well below the 95% confidence regions of the best-fit correlations (Fig. 4.12).

It seems that the fraction of clusters hosting RHs using SZ-selected samples is larger than that measured using X-ray clusters samples (Sommer & Basu 2013), probably because the SZ and the X-ray signals from the ICM have distinct time evolution during cluster mergers. Simulations indeed indicate that the merger induced boost in the SZ signal is much smaller and delayed in time with respect to the X-ray signal (Sommer & Basu 2014). Sommer & Basu (2014) compared the RH “dropout” fraction (i.e. the fraction of clusters that do not host a RH) in two cluster samples, selected on the basis of different mass proxy, in the redshift range $z = 0.1 - 0.4$. Specifically, they used an X-ray selected sample based on the REFLEX, eBCS, NORAS and MACS catalogues and an SZ selected sample based on the Planck PSZ catalogue. These samples were cross-checked with the NVSS to search for diffuse radio emission. They measured the diffuse emission in the central region of the

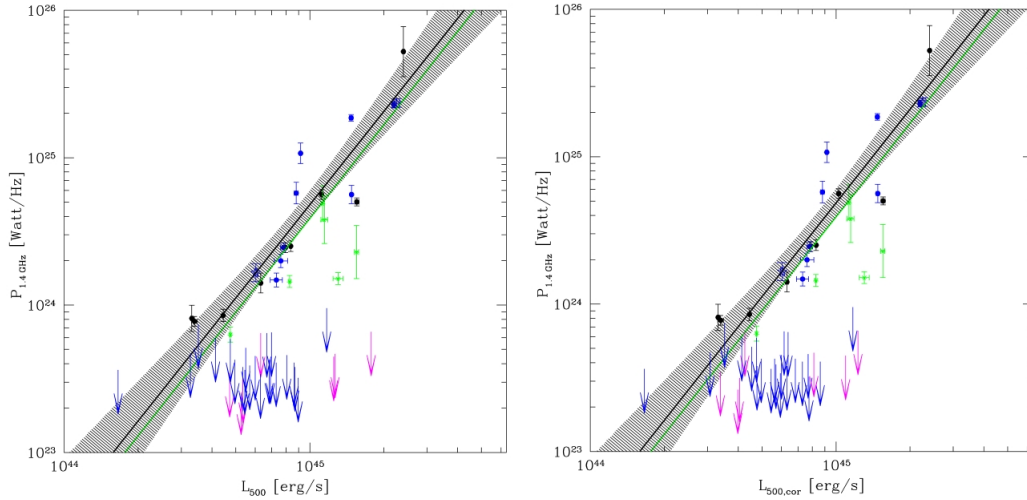


Figure 4.11: Left panel: distribution of clusters in the $P_{1.4} - L_{500}$ plane. Right panel: distribution of clusters in the $P_{1.4} - L_{500,cor}$ plane. In both panels different symbols indicate: EGRHS halos (blue filled dots), halos from literature (black open dots), USSRH (green asterisks). The black lines represent the best fit relation to RHs and the shadowed regions are the 95% confidence (Cassano et al. 2013).

clusters, after having removed the point sources using different filtering techniques. They modelled the relation between the radio power and mass observables with a power law and a “dropout” fraction quantifying the fraction of objects without central diffuse radio emission (Fig. 4.13). It is worth noticing that the procedure applied by Sommer & Basu doesn’t allow to distinguish between RH and non RH clusters, therefore, the “dropout” fraction is only provided by means of statistical methods. They found that the “dropout” fraction, g is $\approx 70\%$ in the X-ray-selected sample, while it is consistent with $\approx 0\%$ in the SZ-selected one, suggesting that the vast majority of massive SZ-selected clusters host RHs. However, they have been unable to infer whether and how the “dropout” fraction varies with the cluster mass.

Despite of these recent efforts to link the presence of RHs in galaxy clusters to their mass, an exhaustive analysis of the occurrence of RHs in large mass-selected samples of galaxy clusters is still missing. The measure of the formation rate of RHs in galaxy clusters and its dependence on the the cluster thermal properties, such as mass and temperature, provides unique information on the physics and the origin of these sources. For these reasons, collecting large mass-selected samples of galaxy clusters and improving the analysis on the occurrence of RHs and on their connection with clusters merger is of fundamental importance.

Actually this Thesis work is aimed at providing an unbiased measure of the fraction of clusters hosting RHs and of its dependence on the cluster mass in a nearly complete mass-selected sample of galaxy clusters.

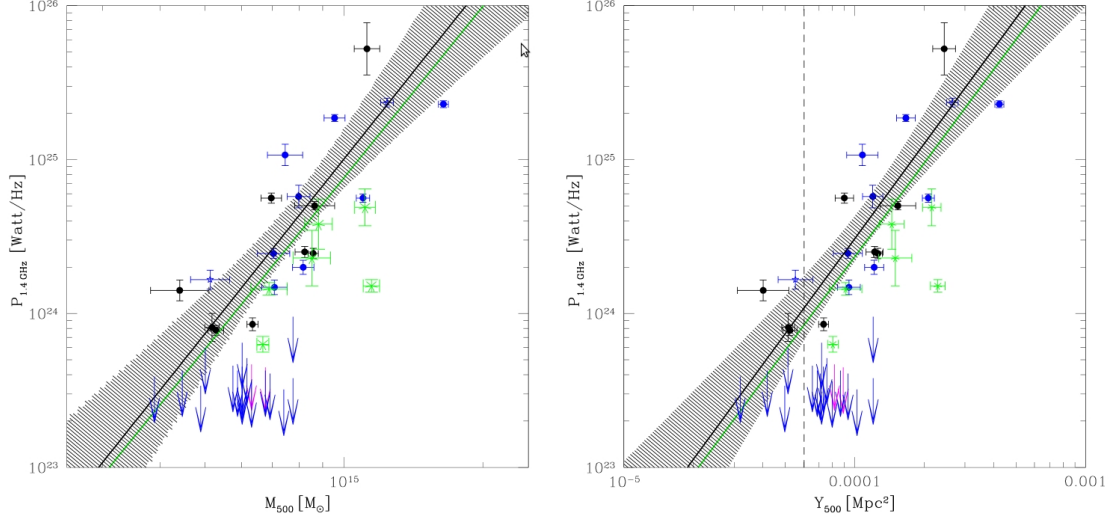


Figure 4.12: Left panel: distribution of clusters in the $P_{1.4} - M_{500}$ plane. Right panel: distribution of clusters in the $P_{1.4} - Y_{500}$ plane. In both panels different symbols indicate: EGRHS halos (blue filled dots), halos from literature (black open dots), USSRH (green asterisks). The black lines represent the best fit relation to RHs. Dashed line in the right panel marks the value $Y_{500} = 6 \times 10^{-5} \text{ Mpc}^2$ (Cassano et al. 2013).

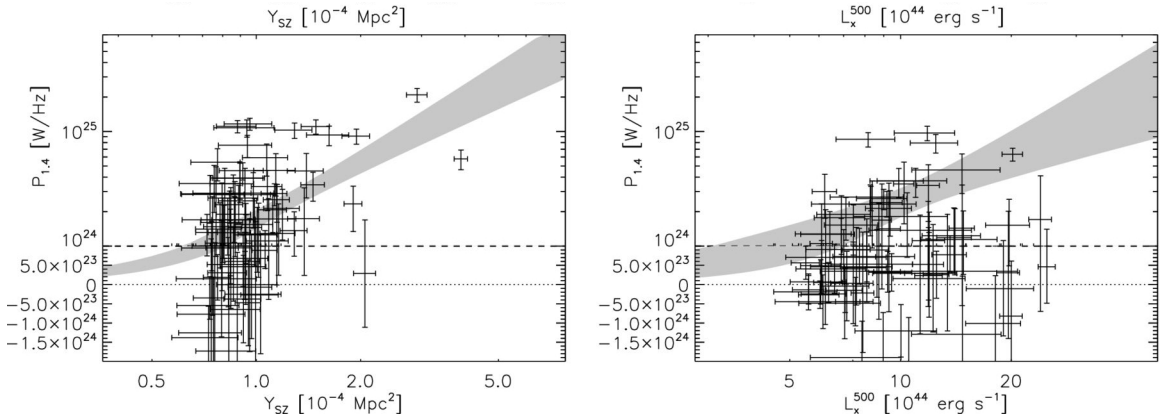


Figure 4.13: NVSS radio power plotted against Y_{SZ} for the PSZ (left panel) and X-ray (right panel) sub-samples. The grey shaded region in each panel represents the 68% confidence region of the best-fitting power law (Sommer & Basu 2014).

Chapter 5

Sample selection & data analysis

So far the statistical properties of RHs have been investigated in X-ray-selected cluster samples (see Chapter 4 and references therein). The comparison between model predictions and observations have been performed by assuming the $L_X - M$ relation to convert the observed cluster X-ray luminosity into cluster mass, being the latter needed by models. The cluster mass is indeed the key parameter of models for the RH formation, because gravity provides the energy for particle acceleration during mergers. Although the existence of a good correlation between the cluster mass and the X-ray luminosity is well established (e.g. Arnaud et al. 2005; Pratt et al. 2009; Maughan et al. 2012), possible biases in the mass determination from the X-ray luminosity have also been investigated. For example, the X-ray luminosity of cool-core clusters might be enhanced by the presence of the core (which increases the X-ray emissivity) with respect to clusters with similar mass, in these cases, the mass of cool-core clusters might be overestimated when derived from the X-ray luminosity (Pratt et al. 2009; Zhang et al. 2011). Simulations of cluster mergers show that the X-ray luminosity of a cluster can be boosted up during mergers (Sarazin, 2002; O'Hara et al. 2006; Poole et al. 2007) and this might lead to an overestimation of the cluster mass. On the other hand, the mass can be underestimated in those cases where the merger has completely destroyed the core and the X-ray brightness distribution of the cluster is very flat, as suggested by the observations in the X-ray of clusters newly discovered via the SZ effect (Planck Collaboration 2011, 2012, 2013), which are on average merging systems, underluminous for their mass compared to X-ray selected clusters.

One possibility to overcome all these problems in the cluster mass determination is to use SZ-selected cluster samples. Because of the very tight correlation between the total SZ signal, Y , and the cluster mass (e.g. Da Silva, 2004; Nagai 2006; Wik et al. 2008; Angulo et al. 2012) SZ-selected samples are very close to be mass-selected samples. In this regard the advent of the Planck Satellite has a fundamental role since it allowed, for the first time, to collect large, and highly complete, SZ-selected samples of galaxy clusters.

This Thesis work is aimed at studying the occurrence of RHs as a function of

the cluster mass and their connection with the clusters dynamical activity. For this purpose, from the Planck SZ catalogue (Planck Collaboration XXIX 2013), we selected clusters with $M \gtrsim 6 \times 10^{14} M_{\odot}$ in the redshift range $z = 0.08 - 0.33$ and we searched for the presence of RHs by using the NVSS for low redshift clusters ($z < 0.2$) and the EGRHS for high redshift ones ($z > 0.2$). We also made use of the Chandra X-ray data to investigate the dynamical status of these clusters.

In this Chapter we present our mass-selected cluster sample and we describe the radio and X-ray data reduction we performed in order to identify RH clusters and to get information on the clusters dynamical status.

5.1 The Planck catalogue

The catalogue we used is the result of the first 15.5 months of Planck survey observations (Planck Collaboration XXIX 2013) in the frequency range 100-857 GHz, with the Planck angular resolution being ~ 5 -10 arcmin. The Survey area used for the SZ detections in Planck is the 83.7% of the sky coverage. To date the Planck sample is the largest SZ-selected cluster sample and the deepest all-sky catalogue spanning the broadest cluster mass range from 0.1 to $1.6 \times 10^{15} M_{\odot}$.

After the identification of SZ sources, the cluster-candidate catalogue undergoes a validation process that permits to identify previously known clusters and to assemble crucial information, such as the cluster redshifts. For this purpose, X-ray (MCXC), optical (Abell and Zwicky, then SDSS), SZ catalogues (SPT and ACT) and the NED and SIMBAD was used, in this order. At the same time, follow up observations with Chandra and XMM-Newton are used to derive the X-ray properties of the new SZ-discovered candidate clusters. Cluster masses are derived from the SZ proxy assuming the scaling between Y_{500} and M_{500} given in Planck Collaboration XX (2013):

$$E^{-2/3}(z) \left[\frac{D_A^2(z) Y_{500}}{10^{-4} \text{Mpc}^2} \right] = 10^{-0.19} \left[\frac{M_{500}}{6 \times 10^{14} M_{\odot}} \right]^{1.79} \quad (5.1)$$

where $E^2(z) = \Omega_m(1+z)^3 + \Omega_{\Lambda}$ computed in the Λ CDM cosmology and D_A is the angular diameter distance. Fig. 5.1 illustrates the $M - z$ distribution of the Planck-SZ catalogue. The limiting mass M_{lim} , computed following Planck Collaboration XX (2013), is also shown for three values of completeness: 20%, 50% and 80%. In Fig. 5.1 we also highlight (red and blu rectangles) the areas of the $M - z$ plane from which our sample is extracted. It should be noted that we selected regions where the PSZ catalogue has a mass-completeness $\gtrsim 80\%$.

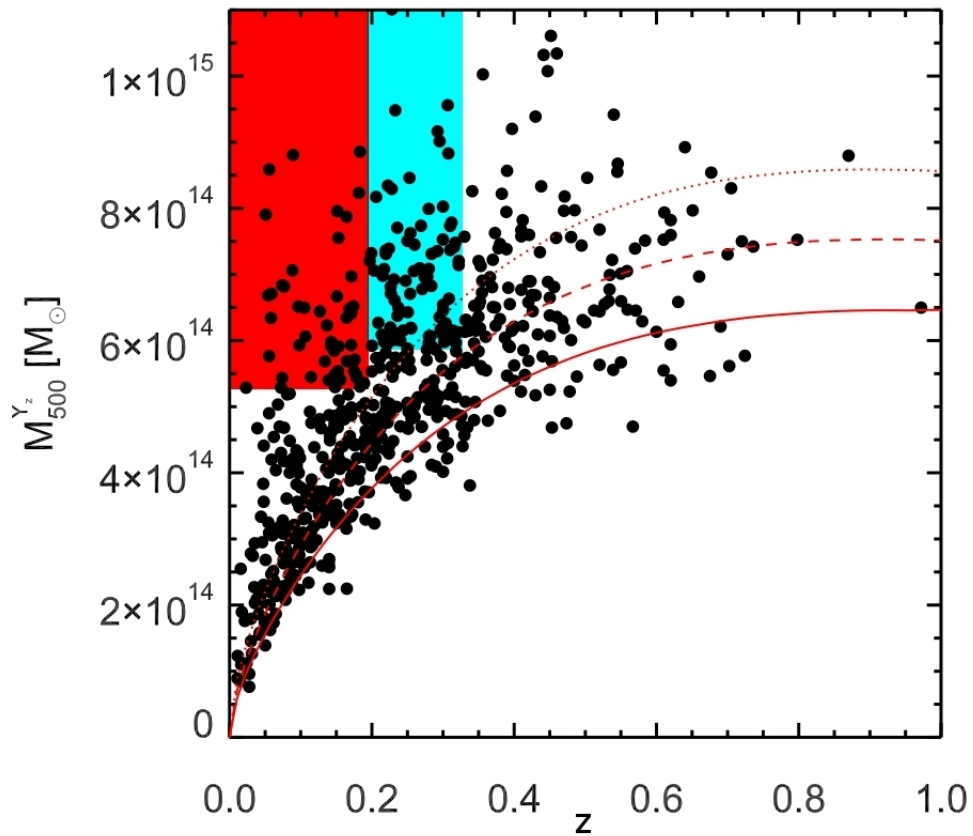


Figure 5.1: Average mass limit computed from the average noise over the sky for the PSZ catalogue. The dotted, dashed and solid lines show the Planck mass limit at 80, 50 and 20 % completeness respectively. The rectangles show the regions from where we extracted the two subsamples: the red rectangles for the low redshift subsample, the cyan rectangle for the high redshift one.

5.2 The low redshift sample

The low redshift sample consists of all the clusters in the Planck-SZ (PSZ) catalogue with

- $M \gtrsim 5.7 \times 10^{14} M_{\odot}$
- $0.008 < z < 0.2$

and visible in the NRAO VLA Sky Survey (NVSS, Condon et al. 1997), i.e. with $\delta > -40^{\circ}$. With the adopted selection criteria, the low- z sample is made of 21 clusters.

The NVSS is a radio survey performed at 1.4 GHz with the Very Large Array (VLA) in D and DnC configuration. It covers the sky north of $\delta = -40^{\circ}$, it has an angular resolution of $45''$ and the surface brightness rms is 0.45 mJy/beam.

The lower redshift limit ($z > 0.08$) is driven by the fact that radio interferometers suffer from the lack of sampling at short baselines, resulting in decreased sensitivity to emission on large spatial scales, e.g. Mpc-scale RHs. Farnsworth et al. (2013) have recently analysed the fractional recovery of extended emission in the NVSS. It has been demonstrated that for emission on scales larger than $\sim 11'$, less than 50% of the total flux density is recovered with a NVSS snapshot observation; at size scales of $15'$ only $\sim 10\%$ of the flux density is recovered. This becomes important at very low redshift since 1 Mpc halo at $z=0.1$ (0.08) would subtend roughly 9 (11) arcmin. For this reason we included in our sample only clusters with $z > 0.08$.

The upper redshift limit ($z < 0.2$) instead is based on three different considerations. Since the surface brightness decreases with $(1+z)^4$, the NVSS low sensitivity makes this survey only suitable for low- z objects. Moreover, the NVSS low angular resolution does not allow to separate the point sources from the extended emission and this problem progressively becomes worse with increasing redshift (a beam of $45''$ at $z = 0.2$ corresponds to a linear scale of 150 kpc). Most importantly, for clusters at $z > 0.2$ deep radio data from the EGRHS are available.

The mass cut at $5.7 \times 10^{14} M_{\odot}$ is due to the NVSS detection limit. Indeed, as a starting point, we had chosen clusters with $M \geq 5.5 \times 10^{14} M_{\odot}$ and this leads to a sample of 25 clusters, among which 13 had literature information about the presence/absence of diffuse radio emission. The other 12 clusters needed further investigation to be classified as RH or non RH clusters. First of all, we had to understand whether we could be able to detect a RH in these clusters with the NVSS. Since known RHs follow a well defined correlation between their synchrotron radio power and the mass of the hosting clusters, it is possible that the smaller clusters in the sample host RHs with low radio powers, non detectable in the NVSS. We assumed that all these clusters host a RH and, since we know their M_{500} , we used the $P_{1.4} - M_{500}$ correlation (Eq. 4.10) to derive their expected radio power, (we used the best fit parameters $A = 0.125$ and $B = 3.77$, see Cassano et al. 2013). Following Cassano et al. (2012) we estimated the minimum flux density of a halo that

can be detected by the NVSS, requiring that the mean halo brightness within half halo radius ($0.5\theta_H$) is ξ_1 times the noise level in the map, i.e. $0.5f_{min}/N_b \approx \xi_1 F_{rms}$, where N_b is the number of independent beams within $0.5\theta_H$ and F_{rms} is the rms noise per beam. This gives:

$$f_{min}(z) \simeq 1.2 \times 10^{-4} \xi_1 \left(\frac{F_{rms}}{10 \mu Jy} \right) \left(\frac{100 \text{ arcsec}^2}{\theta_b^2} \right) \left(\frac{\theta_H^2(z)}{\text{arcsec}^2} \right) \text{ mJy} \quad (5.2)$$

where $\theta_H(z)$ ¹ is the angular size of the RH at a given redshift in arcseconds and θ_b is the beam angular size in arcseconds. For the NVSS $F_{rms} = 0.45 \text{ mJy/b}$ and $\theta_b = 45''$.

Fig. 5.2 shows the distribution of the clusters without literature information in the $P_{1.4} - z$ diagram, where $P_{1.4}$ is the expected radio power of the halo hosted by a cluster with a given mass. The red line represents the NVSS detection limit assuming $\xi_1 = 1.5$ in Eq. 5.2. We remark that, even if the clusters under the red line hosted RHs, they would not have been detected, since their expected RH flux density is below the NVSS detection limit. Based on this result we removed from the sample those clusters lying below the red line, which are clearly the less massive ones.

The final low- z sample includes 21 clusters, whose properties are listed in Tab. 5.1 together with the available X-ray information for each cluster.

¹Here the typical RH radius is assumed to be 600 kpc.

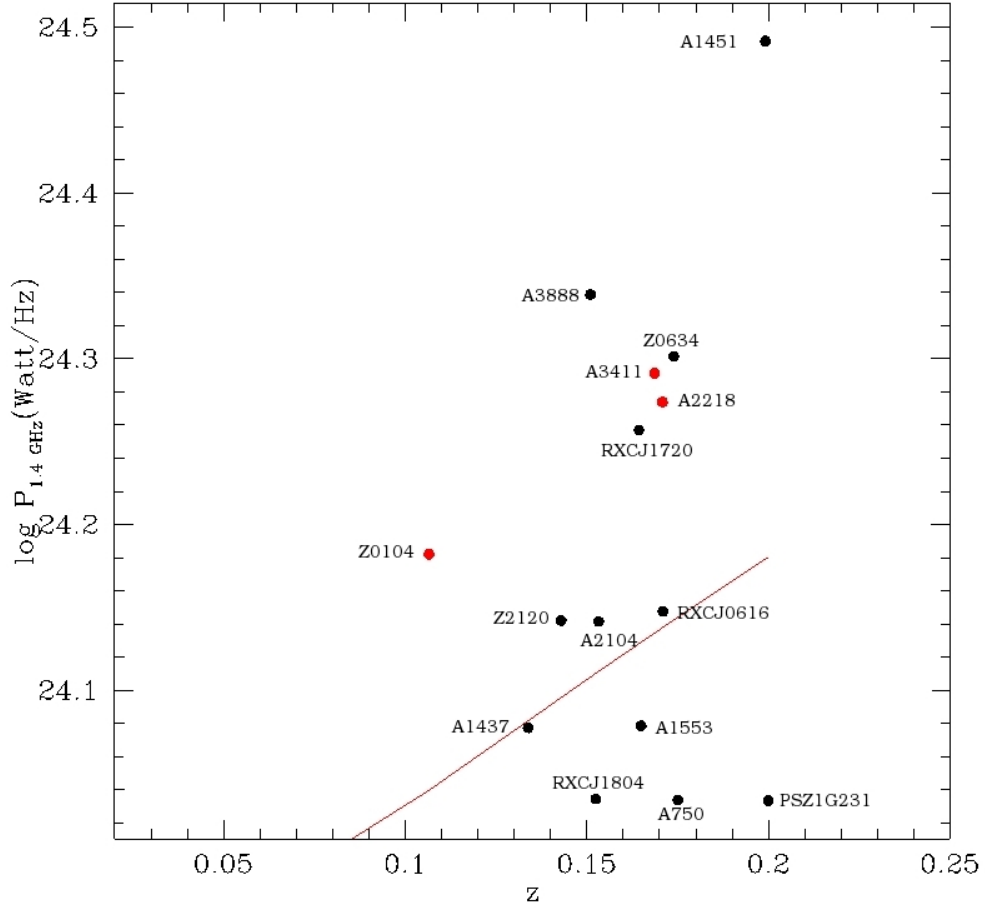


Figure 5.2: $P_{1.4} - z$ diagram for clusters at $0.08 < z < 0.2$. $P_{1.4}$ is computed assuming that all clusters follow the $P_{1.4} - M_{500}$ correlation. The red line represent the NVSS detection limit (using $\xi_1 = 1.5$). Red points represent three known RHs, namely Zwcl 0104.9+5350, A2218 and A3411 for comparison.

Table 5.1: Low redshift sample clusters properties.

cluster name	RA	Dec	z	M_{500} ($10^{14} M_{\odot}$)	Radio info	X info
A1437	12 00 22.3	+03 20 33.9	0.134	5.69	no RH ✓	Rosat
A2345	21 27 06.8	-12 07 56.0	0.176	5.71	Relic	Chandra
A2104	15 40 08.2	-03 18 23.0	0.153	5.91	no RH ✓	Chandra
Zwcl 2120.1+2256	21 22 27.1	+23 11 50.3	0.143	5.91	no RH ✓	Chandra
RXC J0616.3-2156	06 16 22.8	-21 56 43.4	0.171	5.93	no RH ✓	RASS
A1413	11 55 18.9	+23 24 31.0	0.143	5.98	MH	Chandra
Zwcl 0104.9+5350	01 07 54.0	+54 06 00.0	0.107	6.06	RH	Rosat
A1132	10 58 19.6	+56 46 56.0	0.134	6.23	no RH	Chandra
RXJ1720.1+2638	17 20 10.1	+26 37 29.5	0.164	6.34	no RH ✓	Chandra
A2218	16 35 51.6	+66 12 39.0	0.171	6.41	RH	Chandra
A3411	08 41 55.6	-17 29 35.7	0.169	6.48	RH	Chandra
Zwcl 0634.1+4750	06 38 02.5	+47 47 23.8	0.174	6.52	suspect ✓	Chandra
A3888	22 34 26.8	-37 44 19.1	0.151	6.67	suspect ✓	XMM-Newton
A1914	14 26 03.0	+37 49 32.0	0.171	6.97	RH	Chandra
A478	04 13 20.7	+10 28 35.0	0.088	7.06	MH	Chandra
A115	00 55 59.5	+26 19 14.0	0.197	7.21	Relic	Chandra
A1451	12 03 16.2	-21 32 12.7	0.199	7.32	suspect ✓	XMM-Newton
A2204	16 32 45.7	+05 34 43.0	0.151	7.96	no RH	Chandra
A665	08 30 45.2	+65 52 55.0	0.182	8.23	RH	Chandra
A2142	15 58 16.1	+27 13 29.0	0.089	8.81	RH	Chandra
A1689	13 11 29.5	-01 20 17.0	0.183	8.86	RH	Chandra

The symbol ✓ indicates clusters we have analysed in this work.

5.3 The high redshift sample

For the high redshift ($0.2 < z < 0.33$) sample we cross-checked the PSZ catalogue with the EGRHS. The selection criteria are:

- $M \geq 6 \times 10^{44} M_{\odot}$
- $0.2 < z < 0.33$
- $\delta > -30^{\circ}$
- $|b| \geq \pm 20^{\circ}$, where b is the galactic latitude.

These selection criteria led to a sample of 54 clusters, 33 of which have available information (EGRHS, VLA archive or literature information) about the presence of diffuse radio emission. We report on the properties of the 33 clusters belonging to the high redshift sample in Tab 5.2. The remaining 21 clusters have not been classified as RH or no RH clusters so far, for different reasons. In Tab. 5.3 we list these clusters and we summarize the reasons why we did not include them in our sample. In Tab. 5.2 “UL” marks clusters with available Upper Limits on the Mpc-scale flux density derived in V07, V08.

The case of the EGRHS observations is different from that of the NVSS subsample, the former are indeed lower frequency observations (600 MHz) and are much deeper ($1\sigma \sim 35 - 100 \mu\text{Jy}/\text{beam}$) than the NVSS, since they aimed at the detection of RHs. This guarantees that the detection of extended diffuse emission at the level expected from the $P_{1.4} - L_X$ correlation is not biased by the sensitivity limit of those observations, as demonstrated by the bimodal distribution of RH and UL in the $P_{1.4} - L_X$ diagram.

Table 5.2: High redshift sample clusters properties.

cluster name	RA	Dec	z	M_{500} ($10^{14} M_{\odot}$)	Radio info	X info
A1576	12 37 59.0	+63 11 26.0	0.302	5.98	UL	Chandra
A2697	00 03 11.8	-06 05 10.0	0.232	6.01	UL	XMM-Newton
RXC J0142.0+2131	01 42 02.6	+21 31 19.0	0.280	6.07	UL	Chandra
A1423	11 57 22.5	+33 39 18.0	0.214	6.09	UL	Chandra
RXC J1314.4-2515	13 14 28.0	-25 15 41.0	0.244	6.15	RH	XMM-Newton
A2537	23 08 23.2	-02 11 31.0	0.297	6.17	UL	Chandra
A1682	13 06 49.7	+46 32 59.0	0.226	6.20	RH	Chandra
A781	09 20 23.2	+30 26 15.0	0.295	6.36	UL	Chandra
A3088	03 07 04.1	-28 40 14.0	0.254	6.71	UL	Chandra
A2667	23 51 40.7	-26 05 01.0	0.226	6.81	UL	Chandra
A521	04 54 09.1	-10 14 19.0	0.248	6.91	RH	Chandra
A2631	23 37 40.6	+00 16 36.0	0.278	6.97	UL	Chandra
RXC J1504.1-0248	15 04 07.7	-02 48 18.0	0.215	6.98	MH	Chandra
A520	04 54 19.0	+02 56 49.0	0.203	7.06	RH	Chandra
A773	09 17 59.4	+51 42 23.0	0.217	7.08	RH	Chandra
A1351	11 42 30.8	+58 32 20.0	0.322	7.14	RH	Chandra
PSZ1 G205.07-62.94	2 46 27.5	-20 32 5.29.0	0.310	7.37	no RH ^p	XMM-Newton
A2261	17 22 17.1	+32 08 02.0	0.224	7.39	UL	Chandra
RXCJ2003.5-2323	20 03 30.4	-23 23 05.0	0.317	7.48	RH	Chandra
A3444	10 23 50.8	-27 15 31.0	0.254	7.62	no RH, UL?	Chandra
S780	14 59 29.3	-18 11 13.0	0.236	7.71	UL	Chandra
A1758a	13 32 32.1	+50 30 37.0	0.280	7.99	RH	Chandra
A209	01 31 53.0	-13 36 34.0	0.206	8.17	RH	Chandra
A1763	13 35 17.2	+40 59 58.0	0.228	8.29	no RH	Chandra
RXC J1514.9-1523	15 14 58.0	-15 23 10.0	0.223	8.34	RH	RASS
A1835	14 01 02.3	+02 52 48.0	0.253	8.46	MH	Chandra
A1300	11 31 56.3	-19 55 37.0	0.308	8.83	RH	Chandra
A2390	21 53 34.6	+17 40 11.0	0.234	9.48	MH	Chandra
A2744	00 14 18.8	-30 23 00.0	0.307	9.56	RH	Chandra
A2219	16 40 21.1	+46 41 16.0	0.228	11.01	RH	Chandra
PSZ1 G171.96-40.64	11 27 50.4	-40 38 24.0	0.270	11.13	RH	RASS
A697	08 42 53.3	+36 20 12.0	0.282	11.48	RH	Chandra
A2163	16 15 46.9	-06 08 45.0	0.203	16.44	RH	Chandra

^p Ferrari et al. (private communication).

cluster name	RA	Dec	z	M_{500}	Information
Z5247	12 33 56.1	+09 50 28.0	0.229	6.04	GMRT analysis in progress
A2895	01 18 11.1	-26 58 23.0	0.228	6.15	poor quality data ^b
A68	00 37 05.3	+09 09 11.0	0.255	6.19	GMRT analysis in progress
A56	00 33 50.4	-07 47 28.0	0.300	6.20	poor quality data ^a
A402	02 57 41.1	-22 09 18.0	0.322	7.21	MH? ^p
RXC J0510.7-0801	05 10 47.9	-08 01 44.0	0.220	7.36	GMRT analysis in progress
A2552	23 11 26.9	+03 35 19.0	0.300	7.53	GMRT analysis in progress
RXC J2135.2-0102	21 35 00.0	-01 02 17.0	0.33	7.57	locked VLA ^c
A1443	12 01 27.7	+23 05 18.0	0.269	7.74	poor quality data ^a , locked VLA ^c
A2813	00 43 27.4	-20 37 27.0	0.292	9.16	poor quality data ^b
Zwcl 1028.8+1419	10 31 28.2	+14 03 34.0	0.31	6.11	
A3041	02 41 22.1	-28 38 13.0	0.23	6.12	
RXC J2051.1+0216	20 51 08.0	+02 15 55.0	0.32	6.13	
A2472	22 41 50.6	+17 31 43.0	0.31	6.15	
A348	02 48 13.9	-02 16 32.0	0.24	6.38	
RXC J1322.8+3138	13 22 48.8	+31 39 17.0	0.31	6.63	
A220	01 37 19.5	+07 56 16.0	0.33	6.74	
A2355	21 35 22.5	+01 23 26.0	0.23	6.92	
A1733	13 27 03.7	+02 12 15.0	0.26	7.05	
PSZ1 G019.12+3123	16 36 29.4	+03 08 51.0	0.28	7.08	
PSZ1 G139.61+2420	06 22 13.9	+74 41 39.0	0.27	7.09	

Table 5.3: Clusters not included in the sample. (a) VLA archival data analysed in the present work, (p) Macario private communication, (b) GMRT data with $\text{rms} > 130 \mu\text{Jy}/\text{beam}$ (Venturi et al. 2007, 2008), (c) L-BAND VLA observations in C and D configuration. The lower part of the table contains clusters without available radio data (GMRT+VLA proposal submitted).

5.4 Radio data analysis

In this Section we describe the radio data reduction and analysis carried out during this Thesis work on clusters lacking detailed information about the presence of diffuse emission.

We adopted two different approaches for the two subsamples: we analysed (and in some cases reprocessed) NVSS data for the low- z sample clusters, while for clusters at $z > 0.2$ we reduced VLA (array C or D) archival data, when available. In both cases the data analysis was carried out using the standard tasks of the NRAO AIPS (Astronomical Image Processing System) package.

5.4.1 Low- z sample

Among the 21 clusters of the low redshift sample, 13 have literature information about the presence/absence of diffuse radio emission, in form of RH, relics or minihalos (Tab. 5.1). As a first step, for each of the remaining 8 clusters (those marked with the symbol \checkmark in Tab. 5.1) we searched for the X-ray image in the NASA's HEASARC (High Energy Astrophysics Science Archive Research Center) Archive² selecting, in order, the Chandra, XMM-Newton, Rosat and RASS image.

After that, we downloaded, from the NVSS postage stamp server³, the NVSS maps (in FITS format) with size of $0.5^\circ \times 0.5^\circ$ centred on the centroid of the X-ray cluster emission.

In order to have an overall view of the clusters emission, we overlaid the NVSS radio contours on the X-ray image of each cluster. We also retrieved the cluster optical image from the SDSS⁴ (Sloan Digital Sky Survey), when available, since it allows to identify the presence and the location of galaxies in the cluster. An example of this preliminary analysis is shown in Fig. 5.3 in the case of A1451: the radio NVSS contours (green contours) are overlaid on the X-ray XMM-Newton image (upper left panel), on the NVSS map (upper right panel) and on the optical SDSS image (lower panel). As for A1451, the X-ray image is always useful to identify the cluster centre (as the centroid of the X-ray emission) and to visualize its extension. In the specific case of A1451, one can readily note that the radio emission, both from the central and the peripheral regions of the cluster, are due to galaxies visible in the SDSS image.

NVSS data analysis

In this Section we describe the NVSS data analysis, with the aim to investigate the presence/absence of diffuse cluster-scale emission. It is not our goal to measure the

²<http://heasarc.gsfc.nasa.gov>

³<http://www.cv.nrao.edu/nvss/postage.shtml>

⁴<http://www.sdss.org/>

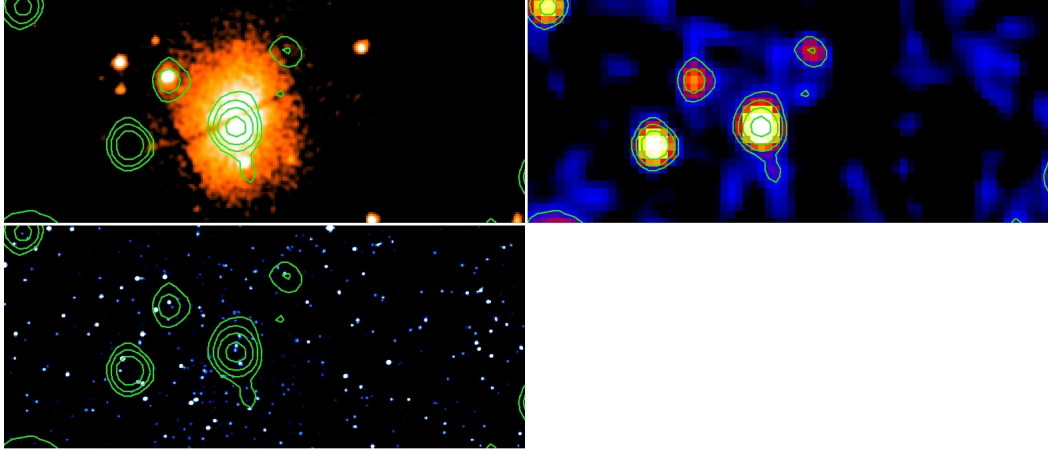


Figure 5.3: A1451 XMM-Newton (upper left panel), NVSS(upper right panel) and SDSS (lower panel) images. The radio contours (green) levels are $0.45 \times (2, 4, 8, 16, 32)$ mJy b^{-1}

true diffuse flux density and to establish the nature of the diffuse emission.

The NVSS is based on more than two hundred thousand “snapshot” observations of the duration of ~ 30 s. The VLA primary power pattern is approximately a circular Gaussian:

$$P(\rho) = \exp[-4 \ln 2(\rho/\theta_P)^2] \quad (5.3)$$

where ρ is the angular distance from the pointing position and θ_P is the primary FWHM, about $31'$ at 1.4 GHz. Sky images much larger than θ_P and having nearly uniform sensitivity can be constructed from weighted sums of partially overlapping snapshot images, each covering most of one primary beam area (Fig. 5.4). Since the primary beam is circular, an hexagonal grid of pointing positions provides the most uniform coverage. The angular distance, Δ , between the pointing positions on this grid is a compromise between the uniformity ($\Delta < \theta_P$) and the observing efficiency, because a larger Δ reduces the number of fields to be observed.

For a set of similar snapshots, the signal-to-noise ratio is simply proportional to the primary power gain. Thus, each snapshot image (which was not corrected for primary-beam attenuation) is multiplied by the primary power pattern $P(\rho)$ before adding it to the large weighted image. This is equivalent to making the normal correction for primary-beam attenuation (dividing by $P(\rho)$) and then multiplying by $P^2(\rho)$.

By the simple visual inspection of the NVSS maps we could not clearly assess the presence of a RH in any cluster. Therefore we proceeded loading the fits files from the NVSS into AIPS, we selected on each map a 1 Mpc sized circle centred on the centroid of the X-ray image. We extracted the total flux density from this region, then we masked the discrete sources in the cluster, with the task BLANK, to measure the remaining diffuse flux density. The residual diffuse flux densities have been then compared with the flux densities measured in other areas around

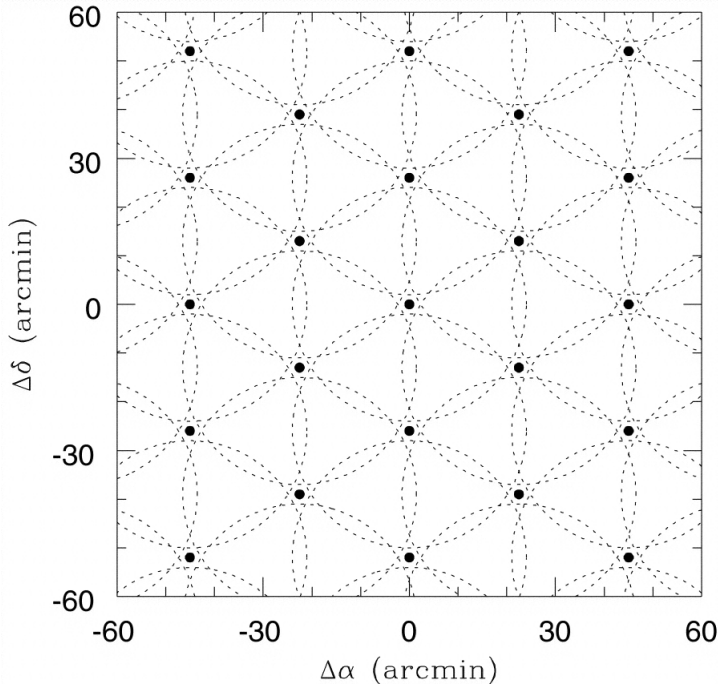


Figure 5.4: The VLA covers the sky uniformly with snapshot images whose pointing centres (filled circles) lie on an hexagonal grid with separation $\Delta = 26'$. The dotted circles indicated the distance from the pointing position at which each snapshot image is truncated.

the cluster (3 for each cluster) of the same size. We will refer to these areas as the “control fields”, since they allow us to compare the diffuse flux density in the central region with the mean residual flux density of empty regions⁵ in the field. For this purpose the control fields should be not far from the cluster centre in order to sample the same region of the sky, but also not too near to the cluster because it is possible that part of its emission extends beyond the X-ray cluster image. Furthermore the control fields should be devoid of sources, however we can also choose some region containing discrete sources and blank them with the same technique adopted for the central region.

Fig. 5.5 gives an example of this procedure applied to the case of A3888, which will be considered as a reference example of our analysis. We also applied this method to 3 known RH clusters (A3411, A2218, Zwcl 0104.9+5350), in order to test our procedure.

For each cluster without literature information, plus the three known RHs, we plotted the diffuse flux density vs. the control field flux densities in Fig. 5.6 (a). We also show the bisector (red line), which is the line where the diffuse flux equals the control fields flux, clusters lying on the left side of the bisector have a diffuse

⁵Here with “empty” we mean devoid of sources.

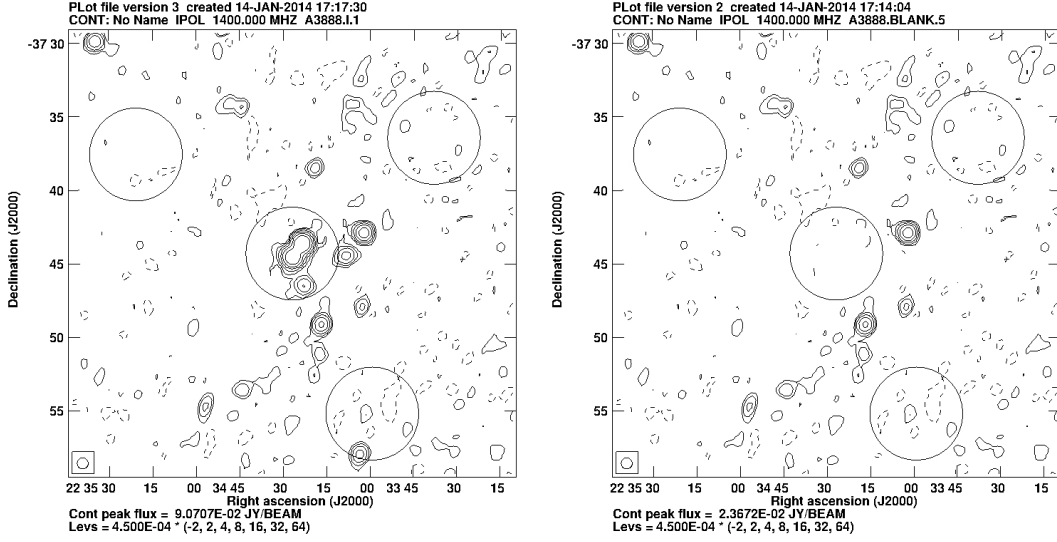


Figure 5.5: A3888 NVSS map, the contour levels are $0.45 \times (2, 4, 8, 16, 32, 64)$ mJy b^{-1} . In both panels the region from where we extracted the flux densities are illustrated (solid circles), the central circle is a 1 Mpc sized circle centred on the centroid of the X-ray emission, the other 3 areas are the so-called control fields. With the task BLANK we masked the discrete sources in the central region and the one that falls in the lower control field (left panel)

residual flux density that overcomes that of the blank regions of the map, therefore they can be considered as clusters with a hint of diffuse radio emission. One would expect to find the three know RHs (black filled dots) in the left region of the diagram, Z0104 and A2218 actually lye there, but A3411 has a very low diffuse flux density and it is comparable with its control fields flux densities. This is not so surprising since A3411 is a well studied cluster and we know that it hosts a low surface brightness RH, whose radio power is lower than that expected from the $P_{1.4} - M$ and $P_{1.4} - L_X$ correlations (Van Weeren et al. 2013).

Fig. 5.7 (a) shows the distribution of the flux densities extracted in the central region (blue histogram) compared to the distribution of the flux densities extracted from the control fields (red histogram). Errors are derived as:

$$\text{err} = \sqrt{rms_A^2 + (0.02) \times F_{obs}} \quad (5.4)$$

where F_{obs} is the measured flux density and rms_A is the number of areas of the beam in the region from which F_{obs} was extracted.

The combination of Fig. 5.6 (a) and Fig. 5.7 (a), suggests a hint of diffuse radio emission in 6 clusters (coloured dots), namely A3888, Zwcl0634.1+4750, A2104, A1451, RXCJ0616.3-2156 and Zwcl2120.1+2256, but this analysis did not allow us to definitely classify them as RH clusters. Thus we decided to reprocess the NVSS data for these 6 clusters, aiming at reducing the rms and the contribution

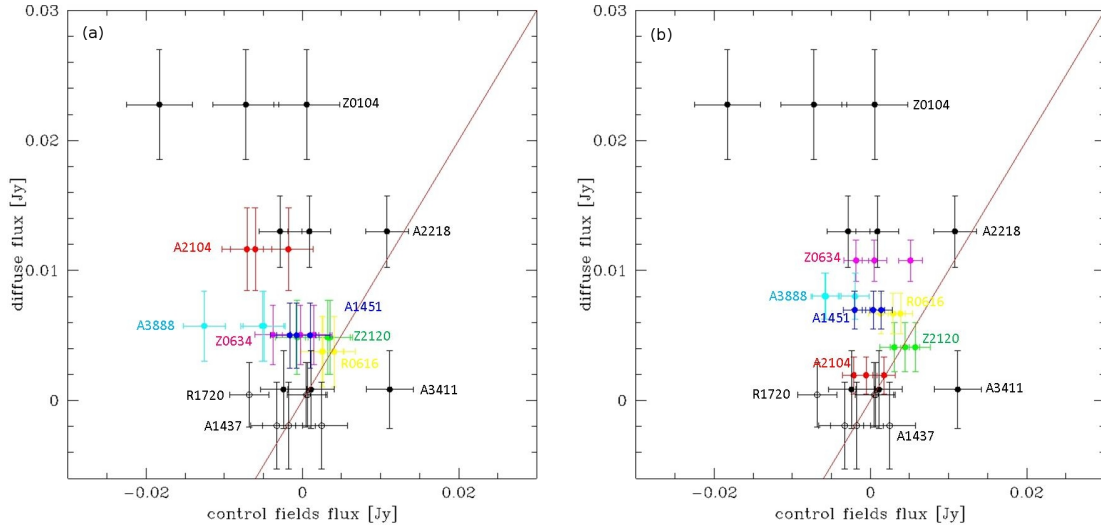


Figure 5.6: Diffuse flux density vs. control fields flux densities for each cluster (a) before and (b) after our NVSS reprocessing. Coloured dots are clusters for which we reprocessed the NVSS dataset. Black dots represent clusters for which we did not perform the NVSS reprocessing because they did not show any hint of diffuse emission in the NVSS (black open dots) or they are known RH clusters (black filled dots). In both panels the red line is the bisector of the plane.

of pattern of positive noise, which can result as diffuse flux density in excess; this might enable us to rule out the presence of RHs or to confirm the presence of suspect diffuse emission with more accuracy.

Reprocessing the NVSS data

To reduce a NVSS dataset we identified the proper file in the VLA archive, we downloaded it and imported into AIPS. The largest difference between a pointed dataset and the NVSS is that, in the majority of the cases, there are two or more pointing positions relevant to the field centre we are considering (see Fig. 5.4) and it is necessary to reprocess separately all the pointings and then combine them with the mosaic technique. Therefore, as a first step we identified all these pointings in the dataset, then, for each pointing, we identified the primary and secondary calibrators, we edited the bad u - v data with tasks like WIPER, TVFLG and/or UVFLG and we proceeded with the amplitude calibration: SETJY VLACALIB (part of VLAPROCS) and CLCAL. Then we calibrated the phase with the secondary calibrator (VLACALIB, GETJY) and apply the calibration to the target with CLCAL. Once the “a priori” calibration was successfully completed, we split the dataset in single source files and we moved on to the imaging (IMAGR). We fi-

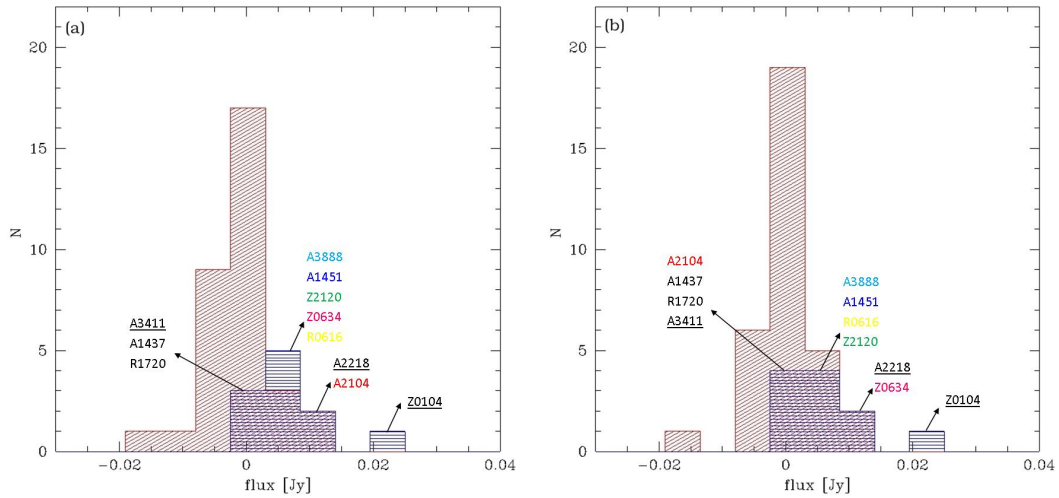


Figure 5.7: Diffuse (blue) flux density distribution and control fields (red) flux density distribution of the 11 clusters of Fig 5.6 (a) before and (b) after our NVSS reprocessing, which has been applied to the clusters marked with coloured names. Black names mark clusters for which we did not perform the NVSS reprocessing because they did not show any hint of diffuse emission in the NVSS (R1729 and A1437) or they are known RH clusters (underlined names).

nally applied the phase self-calibration (CALIB) in order to take into account phase variations on time-scales shorter than the time interval between two scans of the secondary calibrators.

Once the images of the pointings relevant to the cluster centre are obtained, we combined them with the task FLATN. This procedure is fundamental especially when the cluster falls at the border of the primary beam, because the signal to noise ratio decreases with the distance from the pointing position. When one uses the task FLATN to combine maps, the primary beam correction is applied to the maps in order to have the real noise, not attenuated by the instrumental response; then, where the images overlap, they are averaged pixel by pixel. This procedure leads to the increase of the signal to noise ratio in the overlapping region, essentially because there the noise is averaged between the two maps and thus reduced with respect to the single map (Fig. 5.8).

We perform the NVSS reduction for the six clusters in Tab. 5.4 (the six clusters represented with coloured dots in Fig. 5.6), where we report the rms of each map we produced. The rms is measured on the combined maps (.FLATN) with the task TVSTAT, selecting a region devoid of sources as near as possible to the cluster. We reached an average rms ≈ 0.25 mJy/beam, a factor ~ 2 lower with respect to the nominal NVSS rms noise.

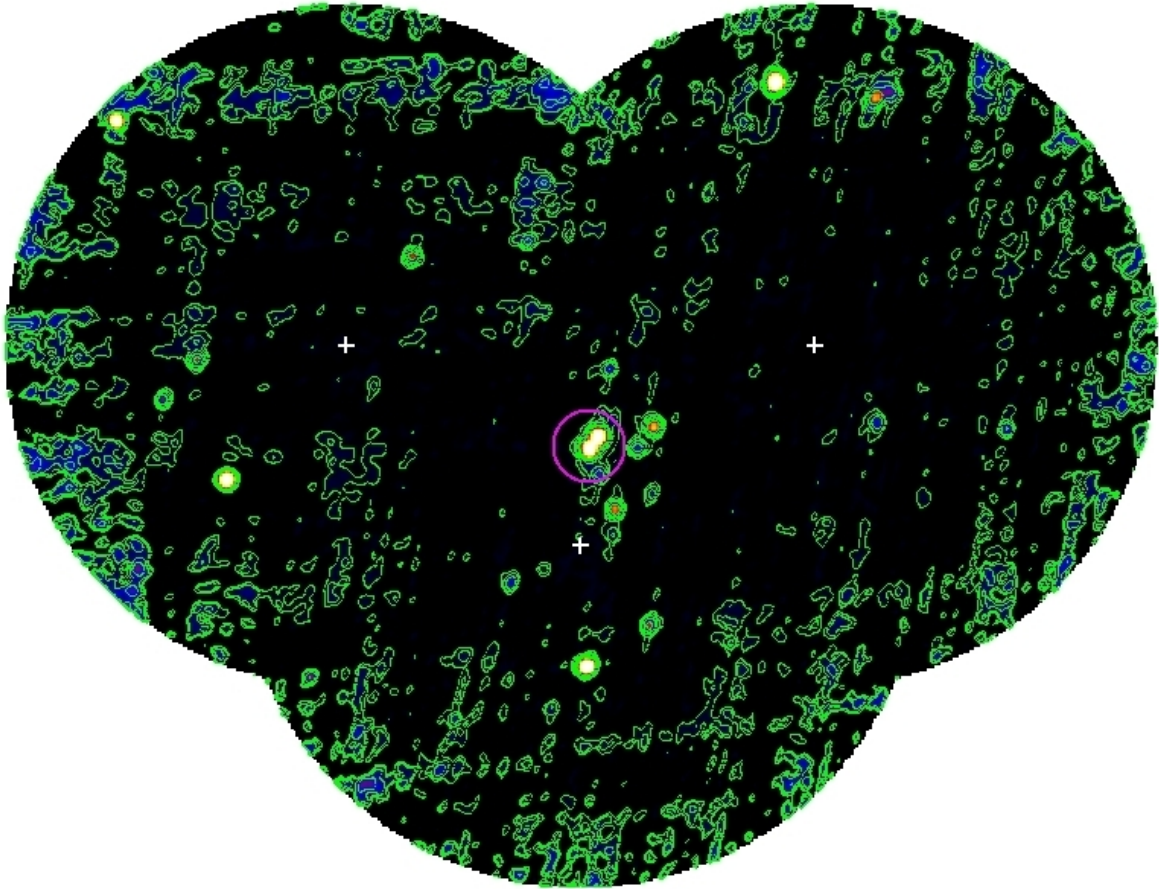


Figure 5.8: A3888 NVSS-reprocessed image, the contour levels are $0.2 \times (2, 4, 8, 16, 32)$ mJy b^{-1} . The three pointings we combined are clearly visible, white crosses mark the pointings centres. The 1 Mpc sized central region is the magenta circle. The cluster centre is nearer to the lower pointing position.

Cluster name	rms (mJy/beam)
A2104	0.26
Zwcl 2120.1+2256	0.25
RXC J0616.3-2456	0.28
Zwcl 0634.1+4750	0.26
A3888	0.23
A1451	0.27

Table 5.4: Rms noises of the NVSS map we have reprocessed. All the rms are taken from the combined maps (.FLATN) with the task TVSTAT selecting a region devoid of sources as near as possible to the cluster.

Estimate of the diffuse flux density

We extracted the diffuse flux densities in the central 1 Mpc region and in the control fields (adopting the regions previously defined) on the reprocessed NVSS images (after masking discrete sources). Fig. 5.6 (b) shows the distribution of clusters in the diffuse-control fields flux density diagram where the flux densities of A3888, Zwcl0634.1+4750, A2104, A1451, RXCJ0616.3-2156 and Zwcl2120.1+2256 are now taken from the reprocessed maps. The lower rms noise in the reprocessed maps allows to measure the flux densities of these six clusters with higher accuracy (as can be seen from the comparison of the coloured dots in Fig. 5.6). We note that the diffuse flux density of A2104 substantially decreases after our reduction, RXCJ0616.3-2156 and Zwcl0634.1+4750 instead have a slightly increase in flux density, while A3888, A1451 and Zwcl2120.1+2256 are still in the same region of the diagram.

Fig. 5.7 (b) shows the distribution of the control fields (red histogram) flux densities and the central circle (blue histogram) flux densities. The comparison between the two panels in Fig. 5.7 reveals the main result of the reprocessing: thanks to the decrease of the rms and the cleaning of noise patterns, control field flux densities are indeed closer to zero in (b) than in (a). However we note that positive residual flux densities are still detected in five clusters, namely Zwcl0634.1+4750, A3888, A1451, RXCJ0616.3-2156 and Zwcl2120.1+2256.

In order to understand, for these 5 cases, how much the residual diffuse flux density differs from the control fields flux densities, for each cluster we considered the average value of the control field flux densities and we calculated the distance of each point from the bisector (that again represents the line where the diffuse flux equals the average control fields flux, Fig. 5.9).

The excesses are shown in Fig. 5.10: small excess means that the residual flux density inside the central 1 Mpc region is consistent with the average flux density of regions devoid of sources selected around the cluster. For this reason we decided to consider the clusters falling into the red ellipse (RXCJ0616.3-2156, Zwcl2120.1+2256) as clusters in which the possible residual of diffuse emission is negligible (<5 mJy), while we will consider A3888, Zwcl0634.1+4750 and A1451 as suspect cases, since their distance from the bisector is larger (between 5 and 10 mJy). Fig. 5.10 also shows the three known RHs, A3411, A2218 and Zwcl 0104.9+5350. As already suggested by Fig 5.6 and 5.7, Fig. 5.10 confirms that RXJ1720.1+2638, A2104 and Zwcl 2120.1+2256 can be considered as clusters without diffuse radio emission, indeed they are inside the red ellipse. Unfortunately the NVSS observations are not sufficient to establish the presence (and nature) of diffuse emission in the three suspect cases, A3888, Zwcl0634.1+4750 and A1451. Deeper observations at low resolution (e.g. VLA array C or D), in order to have a good sensitivity to the diffuse Mpc scale emission, and at high resolution (e.g. VLA array A or B), to make an accurate subtraction of the individual sources from the $u-v$ data, are necessary.

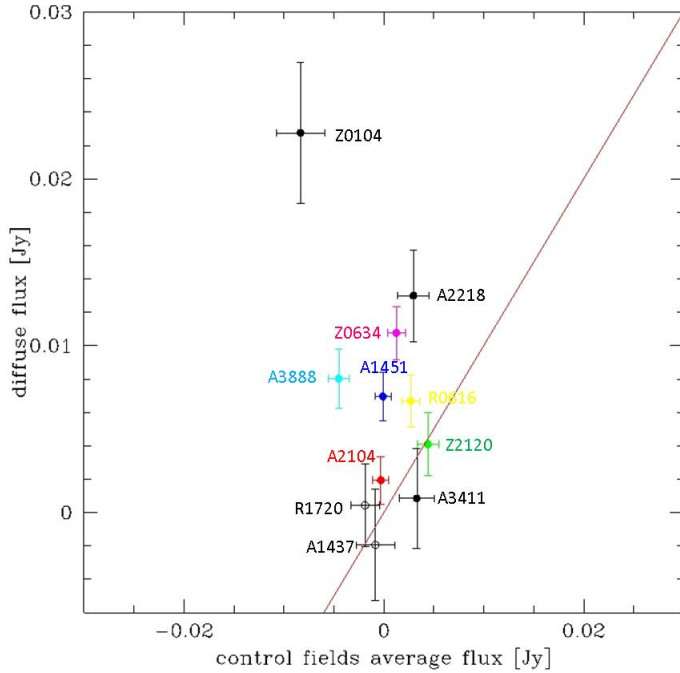


Figure 5.9: Diffuse flux density vs. control fields average flux density. The average values are calculated from the flux densities plotted in Fig. 5.6. Symbols: coloured dots are clusters for which we reprocessed the NVSS datasets; black dots are clusters for which we did not perform the NVSS reprocessing because they did not show any hint of diffuse emission in the NVSS (black open dots) or they are known RH clusters (black filled dots). The red line is the bisector of the plane.

5.4.2 High-z sample

In Tab. 5.3 we list the clusters which have been excluded from the high redshift sample. The two clusters marked with ^a, namely A56 and A1443 had archival VLA data which we analysed during this Thesis work. Here we briefly summarize the data reduction we carried out on these two clusters and the observational problems that led us to keep them out of the sample.

A56 has archival VLA observation in array D and L band (1400 MHz). We loaded this dataset into AIPS and we performed the same calibration procedure adopted for the NVSS (see previous Section) with the only difference that in this case there is a single pointing position corresponding to the cluster centre.

This dataset appeared problematic since the first look at the $u-v$ data, lot of editing was needed. We removed one antenna because it always gave bad data and we excised some baselines. The calibration using the first and secondary calibrator was carried out, then we re-examined the calibrated data and we removed the remaining bad data. We split the dataset and we imaged the data of the target, several

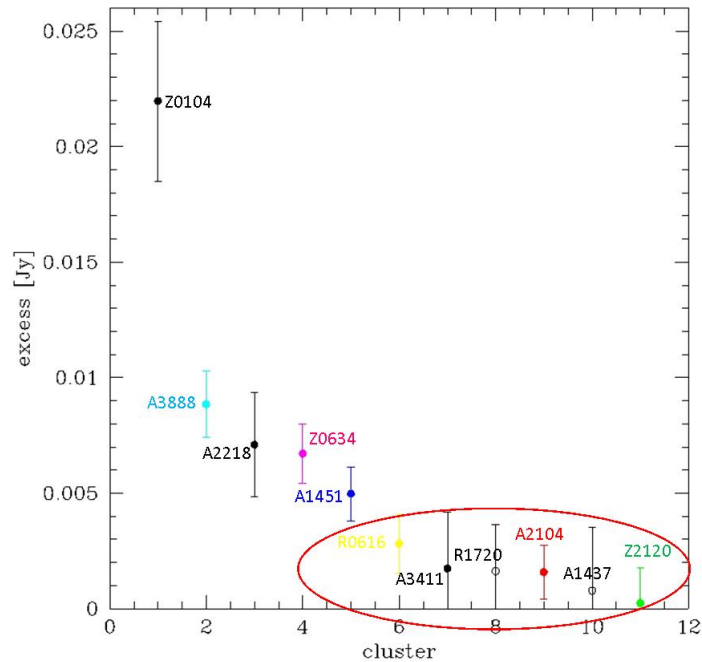


Figure 5.10: Distances between the points in Fig. 5.9 and the bisector. Symbols are the same as in Fig. 5.9. Clusters inside the red ellipse are hereafter considered as objects without diffuse radio emission since their diffuse flux density is actually comparable with the median flux density of regions devoid of sources.

iterations of phase self calibration were performed and finally we applied an amplitude self-calibration. However the rms did not drop below 0.2 mJy/beam, which is comparable to that of an NVSS reprocessed map (Tab. 5.4). As a consequence, we are not able to establish the presence or absence of diffuse emission in this cluster. In Fig. 5.11 we show the radio contours of A56 superimposed to the XMM-Newton image. The X-ray image shows an irregular morphology and the presence of substructure in the cluster central region. The radio emission is composed by three main sources which are blended by the 2σ contours and permeates the cluster X-ray emitting region extending even beyond it.

A1443 has ~ 5 minutes VLA observation in array C (L band). The radio contours overlaid to the Chandra image are reported in Fig. 5.12 : the cluster appears elongated in the East-West direction, but no diffuse radio emission is detected. However this observation is not deep enough to classify this cluster as a no-RH cluster, EVLA (array C-D) and 330 MHz GMRT observations (analysis in progress) will clarify the nature of the radio emission in A1443.

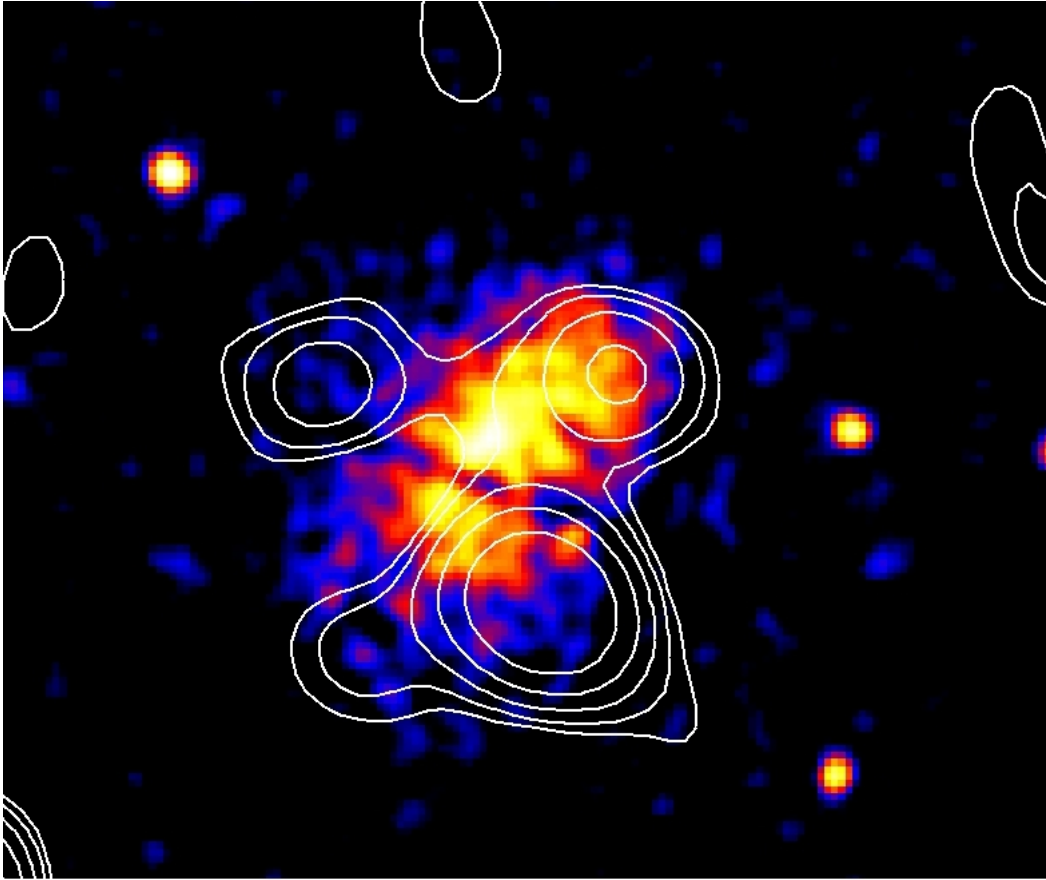


Figure 5.11: VLA-D 1400 MHz image of A56 (white contours) overlaid to the XMM-Newton image. Radio contours levels are $0.2 \times (2, 4, 8, 16, 32)$ mJy/beam.

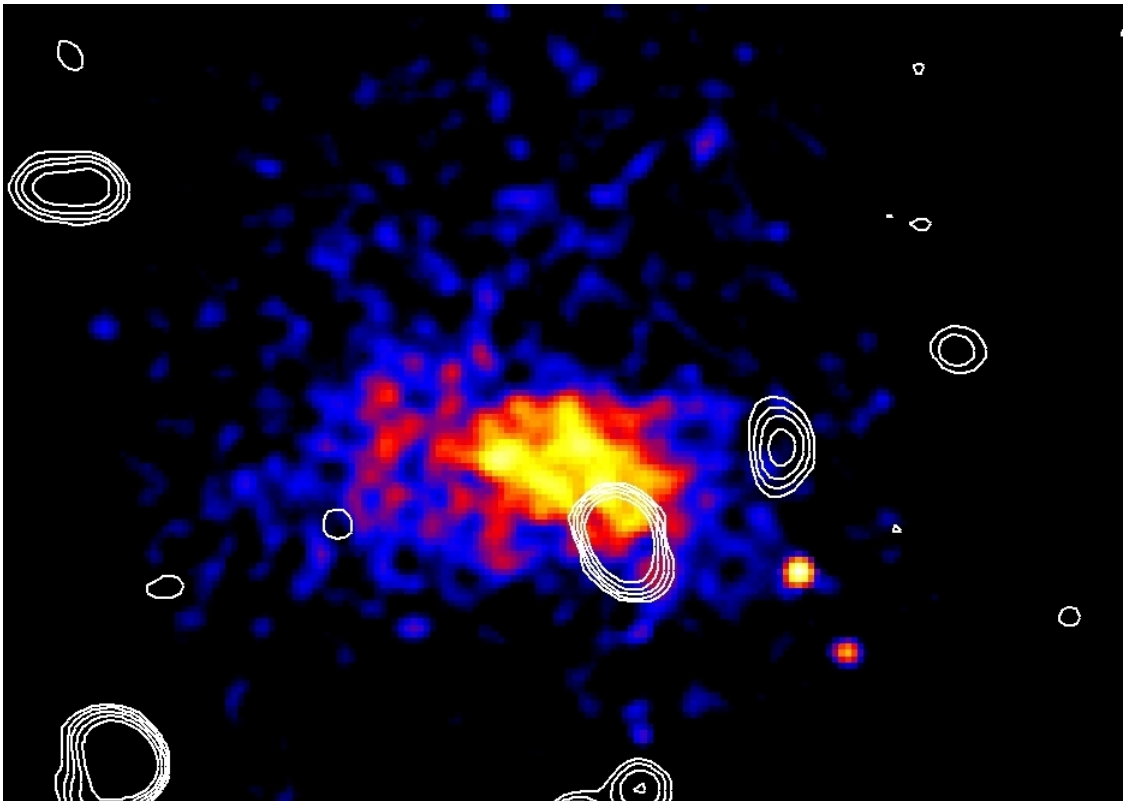


Figure 5.12: VLA-C 1400 MHz image of A1443 (white contours) overlaid to the Chandra X-ray image. Radio contours levels are $70 \times (2, 4, 8, 16, 32) \mu\text{Jy}/\text{beam}$, the 1σ level rms noise is $70 \mu\text{Jy}/\text{beam}$.

5.5 X-ray data analysis

Chandra X-ray data were reprocessed with CIAO 4.5 using calibration files from CALDB 4.5.8. Standard techniques to correct time-dependent problems were applied⁶, the screening of the events file was applied to filter out strong background flares, cosmic rays and soft protons. We adopted an automatic algorithm for the identification of point sources which were then removed from images. The image is then normalized for the exposure map of the observation, which is basically the combination of the effective area of the telescope with the map of the dwell time vs. pointing position and provides the effective exposure time as a function of the sky position exposed on the CCD.

Following Cassano et al. (2010), we made use of the Chandra images, derived in the 0.5-2 keV, to study the clusters dynamical status. For each cluster we analysed the surface brightness inside an aperture of 1 Mpc diameter, centred on the cluster X-ray peak and we derived the morphological parameters described in Sec. 4.2.4: the emission centroid shift, w , the concentration parameter, c , and the power ratio, P_3/P_0 . We report our clusters in the three morphological diagrams: $c-w$, $c-P_3/P_0$ and $w-P_3/P_0$.

In the low redshift sample there are four clusters, namely A478, A1413, A2142 and A2104, for which the 1 Mpc circle extends beyond the CCD edges. We report the example of A1413 in Fig. 5.13 (left panel). To test the reliability of the measure of the morphological parameters in these cases, we restrict our analysis to a smaller radius. We choose the largest possible radius not including the region outside the CCD (Fig. 5.13 right panel); on average we reduced the radius by a factor of $\sim 0.2 - 0.3$. We derived the morphological parameters inside the smaller region and we compared them with those calculated in the 1 Mpc circle. We also applied this test to A1689 that represents a case in which the 1 Mpc circle is well inside the CCD, thus it should not be affected by the selection of a smaller radius. We found that the power ratio parameter suffers the largest variations, this is because by construction it is more sensitive to disturbances at the aperture radius with respect to c and w (Buote & Tsai, 1995, 1996). Specifically, the power ratio parameter decreases of almost one order of magnitude in A478, A1413, A2142 and A2104, when measured in a smaller radius, while it slightly increases in the case of A1689. The other two parameters, c and w , are noticeably less affected by the reduction of the region in all the cases, however, given that a small reduction of the radius (a factor $\sim 0.2 - 0.3$) is required to avoid the region outside the CCD, we will consider for A478, A2104, A2142 and A1413 the reduced radius, to be less affected by observational effects. This is only needed in the case of the low redshift sample, since for high redshift clusters the 1 Mpc circle lies always well inside the CCD.

In some X-ray images the CCD gaps fall inside the aperture radius we selected

⁶<http://exc.harvard.edu/ciao/threads/index.html>

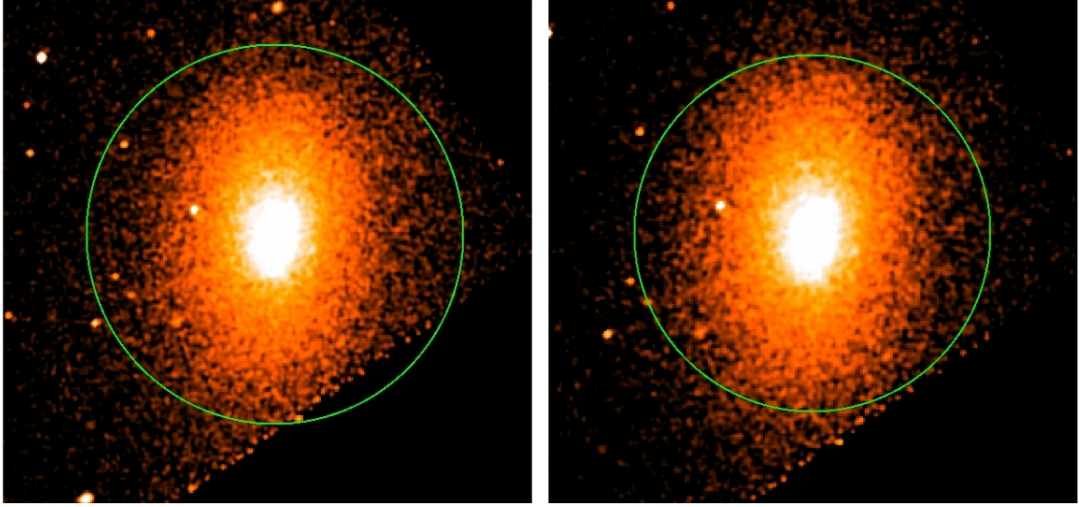


Figure 5.13: A1413 Chandra image with the circle of 1 Mpc diameter (left panel) extending beyond the CCD edges and the reduced circle (right panel) we selected for the morphological analysis.

for the morphological analysis. Even if the Chandra data reduction we performed re-fills the gaps by values interpolated from surrounding background regions (note for example the comparison of the two panels in Fig. 5.14) it is worth testing the reliability of our methods also in these cases.

For this purpose we selected three cases in which CCD gaps cross the cluster, i.e. A2204, A2218 and A115, and we derived the morphological parameters after excluding the CCD gap regions from our analysis.

We do not find significant variation for any of the morphological parameters, in particular, we do not find a common trend of increase or decrease in the three parameters moving from the case with included gaps to the case without gaps. On the basis of this result we performed the morphological analysis without masking the gap regions.

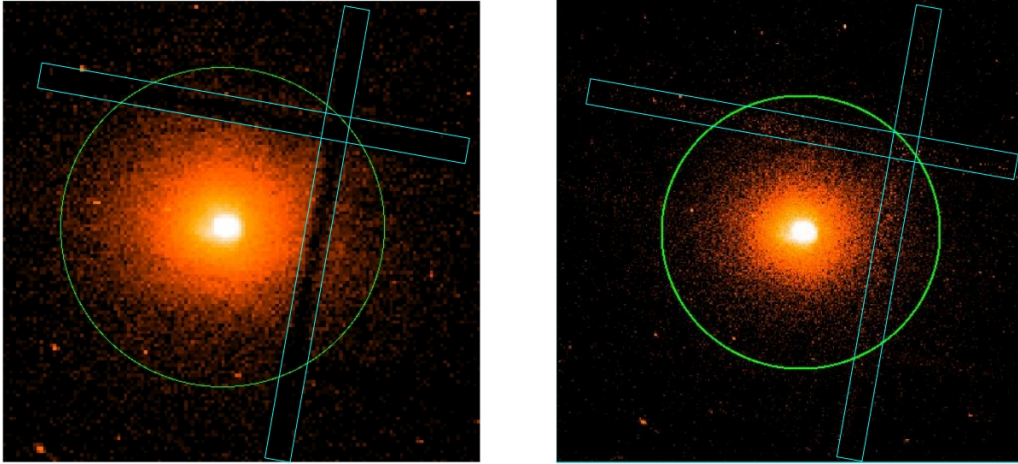


Figure 5.14: A2204 Chandra image downloaded from the archive (left panel) and produced with the Chandra data reduction (right panel). The green circle is the 1 Mpc region, while the cyan rectangles highlight the gaps between the CCDs. It is worth noticing that the gaps in the right panel are re-filled by interpolating the surrounding background regions.

5.6 The total sample

The total sample, made by the combination of the low redshift sample (21 clusters) and the high redshift sample (33 clusters), is thus composed of 54 clusters, whose properties are listed in Tab. 5.5. Since we included all the clusters extracted from the PSZ catalogue at $0.08 < z < 0.2$ (Fig. 5.1, red region), the low- z sample is complete in mass at $\sim 90\%$. The high- z sample instead is extracted from a region of the $M - z$ plane in which the PSZ catalogue completeness is $\sim 80\%$ (Fig. 5.1, cyan region), however we included in our analysis only clusters with adequate available radio information. We estimate that the completeness in mass of our total sample is $\sim 65\%$.

Among the 54 clusters, 44 (16 belonging to the low- z sample and 28 to the high- z one) have available Chandra data that we reduced with the technique explained in the previous Section, in order to derive information on the dynamical status of the clusters. Results will be presented on the following Chapter.

At the end of this Chapter we present a gallery of Chandra images in order of decreasing c , which can be seen as an order of increasing degree of disturbance. In the case of the low- z sample we overlay the NVSS map specifying whether the dataset have been reprocessed or not (see caption), for the high- z clusters instead we only show the X-ray image (since basically we took the radio information from the literature). The X-ray image is very useful because it allows to discriminate between mergers and relaxed clusters even by simple visual inspection, so this gallery might be a proper starting point for the quantitative analysis of the dynamical status

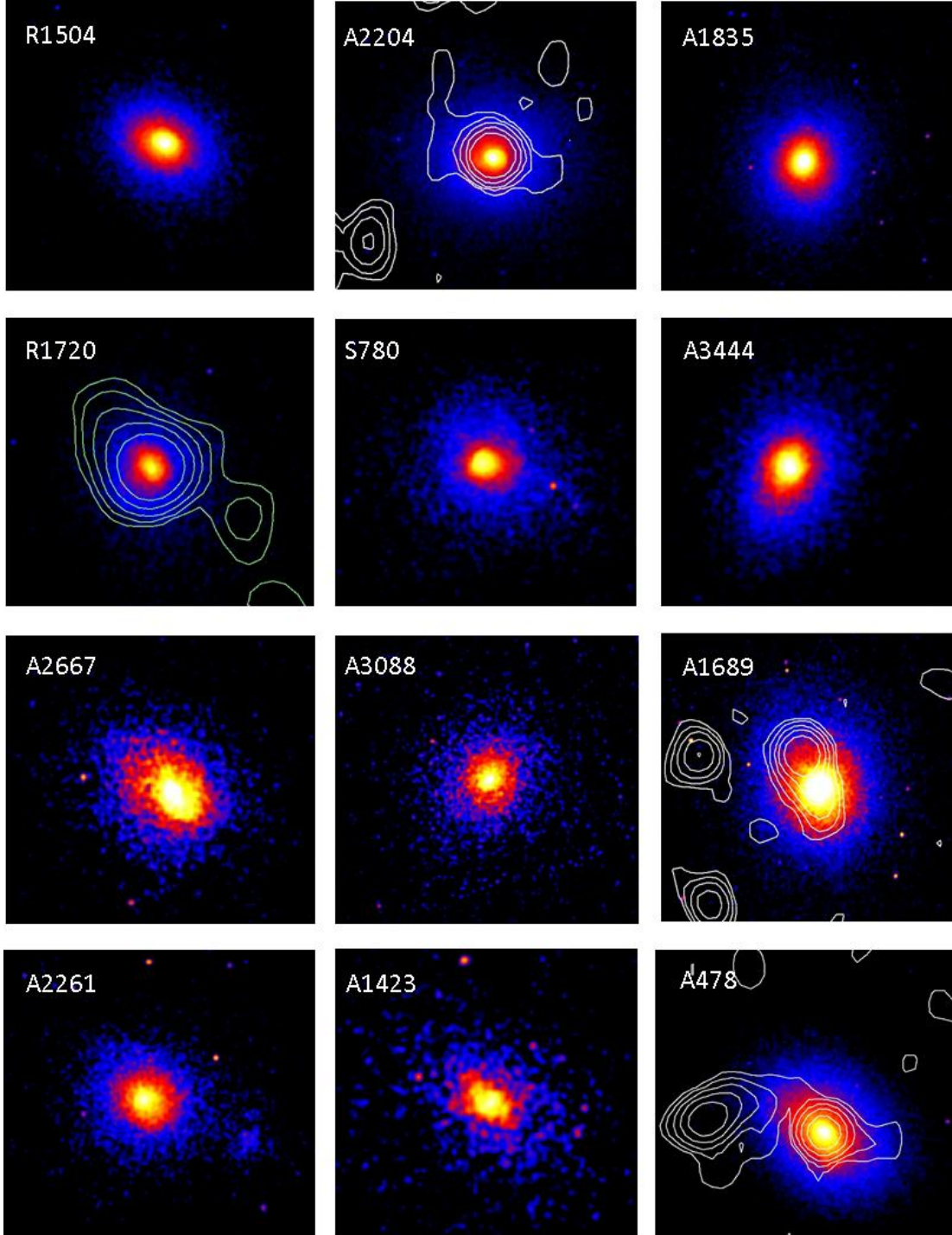
derived from the morphological parameters, whose results will be presented in the next Chapter.

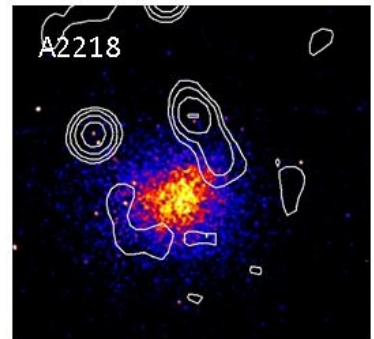
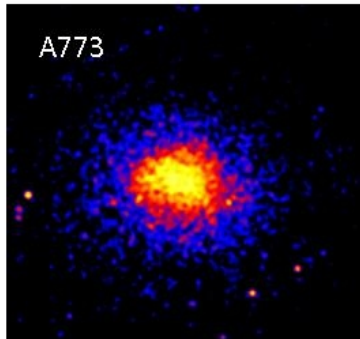
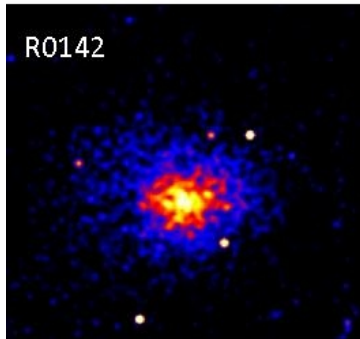
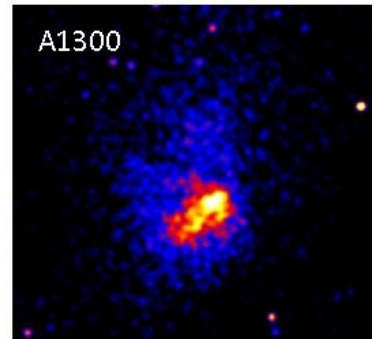
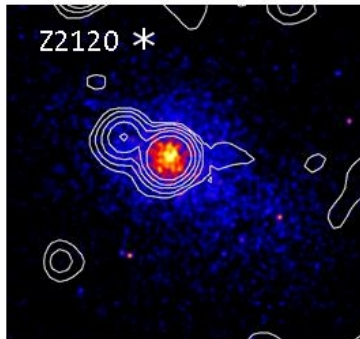
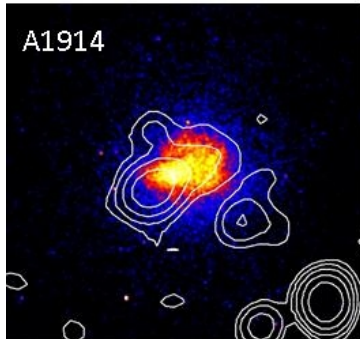
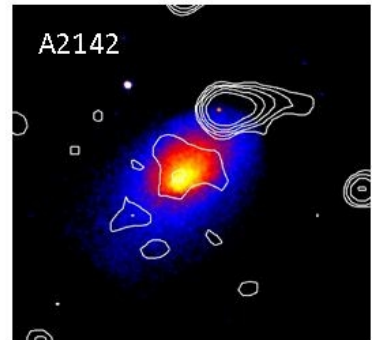
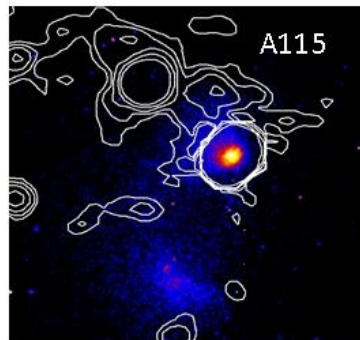
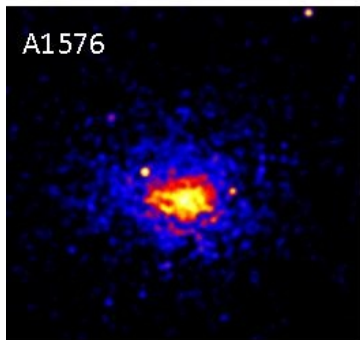
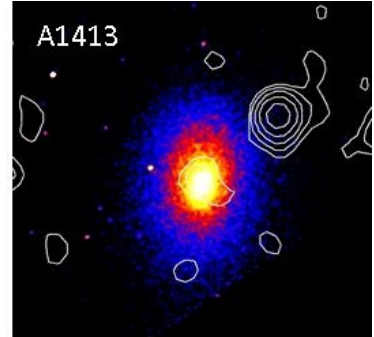
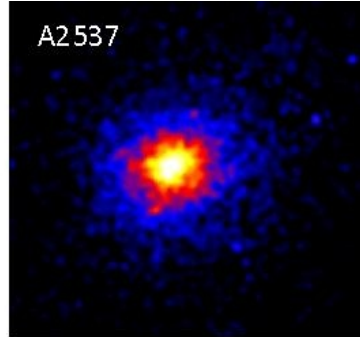
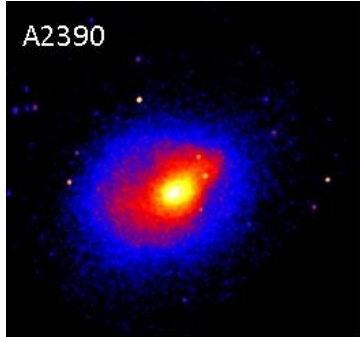
Table 5.5: Total sample clusters properties.

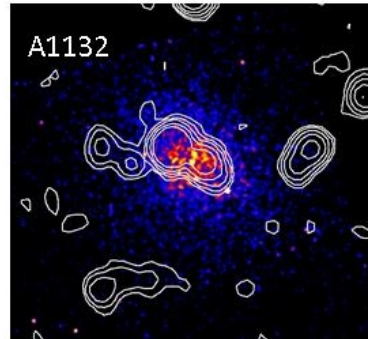
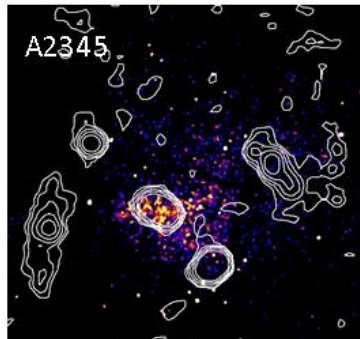
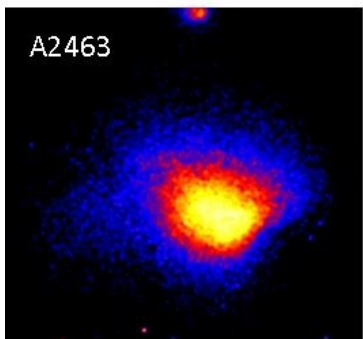
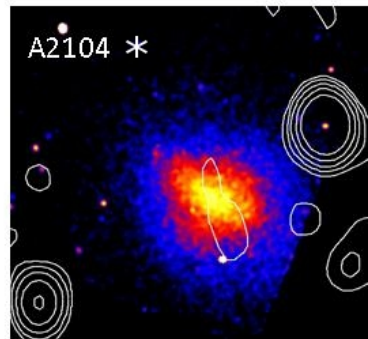
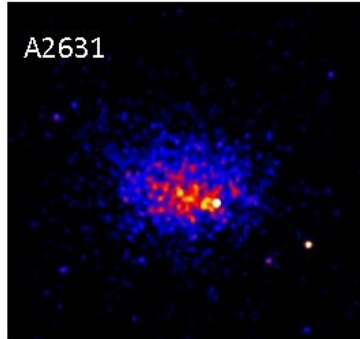
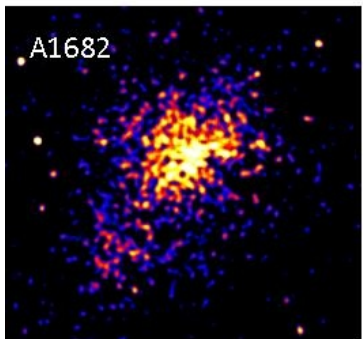
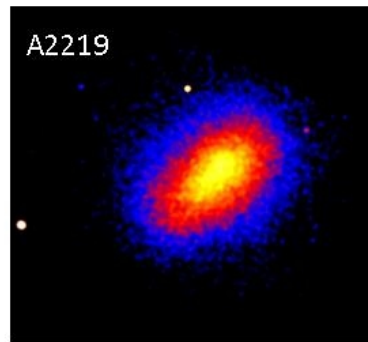
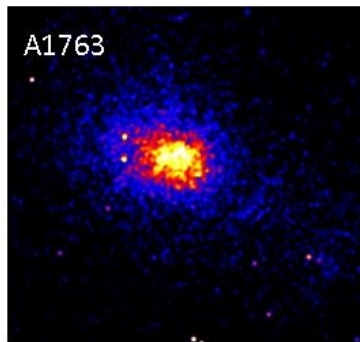
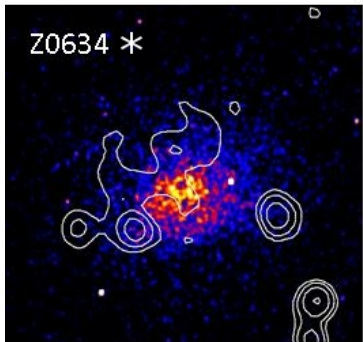
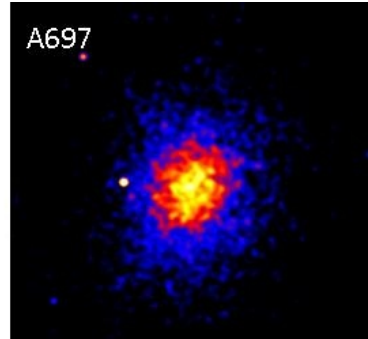
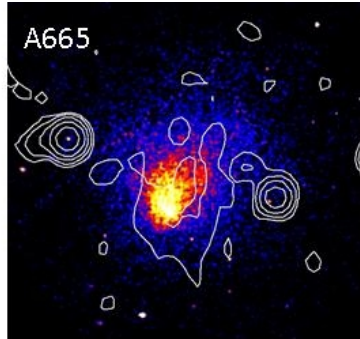
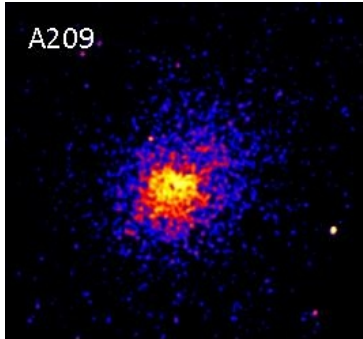
cluster name	RA	Dec	z	M_{500} ($10^{14} M_{\odot}$)	Radio info	X info
A1437	12 00 22.3	+03 20 33.9	0.134	5.69	no RH ✓	Rosat
A2345	21 27 06.8	-12 07 56.0	0.176	5.71	Relics	Chandra
A2104	15 40 08.2	-03 18 23.0	0.153	5.91	no RH ✓	Chandra
Zwcl 2120.1+2256	21 22 27.1	+23 11 50.3	0.143	5.91	suspect ✓	Chandra
RXC J0616.3-2156	06 16 22.8	-21 56 43.4	0.171	5.93	no RH ✓	RASS
A1413	11 55 18.9	+23 24 31.0	0.143	5.98	MH	Chandra
A1576	12 37 59.0	+63 11 26.0	0.302	5.98	UL	Chandra
A2697	00 03 11.8	-06 05 10.0	0.232	6.01	UL	XMM-Newton
Zwcl 0104.9+5350	01 07 54.0	+54 06 00.0	0.107	6.06	RH	Rosat
RXC J0142.0+2131	01 42 02.6	+21 31 19.0	0.280	6.07	UL	Chandra
A1423	11 57 22.5	+33 39 18.0	0.214	6.09	UL	Chandra
RXC J1314.4-2515	13 14 28.0	-25 15 41.0	0.244	6.15	RH	XMM-Newton
A2537	23 08 23.2	-02 11 31.0	0.297	6.17	UL	Chandra
A1682	13 06 49.7	+46 32 59.0	0.226	6.20	RH	Chandra
A1132	10 58 19.6	+56 46 56.0	0.134	6.23	no RH	Chandra
RXJ1720.1+2638	17 20 10.1	+26 37 29.5	0.164	6.34	no RH ✓	Chandra
A781	09 20 23.2	+30 26 15.0	0.295	6.36	UL	Chandra
A2218	16 35 51.6	+66 12 39.0	0.171	6.41	RH	Chandra
A3411	08 41 55.6	-17 29 35.7	0.169	6.48	RH	Chandra
Zwcl 0634.1+4750	06 38 02.5	+47 47 23.8	0.174	6.52	suspect ✓	Chandra
A3888	22 34 26.8	-37 44 19.1	0.151	6.67	suspect ✓	XMM-Newton
A3088	03 07 04.1	-28 40 14.0	0.254	6.71	UL	Chandra
A2667	23 51 40.7	-26 05 01.0	0.226	6.81	UL	Chandra
A521	04 54 09.1	-10 14 19.0	0.248	6.91	RH	Chandra
A2631	23 37 40.6	+00 16 36.0	0.278	6.97	UL	Chandra
A1914	14 26 03.0	+37 49 32.0	0.171	6.97	RH	Chandra
RXC J1504.1-0248	15 04 07.7	-02 48 18.0	0.215	6.98	MH	Chandra
A520	04 54 19.0	+02 56 49.0	0.203	7.06	RH	Chandra
A478	04 13 20.7	+10 28 35.0	0.088	7.06	MH	Chandra
A773	09 17 59.4	+51 42 23.0	0.217	7.08	RH	Chandra
A1351	11 42 30.8	+58 32 20.0	0.322	7.14	RH	Chandra
A115	00 55 59.5	+26 19 14.0	0.197	7.21	Relic	Chandra
A1451	12 03 16.2	-21 32 12.7	0.199	7.32	suspect ✓	XMM-Newton
PSZ1 G205.07-6294	2 46 27.5	-20 32 5.29	0.310	7.37	no RH	XMM-Newton
A2261	17 22 17.1	+32 08 02.0	0.224	7.39	UL	Chandra
RXCJ2003.5-2323	20 03 30.4	-23 23 05.0	0.317	7.48	RH	Chandra
A3444	10 23 50.8	-27 15 31.0	0.254	7.62	no RH, UL?	Chandra
S780	14 59 29.3	-18 11 13.0	0.236	7.71	UL	Chandra
A2204	16 32 45.7	+05 34 43.0	0.151	7.96	no RH	Chandra
A1758a	13 32 32.1	+50 30 37.0	0.280	7.99	RH	Chandra
A209	01 31 53.0	-13 36 34.0	0.206	8.17	RH	Chandra
A665	08 30 45.2	+65 52 55.0	0.182	8.23	RH	Chandra
A1763	13 35 17.2	+40 59 58.0	0.228	8.29	no RH	Chandra
RXC J1514.9-1523	15 14 58.0	-15 23 10.0	0.223	8.34	RH	RASS
A1835	14 01 02.3	+02 52 48.0	0.253	8.46	MH	Chandra
A2142	15 58 16.1	+27 13 29.0	0.089	8.81	RH	Chandra
A1689	13 11 29.5	-01 20 17.0	0.183	8.86	RH	Chandra

Table 5.5 – *Continue*

cluster name	RA	Dec	z	M_{500} ($10^{14} M_{\odot}$)	Radio info	X info
A1300	11 31 56.3	−19 55 37.0	0.308	8.83	RH	Chandra
A2390	21 53 34.6	+17 40 11.0	0.234	9.48	MH	Chandra
A2744	00 14 18.8	−30 23 00.0	0.307	9.56	RH	Chandra
A2219	16 40 21.1	+46 41 16.0	0.228	11.01	RH	Chandra
PSZ1 G171.96-40.64	11 27 50.4	−40 38 24.0	0.270	11.13	RH	RASS
A697	08 42 53.3	+36 20 12.0	0.282	11.48	RH	Chandra
A2163	16 15 46.9	−06 08 45.0	0.203	16.44	RH	Chandra







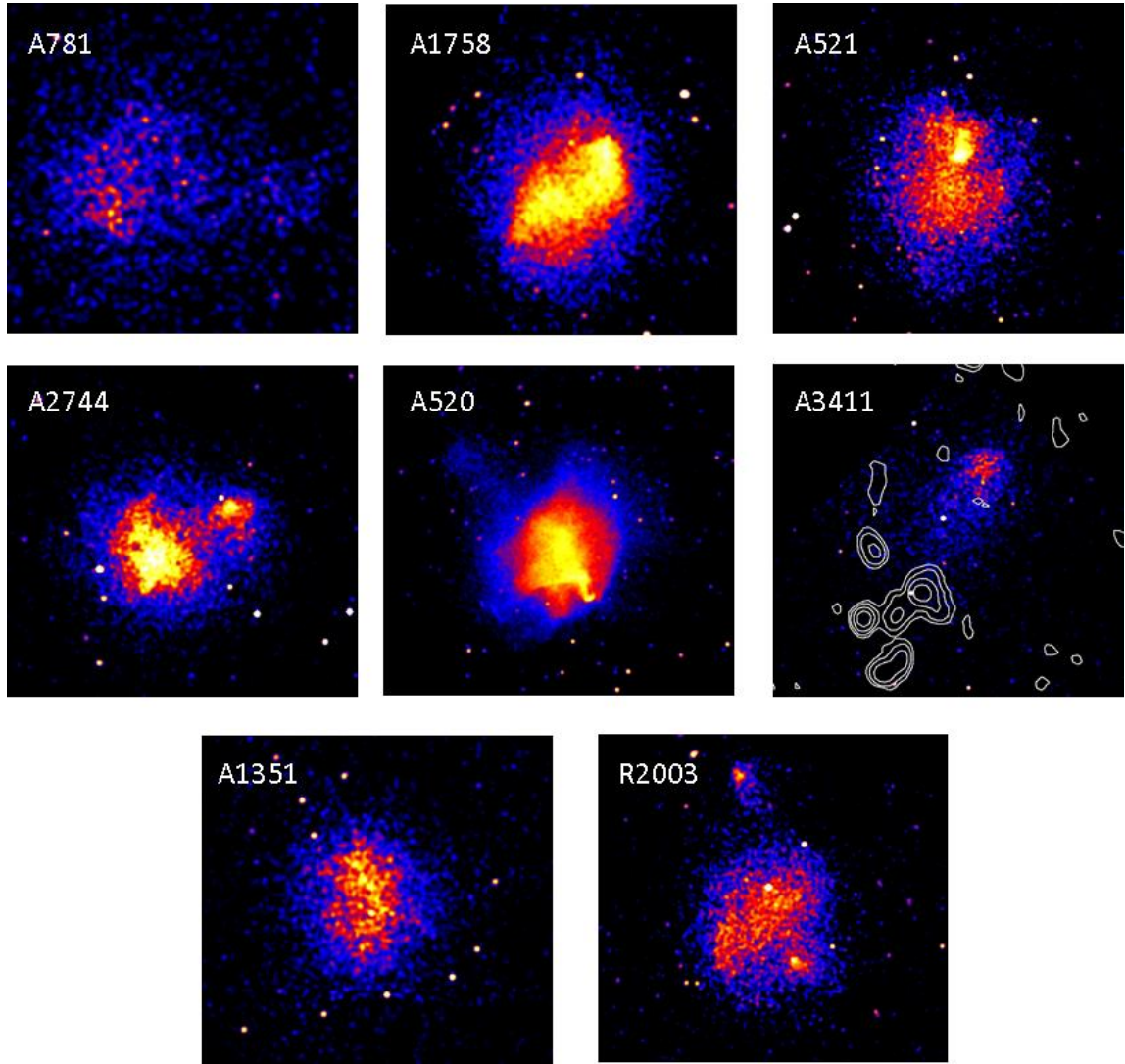


Figure 5.15: Chandra X-ray images of the clusters of the total sample in order of decreasing concentration parameter, c (from more relaxed to more dynamically disturbed clusters). Images with the NVSS radio contours overlaid belong to the low- z sample. (*) NVSS images reprocessed. Radio contours levels are $(2, 4, 8, 16, 32) \times \text{rms}$ [mJy/beam], where $\text{rms}=0.45$ mJy/beam for NVSS images, while for reprocessed images rms are listed in Tab. 5.4.

Chapter 6

Results & Discussion

In the previous Chapter we described the cluster sample used for our statistical investigation and also reported on the method of data analysis adopted to constrain the presence/absence of diffuse RH emission in the clusters. We also provided a brief description of the X-ray data analysis and of the methods adopted to derive morphological parameters.

In this Chapter we derive the fraction of clusters hosting RHs in our sample, as a function of the cluster mass and redshift. We investigate, via Monte Carlo methods, the presence of a firm drop of the RH occurrence towards the smallest systems of the sample. Finally, we derive the distribution of our clusters in the morphological diagrams, highlighting the role of merging in the RH formation.

6.1 Occurrence of Radio Halos

We first derive the fraction of clusters with RHs, f_{RH} , in the two separate subsamples, the low redshift and the high redshift one, and then that in the total sample. We started dividing our samples in two mass bins and we calculated the fraction of clusters with RHs in the low mass (LM) and high mass (HM) bin. As a starting point we split the sample in half according to the median value of the mass.

Among the 21 clusters of the low redshift sample, 7 host RHs, then we have 3 uncertain cases (Sec. 5.4.1). For the low- z sample we chose as the transition mass between the LM and the HM bin the median value of the mass, $M_{lim} = 6.5 \times 10^{14} M_{\odot}$. In the case of the high redshift sample, we found 16 clusters out of 33 that host a RH and the transition value between the two mass bins is $7.3 \times 10^{14} M_{\odot}$. In Tab. 6.1 we report the fraction of clusters with RHs (1σ Poissonian error) in the two redshift samples. To be conservative, for the low- z sample we report the values referred to the case in which we consider the suspect cases as clusters without diffuse radio emission (see table notes for the case in which we consider them as clusters with RH).

In both the redshift ranges we found only a marginal evidence for a jump in the

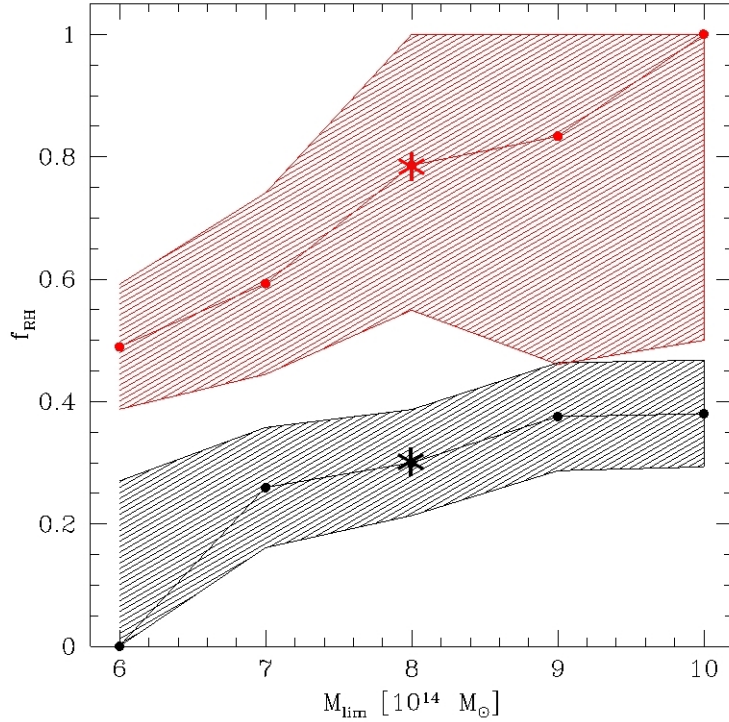


Figure 6.1: f_{RH} , with 1σ Poissonian errorbars, in the HM bin (red region) and in the LM bin (black region) as a function of the boundary mass, M_{lim} . The asterisks show the value of f_{RH} corresponding to $M_{lim} = 8 \times 10^{14} M_{\odot}$.

occurrence of RHs between the two mass bins, with f_{RH} increasing throughout the HM bin.

In order to test the statistical significance of this result, we consider the total sample of 54 clusters, in which we found 23 RHs. Again, we divided the sample according to the median value of the mass, which in this case is $M_{lim} = 7 \times 10^{14} M_{\odot}$ and we found that the fraction of clusters hosting RHs in the LM bin is $f_{RH} = 7/27 = 26 \pm 10\%$ and in the HM bin is $f_{RH} = 16/27 = 59 \pm 15\%$ ¹, thus confirming a drop of f_{RH} going from higher masses to lower masses.

The large number of clusters in the total sample allows to investigate the presence of a drop of f_{RH} in the low massive clusters and to test its significance. For this purpose, and also because there is “a priori” no reason to assume the median value of the mass as transition mass between the two bins, we calculated f_{RH} for different values of M_{lim} . Fig. 6.1 shows f_{RH} (with 1σ Poissonian errorbars) in the LM bin (black region) and in the HM bin (red region) for different values of the transition

¹These values are calculated considering the suspect cases as clusters without RH, if we consider them as RH clusters the fractions become: $f_{RH} = 9/27 = 33 \pm 11\%$ in the LM bin and $f_{RH} = 17/27 = 63 \pm 15\%$ in the HM.

Table 6.1: Occurrence of RHs in the low-z and high-z samples.

Low-z subsample			
	$N_{cluster}$	N_{RH}	f_{RH}
$M < 6.5 \times 10^{14} M_{\odot}$	10	2	$20 \pm 14\%^a$
$M > 6.5 \times 10^{14} M_{\odot}$	11	5	$46 \pm 20\%^b$
High-z subsample			
	$N_{cluster}$	N_{RH}	f_{RH}
$M < 7.3 \times 10^{14} M_{\odot}$	16	6	$38 \pm 15\%$
$M > 7.3 \times 10^{14} M_{\odot}$	17	10	$58 \pm 19\%$

Notes:

If we consider the suspect cases as clusters with RH we obtain

^a $2/10=20\pm 14\%$

^b $8/11=73\pm 26\%$

mass; shadowed regions connect the 1σ Poissonian errorbars.

To investigate which is the value of M_{lim} for which the drop of f_{RH} is most significant we perform Monte Carlo simulations as follow. We considered the suspect cases as cluster without diffuse radio emission. We randomly assigned 23 RHs among the 54 clusters of the sample and counted the number of RHs falling into the HM bin in our Monte Carlo trials. We performed the Monte Carlo analysis considering 5 different values of the transition mass between the two bins, specifically $M_{lim} = (6, 7, 8, 9, 10) \times 10^{14} M_{\odot}$. Fig. 6.2 shows the distributions of the number of RHs in the HM bin after 10^5 Monte Carlo trials in these five cases (see caption). We found that each distribution can be well fitted by a gaussian function, whose median vale (μ) and standard deviation (σ) are reported in Tab. 6.2, together with the observed number of RHs (N_{RH}), the fraction of clusters hosting RHs in the two mass bins (f_{RH}) and their ratio [$f_{RH}(HM)/f_{RH}(LM)$]. Given the observed number of RHs, we calculated Z that is the distance, in σ , between the gaussian median value and the observed value of N_{RH} :

$$Z = \frac{N_{RH} - \mu}{\sigma} \quad (6.1)$$

Considering, for example, the limiting mass $M_{lim} = 7 \times 10^{14} M_{\odot}$, which divides the sample in half, we obtained that the observed number of RHs in the HM bin is at 2.5σ from the value expected if RHs were distributed independently of the clusters masses. By means of the standard normal distribution tables we found that the probability to have by chance a number of RHs in the HM bin greater than 16 is 6.2×10^{-3} .

The transition mass that gives the most significant result (3.16σ) is $M_{lim} = 8 \times 10^{14} M_{\odot}$ and this is also the case in which we observe the greatest ratio between the values of f_{RH} derived in the two mass bins (Tab. 6.2).

Table 6.2:

Monte Carlo analysis

M_{lim} ($10^{14} M_{\odot}$)	N_{RH} (HM)	μ	σ	Z	probability	f_{RH} (HM)	f_{RH} (LM)	ratio
6	23	19.8	1.26	2.5	6.2×10^{-3}	$49 \pm 10\%$	$0 \pm 27\%^*$	–
7	16	11.38	1.83	2.5	6.2×10^{-3}	$59 \pm 15\%$	$26 \pm 10\%$	2.27
8	11	5.88	1.62	3.16	0.8×10^{-3}	$79 \pm 24\%$	$30 \pm 9\%$	2.63
9	5	2.5	1.26	1.98	2.4×10^{-2}	$83 \pm 37\%$	$38 \pm 9\%$	2.18
10	4	1.63	1.06	2.25	1.2×10^{-2}	$100 \pm 50\%$	$38 \pm 9\%$	2.63

Notes:

Although we are aware of the fact that the Poissonian statistics could not be really applied to our sample, we report f_{RH} with the 1σ Poissonian error, $\sigma_{f_{RH}}$, calculated as:

$\sigma_{f_{RH}} = \sqrt{N_{RH}}/N_{TOT}$, where N_{RH} and N_{TOT} are the number of clusters with RHs and the total number of clusters in the considered mass bin, respectively.

* In this case $N_{RH} = 0$, we report the modified Poissonian error derived as:

$$\sigma_{f_{RH}} = \frac{1 + \sqrt{N_{RH} + 0.75}}{N_{TOT}} \text{ (Gehrels, 1986)}$$

Monte Carlo calculations demonstrate the statistical significance of our result, suggesting that the increase of the occurrence of RHs with increasing the hosting cluster mass is physical, rather than casual.

In the framework of the turbulent re-acceleration scenario, theoretical models predict that electrons are accelerated by inefficient mechanisms. The efficiency of such mechanisms increases with the turbulent energy injected during mergers, which scales with the cluster thermal energy ($\sim M^{5/3}$). Therefore in this theoretical frame, RHs are expected to form preferentially in massive systems during energetic merger events. The observed increase of the fraction of clusters with RH between the LM and HM bins is in line with this theoretical picture: RHs originate in massive clusters which undergo merging events, energetic enough to accelerate particles efficiently.

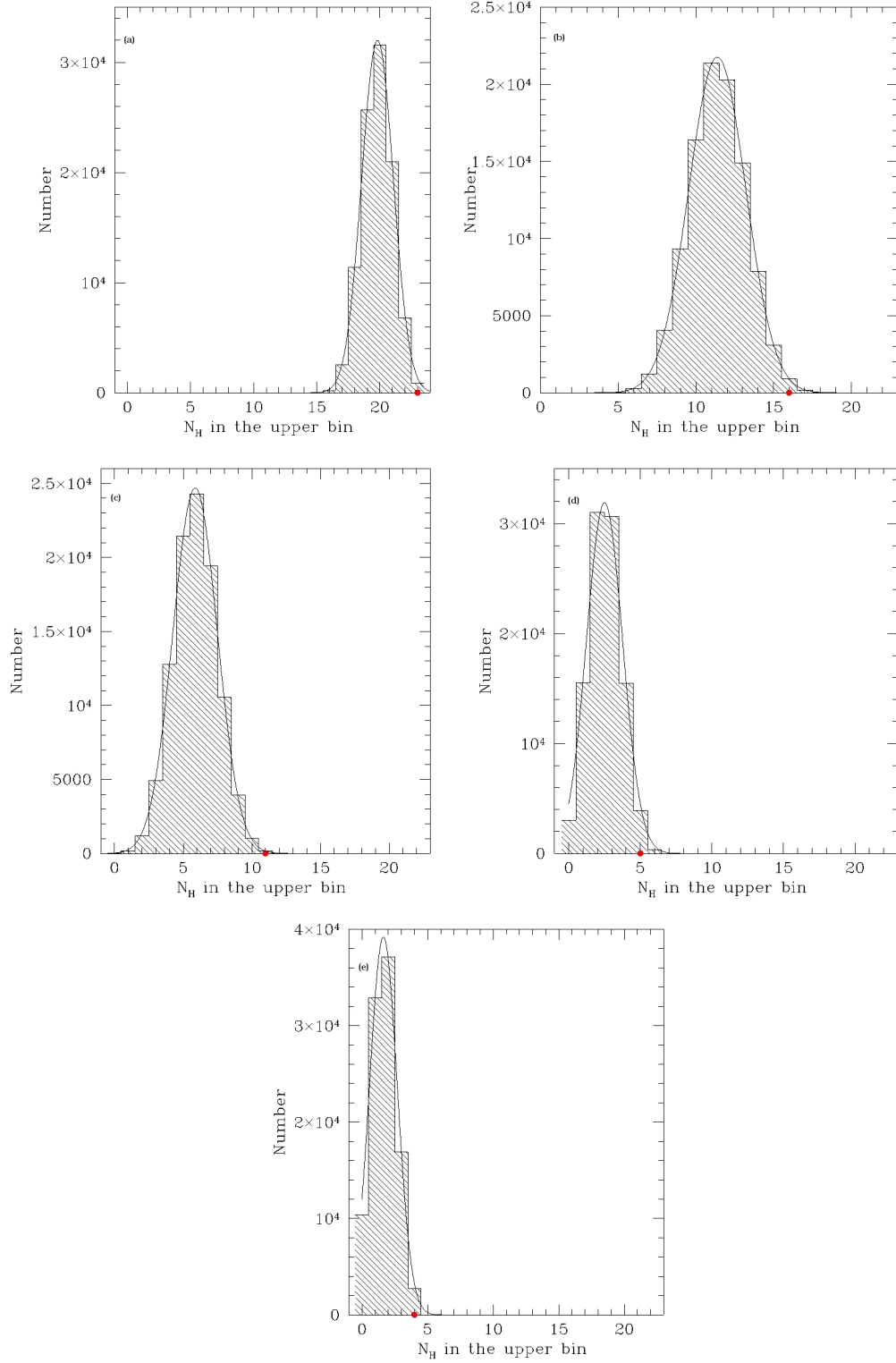


Figure 6.2: Monte Carlo calculations for: (a) $M_{\text{limit}} = 6 \times 10^{14} M_{\odot}$, (b) $M_{\text{limit}} = 7 \times 10^{14} M_{\odot}$, (c) $M_{\text{limit}} = 8 \times 10^{14} M_{\odot}$, (d) $M_{\text{limit}} = 9 \times 10^{14} M_{\odot}$, (e) $M_{\text{limit}} = 10 \times 10^{14} M_{\odot}$.

6.2 Radio Halo-merger connection

The X-ray data reduction we performed for those clusters with available Chandra archival data was aimed at getting information about the dynamical status of the clusters. Following Cassano et al. (2010) (see Sec. 4.2.4) we built up the three morphological diagrams ($c - w$, $w - P_3/P_0$, $c - P_3/P_0$) for the low- z and high- z subsamples and for the total sample. Again, the discussion will be focused on the total sample, since it allows to obtain the most statistically significant results.

In Fig. 6.3 we report the morphological diagrams for the 16 clusters of the low- z sample with available Chandra data. Vertical and horizontal dashed lines are taken from Cassano et al. (2010), in their cases they represented the median value of each parameter, this is not our case, but we will mark these lines on our plots just to visualize the segregation between merging and relaxed clusters, in comparison with previous published results. In spite of the poor statistic of this sample, there is a clear anti-correlation between the concentration parameter and both the centroid shift and power ratio parameters, while w and P_3/P_0 are well correlated. This reflects the fact that high values of c mean that the cluster is relaxed, while high values of w and P_3/P_0 stand for dynamically disturbed clusters. Most importantly even with just 16 clusters, we can see that RH (red dots) can be separated from clusters without RH (black dots). The only RH cluster that always falls in the relaxed region is A1689, however it is known that it is undergoing a merger event at a very small angle with the line of sight (Andersson & Madejski, 2004), therefore the derived morphological parameters for this cluster are likely biased due to projection effects. We note also that clusters with relics (blue dots) are located in the dynamically disturbed regions, in line with which is expected (see Sec. 2.4.3). It is worth noticing that there are few clusters without RH in the regions of merging clusters. Their position in these regions of the diagrams can be explained in the framework of the turbulent re-acceleration model. This model predicts a cut-off in the emission frequency of RHs, ν_c , that makes their detection difficult at $\nu_o > \nu_c$. The cut-off frequency is expected to be lower in less massive clusters. In line with this scenario, two of the merging clusters without RH have masses $< 6.5 \times 10^{14} M_\odot$. These clusters are expected to produce low frequency emitting RHs. Moreover, since the typical life-time of RHs is of the order of ~ 1 Gyr (Sec. 3.3), which is smaller than the total duration time of the merger (a few Gyr), it is possible that in these clusters the RH is not yet “on”, or it is already “off”.

Fig. 6.4 shows the distribution of the 28 clusters of the high redshift sample with available Chandra data in the three morphological diagrams. It is clearly visible that the segregation between merging and relaxed systems corresponds to the separation between RH and non RH clusters respectively. Again, we note that there are few clusters without RH in the merging region. They can be explained with the same argument used for the low- z sample, moreover, the turbulent re-acceleration model predicts that at higher redshift the cut-off frequency can be even lower due

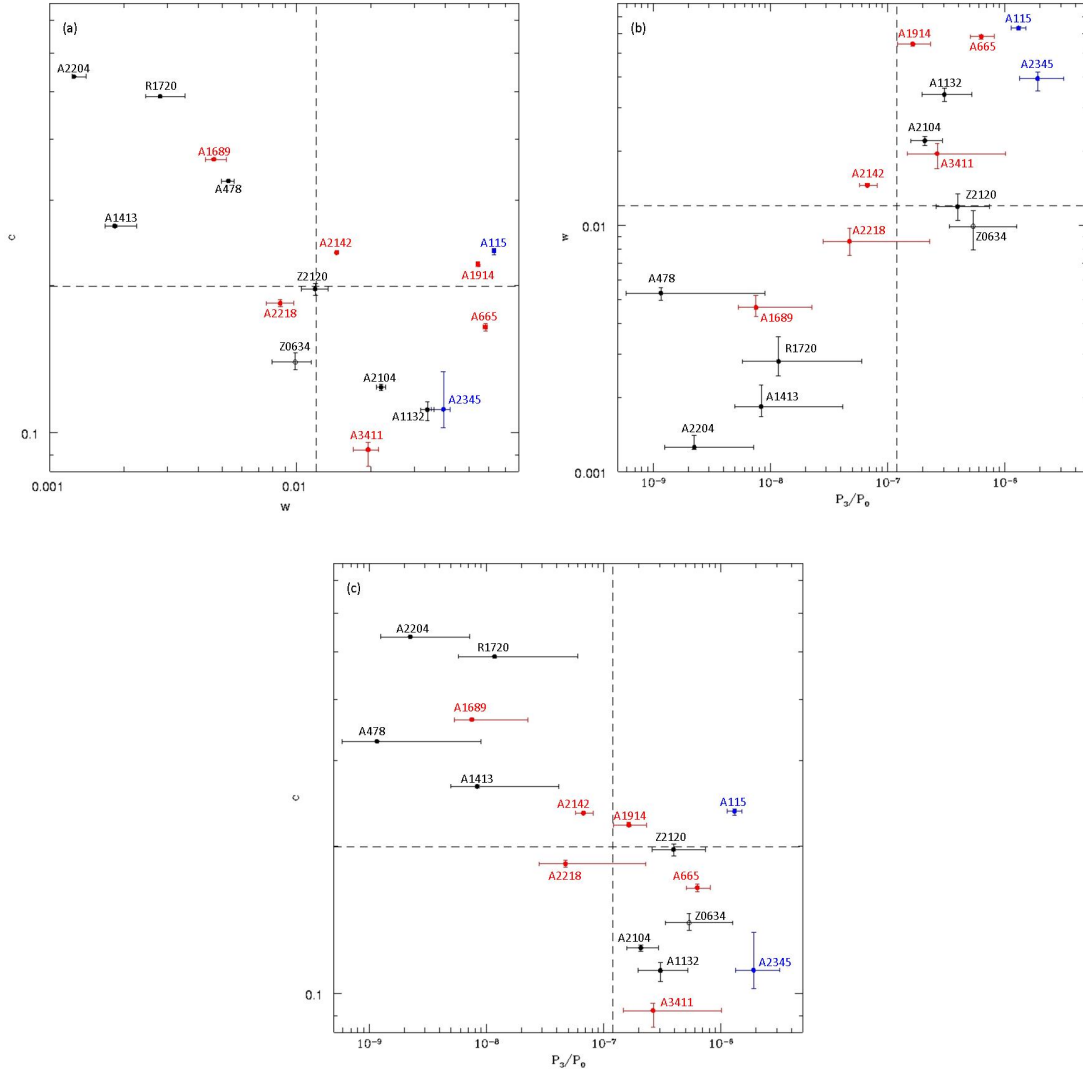


Figure 6.3: (a) $c - w$, (b) $w - P_3/P_0$, (c) $c - P_3/P_0$ for the 16 clusters of the low- z sample. Vertical and horizontal dashed lines: $c = 0.2$, $w = 0.012$ and $P_3/P_0 = 1.2 \times 10^{-7}$. Red, black and blue dots represent clusters with RH, clusters without RH and clusters hosting relics, respectively. Zwcl 0634.1+4750 (black open dot) is the only suspect case with available Chandra data.

to the higher IC losses of relativistic electrons, thus making even more difficult the detection of RHs at observational frequency >600 MHz.

Finally, we present in Fig. 6.5 the morphological diagrams for the total sample, they obviously come from the combination of Fig. 6.3 and 6.4, therefore, to avoid confusion, we do not rewrite the clusters names.

All diagrams provide strong evidence that the separation between RH and “ra-

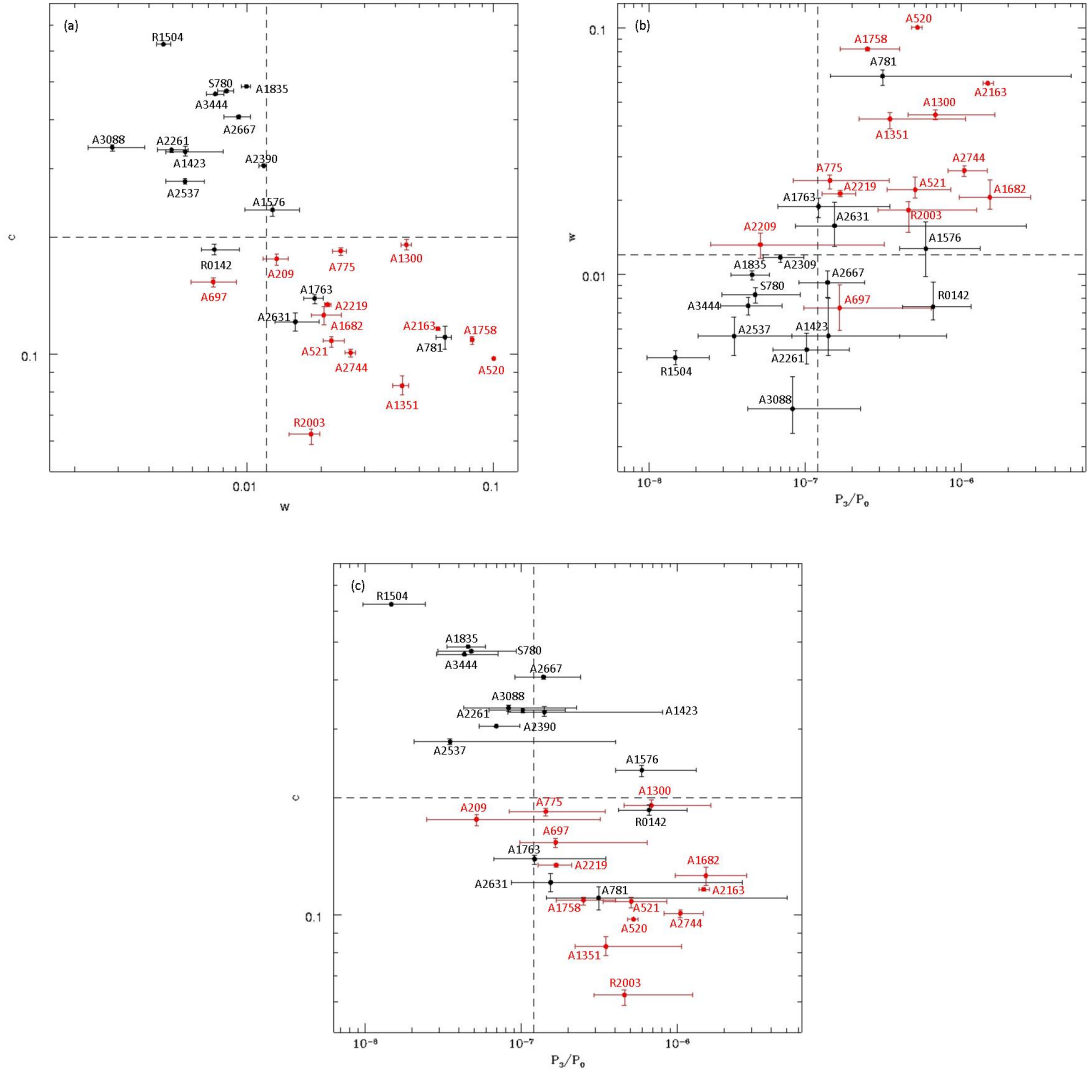


Figure 6.4: (a) $c - w$, (b) $w - P_3/P_0$, (c) $c - P_3/P_0$ for the 28 clusters of the high- z sample. Vertical and horizontal dashed lines: $c = 0.2$, $w = 0.012$ and $P_3/P_0 = 1.2 \times 10^{-7}$. Red and black dots represent clusters with RH and clusters without RH, respectively.

“quiet” clusters corresponds to a difference in the dynamical status: RHs form in dynamically disturbed clusters, while the greatest majority of clusters without Mpc-scale diffuse radio emission are more relaxed objects. This result demonstrates, from a statistical point of view, the connection between RHs and cluster mergers. Thanks to the larger statistics of the total sample, we can further investigate the role of merging in the formation of RHs by dividing the sample in two mass bins, according to the mass that provides the most significant drop in the fraction of clusters with RH (Tab. 6.2): $M_{lim} = 8 \times 10^{14} M_{\odot}$. We plot in Fig. 6.6 the $c - w$

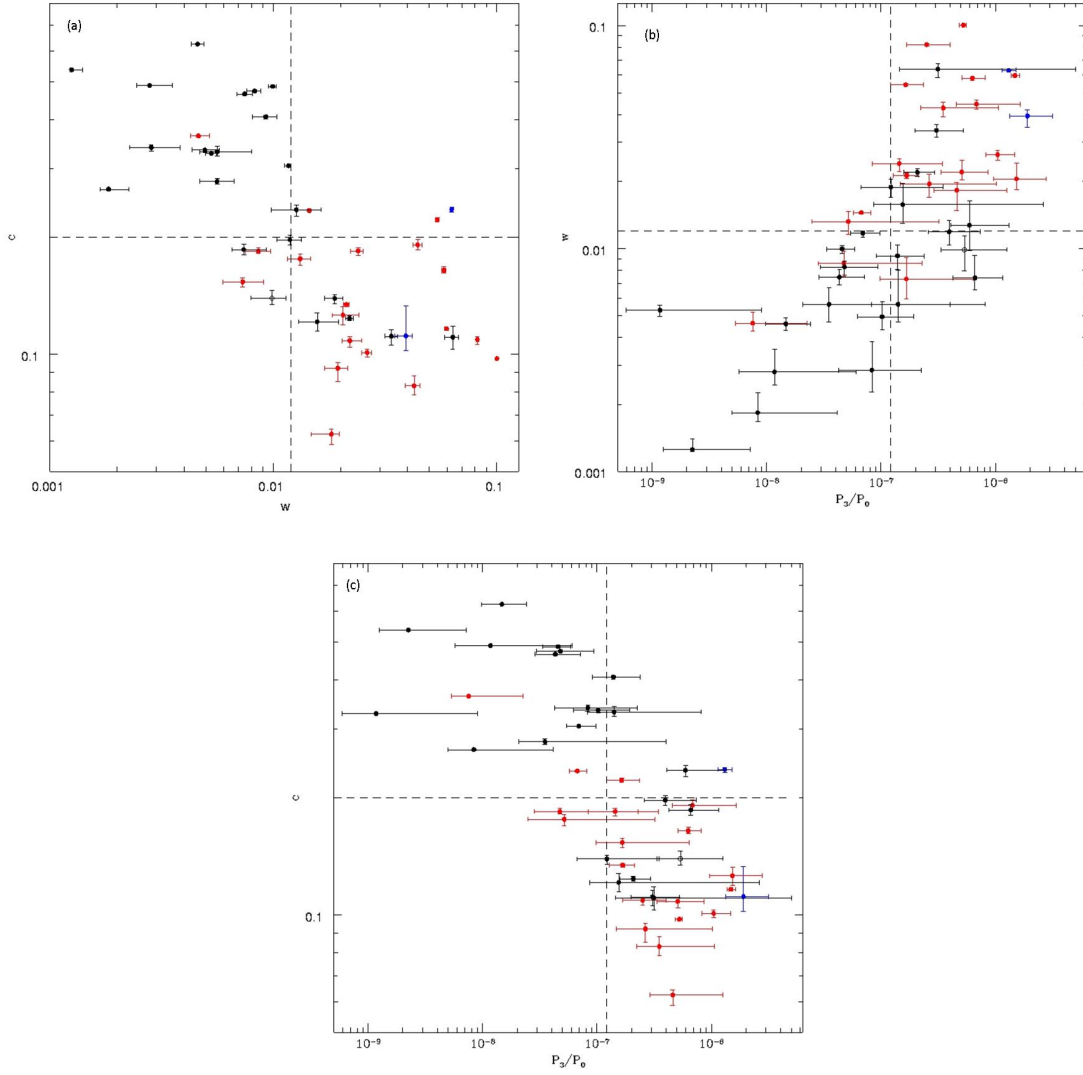


Figure 6.5: (a) $c - w$, (b) $w - P_3/P_0$, (c) $c - P_3/P_0$ for the total sample. Vertical and horizontal dashed lines: $c = 0.2$, $w = 0.012$ and $P_3/P_0 = 1.2 \times 10^{-7}$. Red, black and blue dots represent clusters with RH, clusters without RH and clusters hosting relics, respectively. Zwcl 0634.1+4750 (black open dot) is the only suspect case with available Chandra data.

diagram in the two mass bins; we chose c because it is the parameter that provides the best separation between RH and no RH clusters and w , that has smaller errors with respect to the power ratio parameter. Fig. 6.6 shows that the majority of high mass clusters are merging systems hosting RHs (lower panel), while in the LM bin we find both merging and relaxed objects, with RH always hosted by merging clusters (upper panel). The lack of massive relaxed objects has been already pointed

out by Cassano et al. (2013). They suggested that this can be due to the fact that the redshift range of their sample (0.2-0.35), roughly coincides with the formation epoch of these massive objects. Our sample covers a different redshift range (0.08-0.33), but we note that only 3 (A1689, A665 and A2142) out of 9 clusters in Fig. 6.6 (b) belong to the low- z sample, furthermore two of them have $z > 0.18$.

Another important information we derive from Fig. 6.6, is that the fraction of merging clusters without RHs is negligible for $M > 8 \times 10^{14} M_{\odot}$ (only one cluster without RH is present in the lower right corner), while it increases in the low mass range. This can be explained in the framework of the turbulent re-acceleration scenario, with the same arguments provided before.

It is important to remind that the morphological analysis was carried out for 44 clusters out of 54 of the total sample, because 10 clusters (5 belonging to the low- z sample and 5 belonging to the high- z one) missed Chandra archival data. Tab. 6.3 summarize the X-ray available data for these clusters. Most of the cluster in Tab. 6.3

Table 6.3: Clusters with no available Chandra data

cluster name	X-ray info
Low-z sample	
A1437	ROSAT
RXC J0616.3-2156	RASS
Zwcl 0104.9+5350	ROSAT
A3888	XMM-Newton
A1451	XMM-Newton
High-z sample	
A2697	XMM-Newton
RXC J1314.4-2515	XMM-Newton
PSZ1 G205.07-62.94	XMM-Newton
RXCJ 1514.9-1523	RASS
PSZ1 G171.96-40.64	RASS

have scheduled Chandra observations, we plan to add them to our morphological analysis in the future.

5 out of 10 clusters have XMM-Newton observations that we use to infer qualitatively the morphology of the clusters (Fig. 6.7). From ROSAT pointed observations and RASS images we can't reliably derive information about the morphology of the clusters.

A3888 and A1451 are two of those objects for which we found an hint of diffuse radio emission that however can't be classified as RH on the basis of the analysis we carried out with the NVSS data. Quantitative information about the dynamical status of these clusters would be very interesting, indeed their XMM-Newton images (Fig. 6.7 upper panels) show some signs of merger activity (elliptical mor-

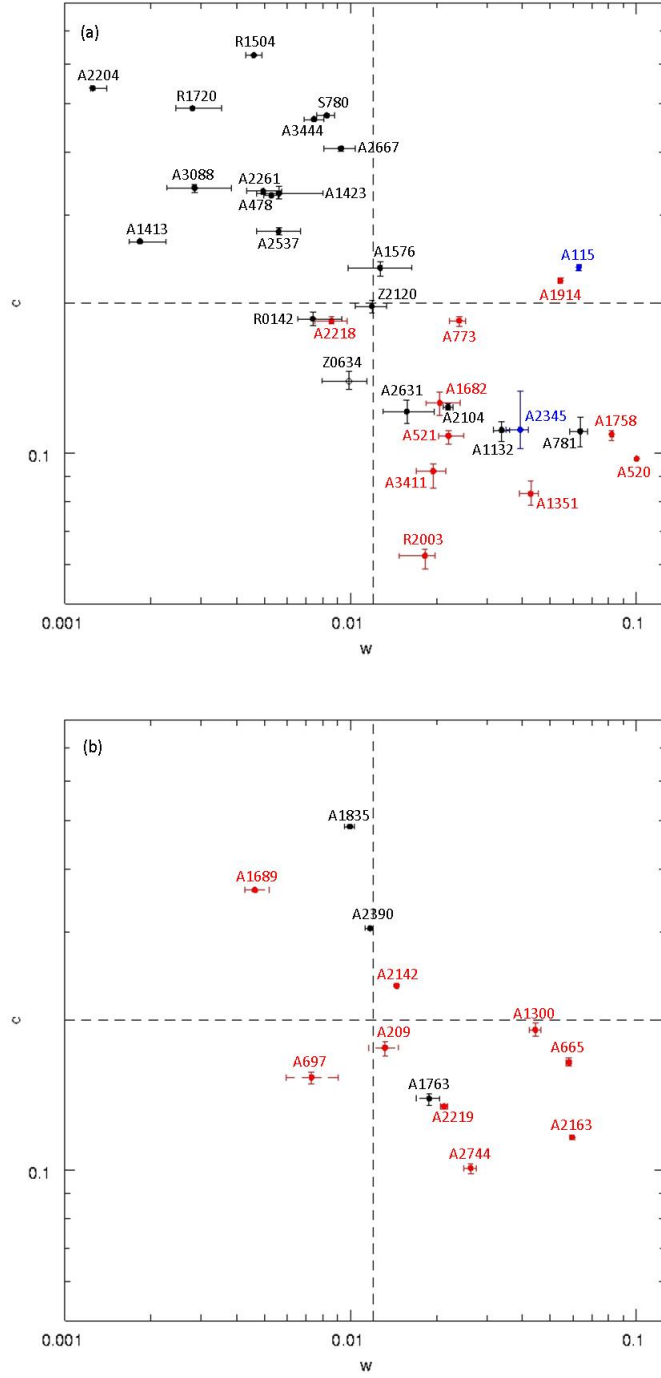


Figure 6.6: (a) $c-w$ diagram for clusters in the LM bin ($M < 8 \times 10^{14} M_{\odot}$), (b) $c-w$ diagram for clusters in the HM bin ($M > 8 \times 10^{14} M_{\odot}$). Symbols are the same as Fig. 6.5.

phology, core substructures). The dynamically perturbed status of A1451 has been also highlighted by Valtchanov et al. (2002) by means of optical and X-ray data analysis.

The other three clusters belong to the EGRHS. Among these, A2697 (Fig. 6.7 median left panel) is a cluster without diffuse radio emission and its XMM-newton image reveal a quite circular shape with a bright core, suggesting that it is a relaxed cluster.

RXCJ 1314.4-2515 is a RH cluster of the EGRHS, its X-ray image (Fig. 6.7 median right panel) shows a very irregular morphology with two central peaks and it is a well known merging cluster (Mazzotta et al. 2001; Valtchanov et al. 2002).

Finally, the XMM-Newton image of PSZ1 G205.07-62.94 (Fig. 6.7 lower panel) show an elongated shape suggesting the presence of dynamical activity, however no RH has been detected in this cluster (Ferrari et al., private communication).

All the clusters in Tab. 6.3 require further investigation, however, from a qualitative point of view, we can infer that the inclusion of these clusters in the morphological analysis should not affect our statistical result.

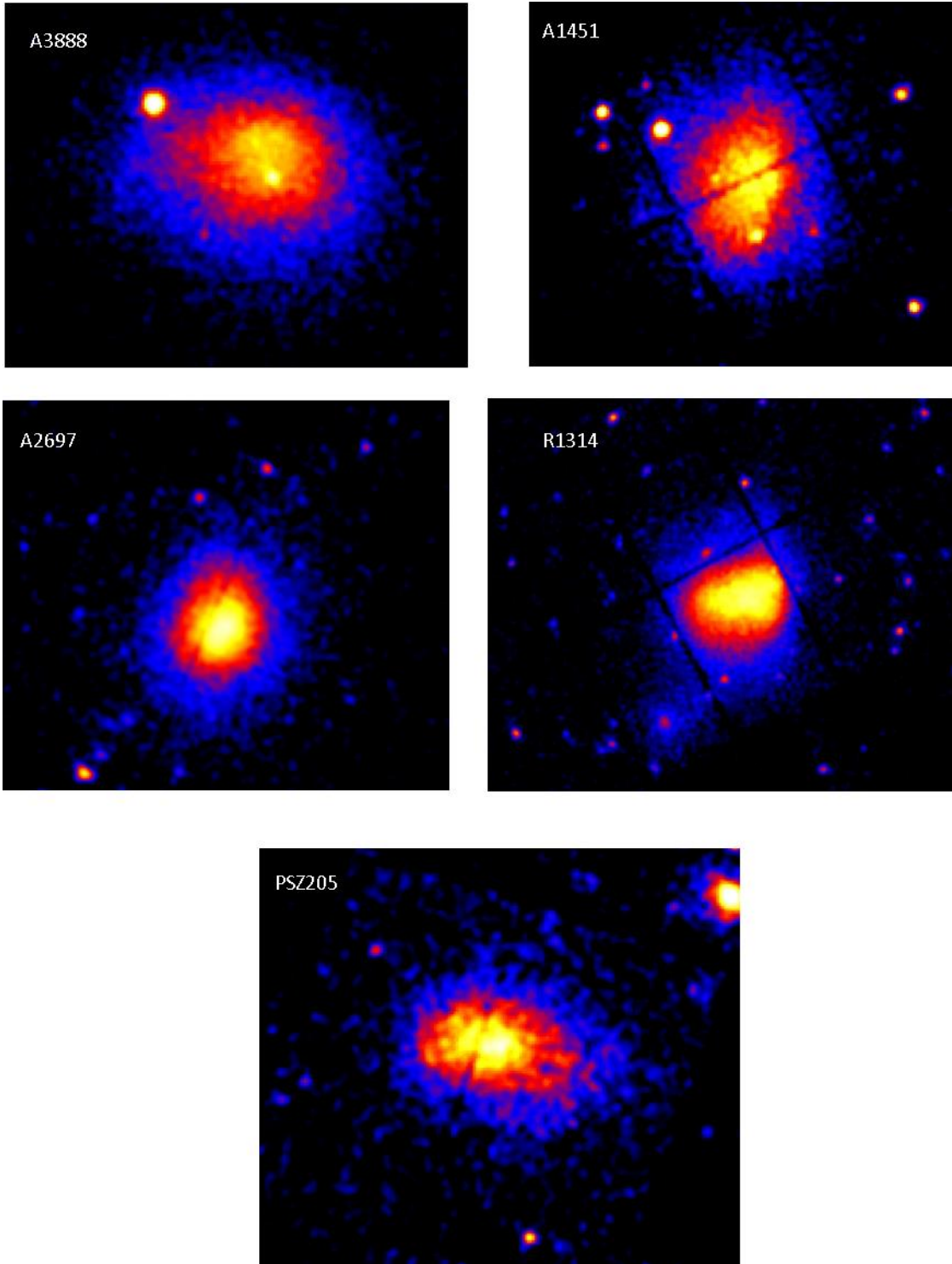


Figure 6.7: A3888 (upper left panel), A1451 (upper right panel), A2697 (median left panel), RXCJ 1514.9-1523 (median right panel) and PSZ1 G171.96-40.64 (lower panel) XMM-Newton images.

Chapter 7

Comparison with model expectations

In this final Chapter we compare the statistical measurements of the occurrence of RHs, as a function of the cluster mass, with theoretical expectations we derive assuming the turbulent re-acceleration scenario and following the statistical modelling discussed in Chapter 3.

7.1 Basic ingredients of the statistical model

In the framework of the turbulent re-acceleration model, the formation and evolution of RHs is strictly connected to the merging history of the hosting cluster. In particular, at a given redshift, the fraction of clusters with RHs depends on the cluster merger rate and on the fraction of energy injected by the merger in the form of turbulence. In this Section, we summarize the main ingredients necessary to derive the probability to form RHs in the framework of this model:

- (i) *Cluster formation.* The formation and evolution of galaxy clusters is computed following the extended Press-Schechter (1974) theory of structure formation, developed by Lacey & Cole (1993). Given the present-day cluster mass, M_0 , the merging history of the cluster can be followed back in time using Monte Carlo simulations. Since a cluster of mass M_0 can be the result of different merging histories, a great number, N , of trees for each M_0 is necessary for a full statistical description of the cosmological evolution of the cluster mass.
- (ii) *Turbulence in galaxy clusters.* The turbulence in galaxy clusters is supposed to be injected during merger events and then dissipated on time-scales of the order of the cluster crossing time. The energetics of the turbulence injected in the ICM is estimated from the PdV work done by the infalling subcluster in

passing through the volume of the most massive one. A fraction of this turbulence is then injected into magneto-sonic (MS) waves which in turn accelerate relativistic electrons.

- (iii) *Acceleration efficiency.* For each merger tree, the electron acceleration coefficient, $\chi(z)$, as a function of redshift can be obtained by combining all the merger events that contribute to the injection of turbulence at a given redshift.

7.2 How to derive f_{RH} from Monte Carlo calculations

In the framework of this model the synchrotron spectrum of RH is expected to become significantly steeper above a frequency $\nu_s \sim 7\nu_b$ (see Cassano et al. 2010), with ν_b being the synchrotron break frequency (see Sec. 3.4):

$$\nu_b \propto \langle B \rangle \gamma_b^2 \propto \frac{\langle B \rangle \chi^2}{(\langle B \rangle^2 + B_{CMB}^2)^2} \quad (7.1)$$

where χ is the electron acceleration coefficient that depends on the cluster merging history and it is given by (see Sec. 3.3 for details):

$$\chi(z) \propto \frac{\eta_t}{R_H^3} \sum_j \left[\left(\frac{M_V + \Delta M}{R_V} \right)^{3/2} \frac{r_s^2}{\sqrt{k_b T}} \right]_j \times \begin{cases} 1 & \text{if } r_s \leq R_H \\ (R_H/r_s)^2 & \text{if } r_s \geq R_H \end{cases} \quad (7.2)$$

As already discussed in Sec. 3.4, a RH is detectable only when its frequency ν_s is higher than the observing frequency, ν_o . Given that the break frequency depends on the electron acceleration coefficient, χ , the condition for having a detectable RH ($\nu_s \geq \nu_o$) becomes a condition on the acceleration coefficient: $\chi \geq \chi_{min}(\nu_o)$.

Given a cluster with mass M_0 , the fraction of time the cluster spends with $\chi \geq \chi_{min}(\nu_o)$ when its mass and redshift are within a given ΔM and Δz , is given by:

$$f_{M_0}^{\Delta M, \Delta z} = \frac{\sum_{j=1}^N t_u^j}{\sum_{j=1}^N (t_u^j + t_d^j)} \quad (7.3)$$

where t_u is the time that the cluster spends with $\chi \geq \chi_{min}$, in the redshift range Δz and mass bin ΔM , and t_d is the time that the same cluster spends with $\chi < \chi_{min}$ (see Fig. 7.1 for a schematic example).

The total probability to form a RH in the bin ΔM (and Δz) is obtained by combining all the contributions given by the different N clusters with mass M_0 (Eq. 7.3), weighted with the present-day cluster mass function. The latter step is necessary to account for the fact that the number density of clusters is larger for smaller systems, that thus have a large statistical weight in the derivation of f_{RH} .

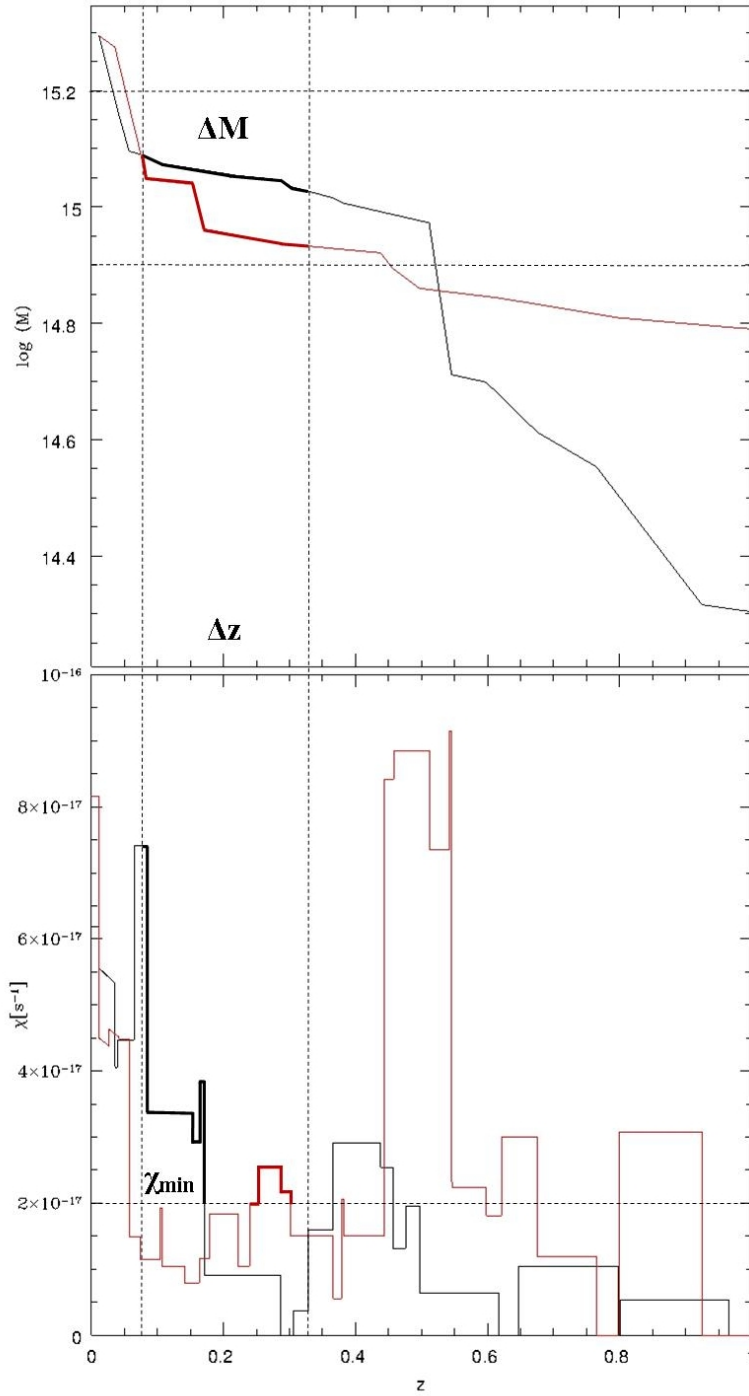


Figure 7.1: Top panel: example of two merger trees (black and red lines) of clusters with $M_0 = 2 \times 10^{15} M_\odot$; lower panel: evolution of the electron acceleration coefficient, $\chi(z)$, associated with the two merger trees reported above. For a given ΔM (and Δz) selected on the merger trees (bold face lines in the upper panel), we selected the fraction of time each cluster spends with $\chi \geq \chi_{min}$ (bold face lines in the lower panel). Here we report, just for example, a value of $\chi_{min} = 2 \times 10^{-17} \text{ s}^{-1}$.

7.3 Adopted parameters and procedures

To derive the expectations for the RH fraction, we need first to define the values of the parameters entering in the calculations. Specifically we followed previous works (CB05, CBS06, Cassano et al. 2008, Cassano et al. 2013) and adopted:

- the fraction of turbulence injected in MS waves, $\eta_t=0.2$
- the scaling between the magnetic field and the cluster mass defined in Sec. 3.4.1:
 $B = B_{\langle M \rangle} \left(\frac{M}{\langle M \rangle} \right)^b$, with $\langle B \rangle = 1.9 \mu\text{G}$, $\langle M \rangle = 1.6 \times 10^{15} M_\odot$ and $b = 1.5$.

In order to have a prompt comparison with our observations, we calculated the formation probability of RHs for clusters with present mass $M_0 > 1.2 \times 10^{15} M_\odot$ ¹, in three redshift ranges: $\Delta z = 0.08 - 0.2$, corresponding to the low-z sample, $\Delta z = 0.2 - 0.33$ corresponding to the high-z sample and $\Delta z = 0.08 - 0.33$, for the total sample. We adopted $\nu_s \geq \nu_o = 600$ MHz, to account for both GMRT and NVSS observations. This implies a threshold value $\chi \geq \chi_{min}(600 \text{ MHz})$ of the electron acceleration coefficient, which defines the condition for the RH formation. From the masses M_0 used in CB05, we selected those values $M_0 \geq 1.2 \times 10^{15} M_\odot$, thus we considered 7 values of M_0 in the range $(1.3 - 5.8) \times 10^{15} M_\odot$. For each M_0 , we used $N = 60$ simulated merger trees. We then derived the RH statistics in the following available mass bins ΔM :

- **BIN C**: $[0.82 - 1.6] \times 10^{15} M_\odot$
- **BIN D**: $[1.0 - 2.0] \times 10^{15} M_\odot$
- **BIN A**: $[1.3 - 2.6] \times 10^{15} M_\odot$
- **BIN E**: $[1.6 - 3.5] \times 10^{15} M_\odot$
- **BIN H**: $[2.0 - 4.5] \times 10^{15} M_\odot$

By construction these mass bins overlap in order to increase the statistics and to minimize sampling errors. Here we summarize the principal steps of the numerical codes we used to derive the formation probability of RHs:

- (i) For each M_0 , we considered ~ 60 merger trees and the corresponding 60 files containing the value of $\chi(z)$.
- (ii) For a given mass bin $\Delta M = M_u - M_l$, we determined which masses M_0 are relevant for that mass bin, considering that:
 - obviously, M_0 cannot be smaller than the minimum mass, M_l , of the bin, otherwise its merger tree would never cross the mass bin ΔM ;

¹Note that M_0 is the virial mass, that corresponds to roughly $2 \times M_{500}$, therefore $M_0 > 1.2 \times 10^{15} M_\odot$, means $M_{500}(z=0) > 6 \times 10^{14} M_\odot$.

- M_0 cannot be substantially greater than the maximum mass of the bin, M_u , because its merger trees would cross the mass bin, ΔM , only at very high redshift, higher than that considered in the present work.
- (iii) Fixed ΔM and the masses, M_0 , relevant to that bin, for each merger tree, we derived the fraction of time the cluster spends with $\chi \geq \chi_{min}$ (Eq. 7.3).
- (iv) Finally, the probability to form a RH with $\nu_s \geq 600$ MHz in a cluster with a redshift value within Δz and mass in the bin ΔM , was obtained by combining the contributions from clusters with the different M_0 relevant to that mass bin ΔM , weighted by the PS cluster mass function at $z = 0$.

Once this procedure has been applied to the five mass bins, the values of the formation probability were averaged where the bins overlap, thus providing the probability to form RHs with $\nu_s \geq 600$ MHz as a function of the cluster mass, in the three redshift ranges taken into consideration.

7.4 Results & Discussion

The goal of this Section is to test whether the observed drop of the fraction of clusters with RHs towards the smaller systems is consistent with the expectations of the turbulent re-acceleration scenario. For this purpose, we derived, with the procedure described in previous Sections, the expected fraction of RHs as a function of the cluster mass in the redshift ranges corresponding to our samples (Fig. 7.2, red lines). In Fig. 7.2 the observed fraction of clusters with RHs in the two mass bins (blue dashed region for the HM bin, black dashed region for the LM bin) are overlaid to the model prediction of the probability to form RHs (red line). The height of the shadowed regions represents the 1σ Poissonian error (See Chapter 6). Actually, due to the poor statistics, in the low- z sample and in the high- z one (Fig. 7.2, upper left and right panel respectively), we are not able to constrain the presence of a drop of f_{RH} between the two mass bins. On the other hand, considering the total sample (Fig. 7.2, lower panel), where we found a significant (3.2σ) drop of f_{RH} from the HM to the LM bin, we note a good agreement, at 1σ , between model expectations and observations.

It is worth noticing that the cosmological model adopted to describe the merging rate of galaxy clusters is based on the PS formalism, which underestimates the merging rate, and hence the number density, of massive objects. The use of more sophisticated semi-analytical methods (including, for example, the ellipsoidal collapse; e.g. Sheth & Tormen 1999) to describe the merging rate of collapsed objects, or cosmological simulations of cluster formation, might potentially improve the statistical modelling for the formation of RHs. Qualitatively, we expect that the probability to form RHs should be slightly revised up in the high-mass end, thus providing an even better matching with the observations.

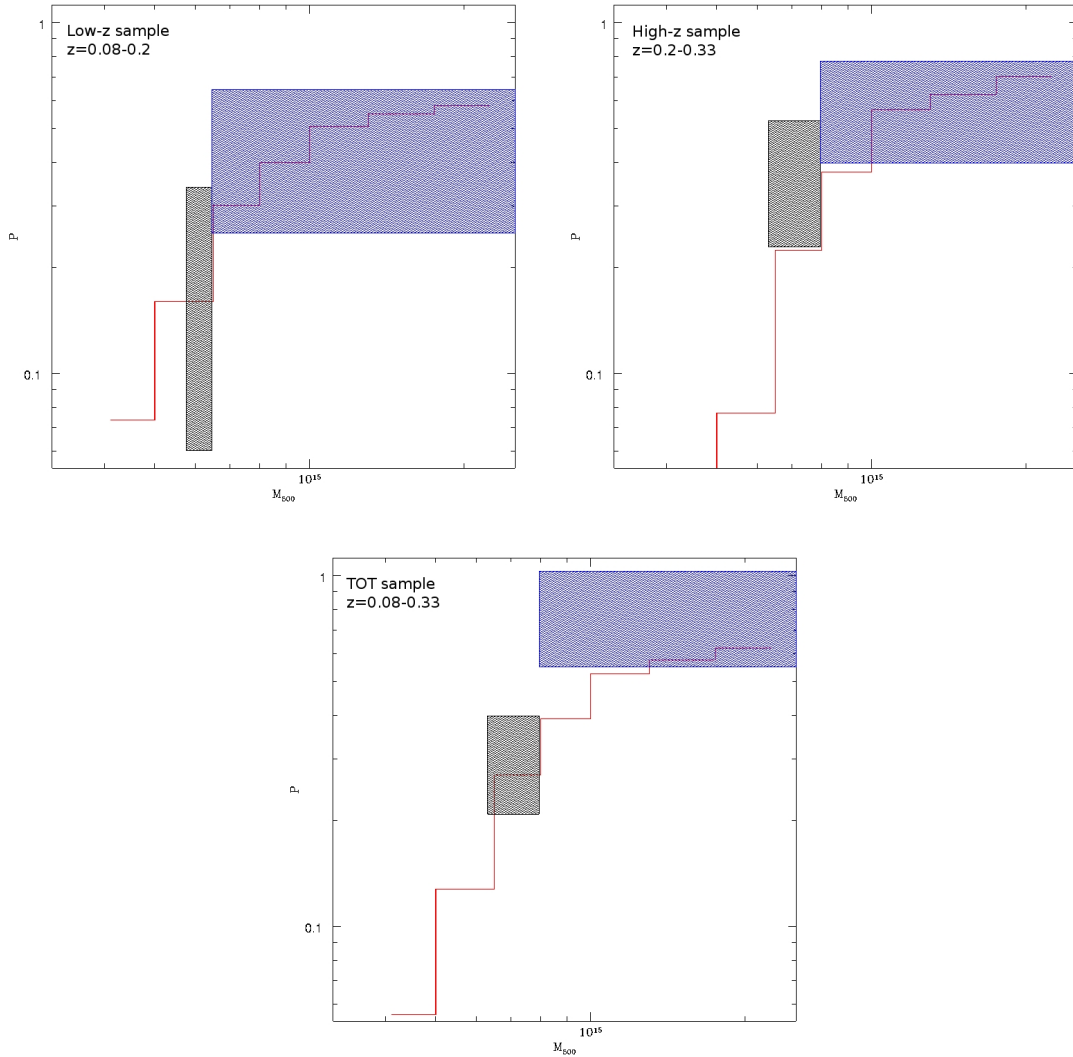


Figure 7.2: The red line represents the formation probability of RHs with $\nu_s \geq 600$ MHz in clusters with present mass $M_0 > 1.2 \times 10^{15} M_\odot$ in three redshift ranges: $z = 0.08 - 0.2$ (upper left panel), $z = 0.2 - 0.33$ (upper right panel) and $z = 0.08 - 0.3$ (lower panel). The shadowed regions mark the observed fraction of RHs in the LM (black) and HM (blue) bins (1σ errors) of the three samples.

We also remind that the statistical calculations are derived considering RHs of fixed size ($R_H = 500$ kpc) while the observed RHs spread a range of radii. Furthermore, in our observational analysis we consider both “classical” RHs and USSRHs. However, some of the observed USSRHs can have $\nu_s \leq 600$ MHz and hence could be not represented in the performed model calculations.

In spite of the need of further investigation to improve the theoretical model, including a more appropriate description of the cluster formation history and the presence of RHs with different sizes, we can reasonably affirm that the observed drop of the occurrence of RHs in the smaller systems can be understood in the framework of the turbulent re-acceleration scenario, where only massive clusters are expected to develop enough turbulence to generate RHs emitting at $\nu \geq 600$ MHz.

Summary & Conclusions

The study of the statistical properties of RHs in galaxy clusters has become increasingly important in the last decade because of its diagnostic power in testing the theoretical models for their origin and in unveiling the connection between RHs and cluster formation.

Among the models proposed for the origin of RHs, the turbulent re-acceleration scenario, in which the turbulence injected in the ICM during cluster mergers re-accelerates relativistic particles, is favoured by present observations (Brunetti et al. 2001, Petrosian et al. 2001). This model provides a “natural” explanation of the connection between RH and cluster mergers (see Brunetti & Jones, 2014 for a review). The alternative view is that RHs are produced by secondary electrons injected in the ICM by hadronic collisions between CR protons and thermal protons (e.g. Dennison 1980). The latter model, known as secondary or hadronic model, is disfavoured by the non detection of galaxy clusters in γ -rays (The Fermi-LAT Collaboration, 2013) and by the existence of RHs with extremely steep spectra.

The turbulent re-acceleration scenario provides clear expectations about the statistical properties of RHs, namely their formation rate in the Universe and their link with the cluster evolution (mass, dynamics and redshift). In particular, the formation history of RHs depends on the cluster merging rate through cosmic epochs and on the mass of the hosting clusters themselves, which ultimately sets the energy budget available for the re-acceleration of relativistic particles. A key expectation is that RHs should be preferentially found in massive objects undergoing energetic merger events, whereas the fraction of clusters with RHs (f_{RH}) should drop towards smaller merging systems, obviously RHs should be absent in relaxed systems (e.g. Cassano & Brunetti, 2005). This is due to the fact that turbulence in massive clusters is expected to accelerate more efficiently relativistic particles, which in turn could be able to emit synchrotron radiation efficiently up to \geq GHz frequency. On the other hand, turbulence in less massive clusters should induce less efficient acceleration of particles, making electrons able to emit at lower frequencies. These less massive clusters and/or less energetic merger events are expected to produce RHs with extremely steep spectra, the so-called Ultra Steep Spectrum Radio Halos (USSRH), that will be mostly visible at low frequency. As a consequence, the fraction of cluster with RH is expected to increase at lower frequency, and the drop of this fraction, towards smaller systems, is expected to be less pronounced with

respect to that observed at ~ 1 GHz (Cassano et al. 2010).

These expectations have driven a large observational project carried out to perform a statistically solid exploration of the properties of RHs in the Universe, the GMRT RH Survey (GRHS, Venturi et al. 2007, 2008) and its extension (EGRHS, Kale et al. 2013). This was a deep pointed radio survey dedicated to the search of RHs in a sample of X-ray selected clusters in the redshift range $z = 0.2 - 0.35$. The sensitivity reached by these observations allowed, for the first time, to place firm upper limits (UL) to the diffuse radio flux density of clusters without RH and to show that clusters branch into two populations: RHs trace the $P_{1.4} - L_X$ correlation, whereas radio-undetected clusters (UL) lie about one order of magnitude below the correlation (Brunetti et al. 2007, 2009). In addition, this bimodal split can be traced to cluster dynamics, with RHs always associated to merging systems and clusters without RH being statistically more relaxed (Cassano et al. 2010).

The combination of the GRHS with previous published analysis of NVSS data for low redshift clusters (e.g. Giovannini et al. 1999) allowed, for the first time, to find a possible statistical evidence (at 3.7σ) that f_{RH} increases with the cluster X-ray luminosity, being of $\sim 40\%$ in the most luminous systems (Cassano et al. 2008). These results were found to be in agreement with expectations based on the turbulent re-acceleration scenario, assuming the cluster X-ray luminosity as a proxy of the mass. However, it is well known that the $L_X - M$ correlation has a large scatter (40 – 50%, e.g. Reiprich & Böhringer, 2002) and that biases in the mass determination from the X-ray luminosity might be introduced for cool-core and merging clusters.

The only possibility to overcome these problems is to have a more robust measure of the cluster mass. The recent advent of SZ-cluster surveys with the Planck satellite, has enabled the construction of cluster samples that are as near as possible to be mass-selected samples, thank to the tight correlation between the total SZ signal, Y_{500} , integrated within R_{500}^2 , and the cluster mass, M_{500} .

Recent studies, based on the EGRHS and the Planck SZ catalogue (PSZ, Planck Collaboration, 2013), show the presence of a bimodal split between clusters with RH and clusters without RH also in the radio power-cluster mass (or Y_{SZ}) diagrams, for clusters with $M_{500} > 5.5 \times 10^{14} M_{\odot}$ and $z = 0.2 - 0.35$ (Cassano et al. 2013) and also suggest that the fraction of clusters with RH could be very high in the most massive systems. The completeness in mass of the sample obtained combining the PSZ catalogue and the EGRHS is however $\sim 50\%$ at smaller masses, which did not allow to probe the presence of a drop of f_{RH} in clusters with $M < 8 \times 10^{14} M_{\odot}$. Later studies, based on the analysis of NVSS data and on the PSZ catalogue, claim that the occurrence of RH appears larger in SZ-selected cluster samples with respect to that derived from X-ray-selected samples (Sommer & Basu, 2014), but were unable to test the presence of a drop of f_{RH} towards smaller systems.

² R_{500} is the radius within which the average density is $500 \times \rho_{cr}$, where ρ_{cr} is the critical density of the Universe.

The goal of this Thesis is to overcome the limits of the previous studies and perform:

- 1) an unbiased census of RHs in a mass-selected sample of galaxy clusters;
- 2) a comparison of the observed occurrence of RHs with expectations derived from turbulent re-acceleration models.

For these purposes we selected clusters with $M \gtrsim 6 \times 10^{14} M_{\odot}$ in the redshift range $0.08 < z < 0.33$ from the Planck SZ catalogue, and we searched for the presence of RHs in the NVSS (plus literature information) for clusters at $z < 0.2$ and in the EGRHS for $z > 0.2$. The sample collects all the clusters from the PSZ catalogue with $0.08 < z < 0.2$ that have NVSS data and all the Planck clusters with $0.2 < z < 0.33$ that have EGRHS data. The resulting sample has a completeness in mass of $\sim 65\%$, larger than that available in previous studies (e.g. Cassano et al. 2013). We also used the available Chandra X-ray data, for 44 out of 54 clusters, to derive information on the cluster dynamical status.

In Chapter 5 we described the data analysis performed during the Thesis work. To determine the presence/absence of RHs in clusters without literature information, we analysed NVSS data for 21 low- z clusters, while we analysed VLA pointed datasets for two clusters at higher z . Six low redshift clusters showed an hint of diffuse radio emission in the NVSS images, in these cases, we reprocessed the NVSS datasets, aiming at producing better images, with rms noise ~ 2 times below the nominal NVSS rms noise. Three of these clusters still showed some residual emission at their centres, thus we considered these as suspect cases. Our analysis led to a total sample of 54 clusters with radio information, 23 of which host RHs. In this Chapter we also reported on the Chandra X-ray analysis of data performed to derive the morphological parameters (the centroid shift, w , the power ratio, P_3/P_0 , and the concentration parameter, c), which are powerful diagnostics of the cluster dynamical status.

In Chapter 6 we described our main observational results. We split our sample into two mass bins, the low mass bin (LM, $M < M_{lim}$) and the high mass bin (HM, $M > M_{lim}$) and derived the fraction of clusters with RHs in the two mass bins for different values of M_{lim} , finding that f_{RH} drops in the LM bin, specifically it is $\approx 60 - 80\%$ in the HM bin and $\approx 20 - 30\%$ in the LM one. We find that the value of M_{lim} that maximizes the drop in f_{RH} between the two mass bins is $M_{lim} \approx 8 \times 10^{14} M_{\odot}$, for which $f_{RH} = 30 \pm 19\%$ (1σ Poissonian errors) in the LM bin and $f_{RH} = 79 \pm 24\%$ in the HM bin. In order to understand whether the measured drop is statistically significant, we carried out Monte Carlo simulations. Specifically, we randomly assigned the 23 RHs among the 54 clusters of the sample and obtained the distributions of RHs in the two mass bins (after 10^5 trials), expected in the case that RHs were distributed independently of the cluster mass. We found that for $M_{lim} \approx 8 \times 10^{14} M_{\odot}$ the observed f_{RH} in the two mass bins differs from that obtained by the Monte Carlo analysis at 3.2σ . This means that the probability to

obtain by chance the observed drop of f_{RH} is $< 8 \times 10^{-4}$, thus highlighting the statistical significance of our results and suggesting that the increase of the occurrence of RHs with the cluster mass is real, rather than casual.

In Chapter 6 we also studied the distribution of clusters in the morphological diagrams ($c - w$, $c - P_3/P - 0$ and $w - P_3/P_0$). In line with earlier studies (Cassano et al. 2010), we found that RHs are hosted by merging clusters while clusters without RHs are relaxed, thus highlighting the fundamental role of merging in the formation of RHs.

In Chapter 7 we compare our statistical measurements of the occurrence of RHs as a function of the cluster mass with the formation probability of giant RHs, derived in the framework of the turbulent re-acceleration model. Specifically, following Cassano & Brunetti (2005), we used a statistical semi-analytical method to follow (i) the hierarchical evolution of galaxy clusters through mergers, (ii) the injection of turbulence during these mergers and (iii) the ensuing acceleration of relativistic particles, which in turn produces the synchrotron emission in the form of RHs. This method relies on the extended Press & Schechter theory (Lacey & Cole, 1993), that, starting from a cluster with mass M_0 at $z = 0$, allows to follow, back in time, the merging histories (merger trees) of galaxy clusters through Monte Carlo methods. These calculations allow to derive the statistical properties of RHs in the framework of the turbulent re-acceleration scenario, assuming that a fraction, η_t , of the PdV work done by the infalling subclusters during mergers, is channelled into magnetosonic waves that in turn accelerate relativistic particles. In order to compare our observational results with the theoretical evolution of f_{RH} with the cluster mass, we ran these calculations in the redshift range of our sample $z = 0.08 - 0.33$ and considered clusters with $M_0 > 6 \times 10^{14} M_\odot$. We assumed $\eta_t = 0.2$, a scaling between the magnetic field and the cluster mass $B = \langle B \rangle \times (M/\langle M \rangle)^b$, with $\langle B \rangle = 1.9 \mu\text{G}$, $\langle M \rangle = 1.6 \times 10^{15} M_\odot$ and $b = 1.5$ (see Cassano, Brunetti & Setti, 2006 and Chapter 3 for details). The choice of model parameters is made for consistency with previous calculations in the literature (Cassano et al. 2006, 2010, 2012). Results are not expected to substantially change for different choice of parameters (Cassano et al. 2008). We found that the observed drop in the occurrence of RHs towards the low mass bin is in good agreement with the derived theoretical expectations.

Despite the results discussed above support the hypothesis that RHs trace turbulent regions in merging clusters, future efforts are still needed to achieve a full understanding of the statistical properties of RHs in galaxy clusters.

To complete our study, namely to have a mass-complete sample, it is necessary to observe the remaining 14 clusters (see Tab 5.3 in Chapter 5) in the $z = 0.2 - 0.33$ sample without radio information. In this respect, GMRT and VLA proposals have already been submitted to ask for observations of the remaining clusters, which, added to the sample, would allow to reach a 80% completeness and to firmly prove the presence of a drop of f_{RH} also in this redshift range. Furthermore, a crucial expectation of the turbulent re-acceleration scenario is that f_{RH} should further drop

for even smaller systems, however, none statistical information is currently available for clusters with $M < 6 \times 10^{14} M_{\odot}$. We started to explore the statistical properties of RHs in smaller systems at lower redshift by means of Square Kilometre Array (SKA) precursors. In particular, we asked and obtained time to observe clusters with $M > 4 \times 10^{14} M_{\odot}$ in the redshift range $z = 0.05 - 0.1$ with KAT-7 (a precursor of MeerKAT in South Africa) at 1.9 GHz and with The Murchison Widefield Array (MWA, in Australia) between 40 and 90 MHz. These observations would allow to study the occurrence of RHs in the local Universe and in a still unexplored mass range.

Finally, future observations will be fundamental to test the theoretical predictions on the occurrence of RHs at low frequency. Indeed the fraction of clusters with RHs at low observational frequency is expected to increase substantially (Cassano et al. 2010). Low-Frequency Array (LOFAR) follow up observations of our sample could allow to test this prediction. Moreover, merging galaxy clusters which do not show diffuse emission at \sim GHz frequency are ideal candidate to search for the presence of the USSRH with LOFAR.

The results of this Thesis have been presented at two International Conferences:

- “Metrewavelength Sky Conference” in Pune (India), December 2013
 Poster: *Radio Halos in a mass-selected sample of Galaxy Clusters*
 Authors: V. Cuciti, R. Cassano, R. Kale, D. Dallacasa, L. Gregorini
 Conference Proceeding to be published in the Bulletin of the Astronomical Society of India
- “Transformational science with the SKA”, Stellenbosch, South Africa, February 2014
 Poster: *Statistics of RHs in Galaxy Clusters: a test for theoretical models*
 Authors: V. Cuciti, R. Cassano, R. Kale, D. Dallacasa, L. Gregorini

Bibliography

- [1] Abell GO. 1958, *Ap. J. Suppl.* 3:211-278
- [2] Abell GO, 1965 *ARA&A* 3, 1
- [3] Abell GO, Corwin HGJr, Olowin RP. 1989, *Ap. J. Suppl.* 70:1-138
- [4] Aleksić, J., Antonelli, L. A., Antoranz, P. et al. 2010, *ApJ*, 710, 634
- [5] Andersson, K.E. & Madejski, G.M. 2004, *ApJ*, 607, 190
- [6] Angulo, R.E., Springel, V., White, S. D. M. et al. 2012, *MNRAS*, 426, 2046
- [7] Arnaud, M., Maurogordato, S., Slezak, E., Rho, J. 2000, *A&A*, 355, 461
- [8] Arnaud, M., Pointecouteau, E., Pratt, G.W. 2005, *A&A*, 441, 393
- [9] Ascasibar, Y. & Markevitch, M. 2006, *ApJ*, 650, 102
- [10] Bartelmann, M. 2003, *Astronomical Society of the Pacific Conference Series*, 301, 255
- [11] Basu, K. 2012 *MNRAS*, 421L, 112
- [12] Bauer, F. E., Fabian, A. C., Sanders, J. S., Allen, S. W., Johnstone, R. M. 2005, *MNRAS*, 359, 1481
- [13] Bautz, L. P., & Morgan, W. W. 1970, *ApJ*, 162, L149
- [14] Bennett, C. L. et al. 1996, *ApJ*, 464, L1
- [15] Beresnyak, A., Xu, H., Li, H., Schlickeiser, R. 2013, *ApJ*, 771, 131
- [16] Berezhinsky, V. S., Blasi, P., Ptuskin, V. S. 1997, *ApJ*, 487, 529
- [17] Bîrzan, L., Rafferty, D. A., McNamara, B. R., Carilli, C. L., Wise, M. W., Nulsen, P. E. J. 2004, *ApJ*, 607, 800
- [18] Blasi, P. & Colafrancesco, S. 1999, *Astroparticle Physics*, 12 169

- [19] Blasi, P. 2000, ApJ Letter, 532, L9
- [20] Blasi, P. 2001, APh, 15, 223
- [21] Bonafede, A., Govoni, F., Feretti, L., Murgia, M., Giovannini, G., Brüggén, M. 2011, A&A, 530, 24
- [22] Bonafede, A., Feretti, L., Murgia, M. et al. 2012, A&A 513, A30
- [23] Bonafede, A., Vazza, F., Brüggén, M. et al. 2013, MNRAS, 429, 3564
- [24] Bond, J. R., Cole, S., Efstathiou, G., Kaiser, N. 1991, ApJ, 379, 440
- [25] Böhringer, H., Briel, U. G., Schwarz, R. A., Voges, W., Harner, G., Trümper, G. 1994, Nature, 368, 828
- [26] Böhringer, H., Schuecker, P., Guzzo, L. et al. 2004, A&A, 425, 367
- [27] Böhringer, H., Pratt, G. W., Arnaud, M., Borgani, S., Croston, J. H. 2010, A&A, 514, 32
- [28] Bower, R. G. 1991, MNRAS, 248, 332
- [29] Briel, U. G. et al. 1991, A&A, 246, L10
- [30] Brown, S., Emerick, A, Rudnick, L., Brunetti, G. 2011, ApJ, 740, L28
- [31] Brüggén, M., Ruszkowski, M., Simionescu, A., Hoeft, M., Dalla Vecchia, C. 2005, ApJ Letter, 631, L21
- [32] Brüggén, M., Bykov, A., Ryu, D., Röttgering, H. 2012, Space Science Reviews, 166, 187
- [33] Brunetti G. et al. 2001, MNRAS, 320, 365
- [34] Brunetti G. 2003, Astronomical Society of the Pacific Conference Series, 301, 349
- [35] Brunetti, G., Mack, K.-H., Prieto, M. A., Varano, S. 2003, MNRAS.345.40
- [36] Brunetti, G., Blasi, P., Cassano, R., Gabici, S. 2004, MNRAS, 350, 1174
- [37] Brunetti G. & Blasi, P. 2005, MNRAS 363, 1173
- [38] Brunetti G. & Lazarian, A. 2007, MNRAS, 378, 245
- [39] Brunetti G., Venturi, T., Dallacasa, D., Cassano, R., Dolag K., Giacintucci, S., Setti, G., 2007, ApJ Letter, 670, L5

- [40] Brunetti G., Giacintucci, S., Cassano, R. et al. 2008, *Nature*, 455, 944
- [41] Brunetti G., Cassano, R. Dolag, K., Setti, G. 2009, *A&A*, 507, 661
- [42] Brunetti G., Lazarian, A. 2011, *MNRAS*, 410, 127
- [43] Brunetti G. & Jones, T. W. 2014, arXiv 1401, 7519B
- [44] Buote, D. A. & Tsai, J. C. 1995, *ApJ*, 452, 522
- [45] Buote, D. A. & Tsai, J. C. 1996, *ApJ*, 458, 27
- [46] Buote, D. A. 2001, *ApJ*, 553, 15
- [47] Burns, J. O., Sulkanen, M. E., Gisler, G. R., Perley, R. A. 1992, *ApJ*, 388, L49
- [48] Carilli, C.L., Taylor, G.B., 2002, *ARA&A*, 40, 319
- [49] Carlstrom, J. E., Holder, G. P., Reese, E. D. 2002, *ARA&A*, 40, 643
- [50] Carrol, S. M., Press, W. H., Turner, E. L. 1992, *ARA&A* 30, 499
- [51] Cassano R., Brunetti, G., Setti, G. 2004, *JKAS*, 37, 589
- [52] Cassano R. & Brunetti G. 2005, *MNRAS*, 357, 1313 (CB05)
- [53] Cassano R., Brunetti, G., Setti, G., 2006, *MNRAS*, 369, 1577 (CBS06)
- [54] Cassano, R., Brunetti, G., Venturi, T., Setti, G., Dallacasa, D., Giacintucci, S., Bardelli, S. 2008, *A&A* 480, 687
- [55] Cassano, R., Gitti, M., Brunetti, G. 2008, *A&A*, 486, L31
- [56] Cassano, R., Etti, S., Giacintucci, S., Brunetti, G., Markevitch, M., Venturi, T., Gitti, M. 2010, *ApJL*, 721: L82-L85
- [57] Cassano, R., Brunetti, G., Röttgering, H. J. A., Brüggem, M. 2010, *A&A*, 509, A68
- [58] Cassano, R., Brunetti, G., Venturi, T. 2011, *JApA*, 32, 519
- [59] Cassano, R., Brunetti, G., Norris, R.P., Röttgering, H. J. A., Johnston-Hollit, M., Trasatti, M. 2012, *A&A*, 548, A100
- [60] Cassano, R., Etti, S., Brunetti, G., Giacintucci, S., Pratt, G. W. et al. 2013, *ApJ*, 777, 141
- [61] Cavaliere, A. & Fusco-Femiano, R. 1976, *A&A*, 49, 137

- [62] Cho, J., Lazarian, A., Honein, A., Knaepen, B., Kassinos, S., Moin, P. 2003, ApJ, 589L, 77
- [63] Clarke, T. E. & Enßlin, T. A. 2006, Astronomical Journal, 131, 2900
- [64] Cole, S. 1991, ApJ, 367, 45
- [65] Cole, S., Aragon-Salamanca, A., Frenk, C. S., Navarro, J. F., Zepf, S. E. 1994, MNRAS, 271, 781 1994, MNRAS, 271, 781
- [66] Coles, P. & Lucchin, F. 1995. *Cosmology. The origin and evolution of cosmic structure*, Chichester: UK: Wiley
- [67] Condon, J. J., Cotton, W. D., Greisen, E. W., Yin, Q. F. et al. 1998, AJ, 115, 1693
- [68] Dallacasa, D., Brunetti, G., Giacintucci, S., Cassano, R. et al. 2009, ApJ, 699, 1288-1292
- [69] Da Silva, A. J. C. 2004, Ap&SS, 290, 167
- [70] Davis, M., Efstathiou, G., Frenk, C. S., White, S. D. M. 1985, ApJ, 302, L1
- [71] Deiss, B. M., Reich, W., Lesch, H. Wielebinski, R. 1997, A&A, 321, 55
- [72] Dennison, B. 1980, ApJ 239
- [73] Dermer, C. D. 1986, ApJ, 307, 47
- [74] Dolag, K., Bartelmann, M., Lesch, H. 1999, A&A, 348, 351
- [75] Dolag, K., Schindler, S., Govoni, F., Feretti, L. 2001, A&A, 378, 777
- [76] Dolag, K., Bartelmann, M., Lesch, H. 2002, A&A, 387, 383
- [77] Dolag, K., Bartelmann, M., Perrotta, F., Baccigalupi, C., Moscardini, L., Meneghetti, M., Tormen, G. 2004, A&A, 416, 853
- [78] Dolag, K., Grasso, D., Springel, V., Tkachev, I. 2005, JCAP, 1,9
- [79] Domainko, W., Kapferer, W., Gitti, M., Schindler, S., van Kampen, E. et al. 2004, bdmh confE, 74
- [80] Donnert, J., Dolag, K., Cassano, R., Brunetti, G. 2010, MNRAS, 407, 1565
- [81] Donnert, J., Dolag, K., Brunetti, G., Cassano, R. 2013, MNRAS.429.3564
- [82] Ebeling, H., Voges, W., Böringer, H., Edge, A. C., Huchra, J. P., Briel, U. G. 1996, MNRAS, 281, 799

- [83] Eilek, J. A. 1979, *ApJ*, 230, 373
- [84] Enßlin, T. A., Biermann, P. L., Kronberg, P. P., Wu, X-P. 1997, *ApJ*, 477, 560
- [85] Enßlin, T. A. & Röttgering, H. 2002, *A&A*, 396, 83
- [86] Enßlin, T. A., Pfrommer, C., Miniati, F., Subramanian, K. 2011, *A &A*, 527, 99
- [87] Fabian, A. C. 1994, *ARA&A*, 32, 277
- [88] Fabian, A. C., Celotti, A., Blundell, K. M., Kassim, N. E., Perley, R. A. 2002, *MNRAS*, 331, 369
- [89] Fabian, A. C., Sanders, J. S., Crawford, C. S., Conselice, C. J., Gallagher, J. S., Wyse, R. F. G. 2002, *MNRAS*, 344, L8
- [90] Fall, S. M., & Efstathiou, G. 1980, *MNRAS*, 193, 189
- [91] Feretti, L., Orrù, E., Brunetti, G., Giovannini, G. Kassim, N, Setti, G. 2004, *A&A*, 423, 111
- [92] Feretti, L. 2005, X-ray and Radio Connections (eds L.O. Sjouwerman and K.K Dyer) Published electronically by NRAO, <http://www.aoc.nrao.edu/events/xraydio> Held 3-6 February 2004 in Santa Fe, New Mexico, USA, (E8.02) 10 pages
- [93] Feretti, L., Giovannini, G., Govoni, F., Schindler, S., Bykov, A. M., Rephaeli, Y. 2008, *Space Science Reviews*, 134, 93
- [94] Feretti, L., Giovannini, G., Govoni, F., Murgia, M. 2012, *A&ARv*, 20, 54
- [95] The FERMI-LAT Collaboration: Ackermann, M. et al. 2013, *ApJ*, 209, 34
- [96] The FERMI-LAT Collaboration: Ackermann, M. et al. 2013, arXiv: 1308.6278
- [97] Ferrari, C., Maurogordato, S., Cappi, A., Benoist, C., 2003, *A&A*, 399, 813
- [98] Fujita, Y, Takizawa, M., Sarazin, C. L. 2003, *ApJ*, 584, 190
- [99] Furlanetto, S. R. & Loeb, A. 2001, *ApJ*, 556, 619
- [100] Fusco-Femiano, R., Dal Fiume, D., Feretti, L., Giovannini, G., Grandi, P., Matt, G., Molendi, S., Santangelo, A. 1999, *ApJ*, 513, L21
- [101] Fusco-Femiano, R., Orlandini, M., Brunetti, G., Feretti, L., Giovannini, G., Grandi, P., Setti, G. 2004, *ApJ*, 602, 73
- [102] Gabici, S., Blasi, P. 2003, *ApJ*, 583, 695

- [103] Gehrels, N. 1986, ApJ 303, 336
- [104] Giacintucci, S. Venturi, T., Brunetti, G., Bardelli, S. et al. 2005, A&A, 440, 867
- [105] Giacintucci, S. Venturi, T., Macario, G., et al. 2008, A&A, 486, 347
- [106] Giacintucci, S., Markevitch, M. Brunetti, G. Cassano, R. Venturi, T. 2011, A&A, 525L, 10G
- [107] Giovannini, G., Feretti, L., Venturi, T., Kim, K.-T., Kronberg, P. P. 1993, ApJ, 406, 399
- [108] Giovannini, G., Tordi, M., Feretti, L. 1999, NewA 4, 141
- [109] Giovannini, G. & Feretti, L. 2004, Journal of Korean Astronomical Society, 37, 323
- [110] Giovannini, G., Bonafede, A., Feretti, L., et al. 2009, A&A, 507, 1257
- [111] Giovannini, G., Feretti, L., Girardi, M., et al. 2011, A&A, 530, L5
- [112] Gitti, M., Brunetti, G., Setti, G. 2002, A&A, 386, 456
- [113] Govoni, F., Feretti, L., Giovannini, G., Böhringer, H, et al. 2001, A&A, 369, 441
- [114] Govoni, F., Markevitch, M., Vikhlinin, A., VanSpeybroeck, L. Feretti, L., Giovannini, G. 2004, ApJ, 605, 695
- [115] Govoni, F., Murgia, M., Feretti, L., Giovannini, G., Dolag, K., Taylor, G. B. 2006, A&A, 460, 425
- [116] Guidetti, D., Murgia, M., Govoni, F., Parma, P., Gregorini, L., De Ruiter, H. R., Cameron, R. A., Fanti, R. 2008, A&A, 483, 699
- [117] Hanish, R. J., 1982, Astron. Astrophys., 111, 97
- [118] Henriksen, M., Donnely, R. H., Davis, D. S. 2000, ApJ, 529, 692
- [119] Hoeft, M., Brüggén, M. Tepes, G., Gottlöber, S., Schwöpe, A. 2008, MNRAS, 391, 1511
- [120] Huber, B., Tchernin, C., Eckert, D. et al. 2013, arXiv: 1308.6278
- [121] Hwang, C.-Y. 2004, JKAS 37, 461
- [122] Jaffe, W. J. 1977, ApJ, 212, 1

- [123] Jeltema, T. E., Canizares, C.R., Bautz, M.W., Buote, D.A. 2005, ApJ, 624, 606
- [124] Kaiser, N. 1986, MNRAS, 222, 323
- [125] Kale et al. 2013, A&A 557, 99
- [126] Kang, H. & Ryu, D. 2011, ApJ, 734, 18
- [127] Kang, H., Ryu, D., Jones, T. W., 2012, ApJ, 756, 97
- [128] Katz, N., Weinberg, D. H., Hernquist, L. 1996, ApJS, 105, 19
- [129] Kauffmann, G., White, S. D. M., Guiderdoni, B. 1993, MNRAS, 264, 201
- [130] Kempner, J. C. & Sarazin, C. L. 2001, ApJ, 548, 639
- [131] Keshet, U. & Loeb, A. 2010, ApJ, 722, 737
- [132] Kim, K. T., Kronberg, P. P., Dewdney, P. E., Landecker, T. L. 1990, ApJ, 355, 29
- [133] Kitayama, T. & Suoto, Y. 1996, ApJ, 469, 480
- [134] Kulsrud, R. M., Cen, R., Ostriker, J. P., Ryu, D. 1997, ApJ, 480, 481
- [135] Lacey, C. & Cole, S. 1993, MNRAS, 262, 627
- [136] Liang, H., Hunstead, R. W., Birkinshaw, M., Andreani, P. 2000, ApJ, 544, 686
- [137] Macario, G., Venturi, T., Brunetti, G., Dallacasa, D., Giacintucci, S. et al. 2010, A&A, 517, A43
- [138] Marghegiani, P., Perola, G. C., Colafrancesco, S. 2007, A&A, 465, 41
- [139] Markevitch, M., Sarazin, C. L., Vikhlinin, A. 1999, ApJ, 521, 526
- [140] Markevitch, M. & Vikhlinin, A. 2001, ApJ, 563, 95
- [141] Markevitch, M., Govoni, F., Brunetti, G., Jerius, D., 2005, ApJ, 627, 733
- [142] Markevitch, M. 2006, in “The X-ray Universe 2005”, September
- [143] Maughan, B. J., Jones, L. R., Pierre, M., Andreon, S., Birkinshaw, M., Bremer 2008, MNRAS, 387, 998
- [144] Maughan, B.J., Giles, P. A., Randall, S. W., Jones, C., Forman, W.R. 2012, MNRAS, 421, 1583

- [145] Mazzotta et al. 2001, *Memorie della Società Astronomica Italiana*, V82, 495
- [146] Mazzotta, P., Markevitch, M., Forman, W.R., Jones, C., Vikhlinin, A., VanSpeybroeck, L. 2001, *astro-ph*, 8476
- [147] Mazzotta, P. & Giacintucci, S. 2008, *ApJ*, 675, L9
- [148] Melrose, D. B. 1968, *ApSS* 2, 171
- [149] Melrose, D. B. 1980, *Plasma astrophysics. Nonthermal processes in diffuse magnetized plasmas*, New York: Gordon and Breach
- [150] Miniati, F., Ryu, D., Kang, H., Jones, T. W. 2001, *ApJ*, 559, 59
- [151] Miniati, F. 2003, *MNRAS*, 342, 1009
- [152] Mohr, J. J., Fabricant, D. G., Geller, M. J. 1993, *ApJ*, 413, 492
- [153] Murgia, M., Govoni, F., Feretti, L., Giovannini, G., Dallacasa, D., Fanti, R., Taylor, G. B., Dolag, K 2004, *A&A*, 424, 429
- [154] Murgia, M., Govoni, F., Markevitch, M. et al. 2009, *A&A* 499, 679
- [155] Nagai, D. 2006, *ApJ*, 650, 538
- [156] O'Hara, T. B., Mohr, J. J., Bialek, J. J., Evrard, A. E. 2006, *ApJ*, 639, 640
- [157] Orrù, E., Murgia, M., Feretti, L., Govoni, F., Brunetti, G. et al. 2007, *A&A*, 467, 943
- [158] Owen, F. N., Eilek, J. A., Kassim, N. E. 2000, *ApJ*, 543, 611
- [159] Petrosian, V. 2001, *ApJ*, 557, 560
- [160] Petrosian, V., Bykov, A., Rephaeli, Y. 2008, *Space Science Reviews*, 134, 191
- [161] Pfrommer, C. & Enßlin, T. A. 2004, *MNRAS*, 352, 76
- [162] Pfrommer, C., Springel, V., Enßlin, T. A., Jubelgas, M. 2006, *MNRAS*, 367, 113
- [163] Pfrommer, C., Enßlin, T. A., Springel V. 2008, *MNRAS*, 385, 1211
- [164] Pfrommer, C. 2008, *MNRAS*, 385, 1242
- [165] Planck Collaboration, 2011, *A&A*, 536, A8
- [166] Planck Collaboration, 2011, *A&A*, 536, 9
- [167] Planck Collaboration, 2011, *A&A*, 536A, 10P

- [168] Planck Collaboration, 2012, *A&a*, 543, 102
- [169] Planck Collaboration 2013, *A&A*, 550, 130
- [170] Planck Collaboration 2013, arXiv:1303.5089
- [171] Poole, G. B., Fardal, M. A., Babul, A., McCarthy, I. G., Quinn, T., Wadsley, J. 2006, *MNRAS*, 373, 881
- [172] Poole, G. B., Babul, A., McCarthy, I. G., et al. 2007, *MNRAS*, 380, 437
- [173] Pratt, G.W., Croston, J.H., Arnaud, M., Böhringer, H. 2009, *A&A*, 498, 361
- [174] Press W.H. & Schechter P. 1974, *ApJ* 187, 425
- [175] Pzinke, A. & Pfrommer, C. 2010, *MNRAS*, 409, 449
- [176] Pzinke, A., Pfrommer, C., Bergström, L. 2011, *Physical Review D*, 84, 123509
- [177] Randall, S. W., Sarazin, C. L., Ricker, P. M. 2002, *ApJ*, 577, 579
- [178] Reimer, A., Reimer, O., Schlickeiser, R., Iyudin, A. 2004, *A&A*, 424, 773
- [179] Reiprich, T. H. and Böhringer, H. 2002, *ApJ*, 567, 716
- [180] Rephaeli, Y., Gruber, D., Blanco, P. 1999, *ApJL*, 511, 21
- [181] Rephaeli, Y. & Gruber, D. 2002, *ApJ*, 579, 587
- [182] Ricker, P. M., Sarazin, C. L., 2001, *ApJ*, 561, 621
- [183] Röttgering, H. J. A., Wieringa, M. H., Hunstead, R. W., Ekers, R. D. 1997, *MNRAS*, 290, 577
- [184] Röttiger, K., Burns, J. O., Stone, J. M. 1999, *ApJ* 518, 603
- [185] Ryu, D., Kang, H., Biermann, P. L. 1998, *A&A*, 335, 19
- [186] Ryu, D., Kang, H., Hallmann, E., Jones, T. W. 2003, *ApJ*, 593, 599
- [187] Rudnick, L., Delain, K.M., Rawlings, S., Brand, K., Blundell, K. 2005, *AAS*, 206, 1011
- [188] Rudnick, L., Delain, K. M., Lemmerman, J. A. 2006, *Astronomische Nachrichten*, 327, 549
- [189] Santos, J.S., Rosati, P., Tozzi, P., Böhringer, H., Ettori, S., Bignamini, A. 2008, *A&A*, 483, 35
- [190] Sarazin, C. L. 1986, *Reviews of Modern Physics* 58, 1

- [191] Sarazin, C. L. 1999, ApJ, 520, 529
- [192] Sarazin, C. L. 2002, ASSL, 272, 1
- [193] Schlickeiser, R., Sievers, A., Thiemann, H. 1987, A&A, 182, 21
- [194] Schlickeiser, R. & Miller, J. A. 1998, ApJ, 492, 352
- [195] Schlickeiser, R. 2002, *Cosmic Ray Astrophysics*, Springer-Verlag, Berlin Heidelberg
- [196] Schuecker, P., Böringer, H., Reiprich, T. H., Feretti, L. 2001, A&A, 378, 408
- [197] Sheth, R. K. & Tormen, G. 1999, MNRAS, 308, 119
- [198] Sijbring, L. G. 1993, PhD Thesis, University of Groningen
- [199] Smith S. 1936, ApJ, 83, 23
- [200] Sommer, M. W., Basu, K. 2014, MNRAS, 437, 2163
- [201] Springel, V. 2005, MNRAS, 364, 1105
- [202] Springel, V. et al. 2005, Nature, 435, 629
- [203] Steinmetz, M. & Muller, E. 1995, MNRAS, 276, 549
- [204] Subramanian, K., Shukurov, A., Haugen, N. E. L. 2006, MNRAS, 373, L65
- [205] Takahashi, T., Mitsuda, K., Kelley, R. et al. 2010, Proceeding of the SPIE, 7732, 77320Z-77320Z-18
- [206] Thierbach, M., Klein, U., Wielebinski, R. 2003, A&A, 397, 53
- [207] Tormen, G., Moscardini, L., Yoshida, N. 2004, MNRAS, 350, 1397
- [208] Tribble, P. C. 1989, MNRAS, 238, 1247
- [209] Vacca, V., Murgia, M., Govoni, F. et al. 2012, A&A, 540, A38
- [210] Valtchanov, I., Murphy, T., Pierre, M., Hunstead, R., Lémonon, L. 2002, A&A, 392, 795
- [211] van Weeren, R. J., Röttgering, H. J. A., Brüggén, M., Hoeft, M. 2010, Science, 330, 347
- [212] van Weeren, R. J., Fogarty, K., Jones, C., Forman, W. R., Clarke, T.E., Brüggén, M., Kraft, R.P. et al. 2013, ApJ, 769, 101

- [213] Vazza, F., Tormen, G., Cassano, R., Brunetti, G., Dolag, K. 2006, MNRAS, 369, L14
- [214] Ventimiglia, D. A., Voit, G. M., Donahue, M., Ameglio, S. 2008, ApJ, 685, 118
- [215] Venturi, T., Giacintucci, S., Brunetti, G., Cassano, R. et al. 2007, A&A 463, 937 (V07)
- [216] Venturi, T., Giacintucci, S., Dallacasa, D., Cassano, R., Brunetti, G. et al. 2008, A&A, 484, 327 (V08)
- [217] Venturi, T. 2011, MmSAI, 82, 499
- [218] Venturi, T., Giacintucci, S., Dallacasa, D., Cassano, R., Brunetti, G. et al. 2013, A&A, 551A, 24
- [219] Vogt, C. & Enßlin, T.A. 2005, A&A, 434, 67
- [220] Voigt, L. M., Schmidt, R. W., Fabian, A. C., Allen, S. W., Johnstone, R. M. 2002, MNRAS, 335L, 7
- [221] Völk, H. J., Aharonian, F. A., Breitschwerdt, D. 1996, SSRv 75, 279
- [222] Völk, H. J., & Atoyan, A. M. 1999 Astroparticle Physics, 11, 73
- [223] Völk, H. J., & Atoyan, A. M. 2000, ApJ, 541, 88
- [224] White, S.D.M. & Frenk, C.S. 1991, ApJ, 379, 52
- [225] White, S.D.M. & Rees, M. J. 1978, MNRAS, 183, 341
- [226] Wik, D.R., Sarazin, C. L., Ricker, P. M., Randall, S.W. 2008, ApJ, 680, 17
- [227] Wik, D. R., Sarazin, C. L., Finoguenov, A. et al. 2011, ApJ, 727, 119
- [228] Willson, M. A. G. 1970, MNRAS, 151, 1
- [229] Zandanel, F., Pfrommer, C., Prada, F. 2014, MNRAS, 438, 116
- [230] Zhang, Y.-Y., Andernach, H., Caretta, C. A., et al. 2011, A&A, 526, A105
- [231] Zhuravleva, I., Churazov, E., Kravtsov, A., Sunyaev, R. 2012, MNRAS, 422, 2712
- [232] ZuHone, J.A., Markevitch, M., Johnson, R. E. 2010, ApJ, 717, 908
- [233] ZuHone, J.A., Markevitch, M., Lee, D. 2011, ApJ, 743, 16

- [234] ZuHone, J.A., Markevitch, M., Brunetti, G., Giacintucci, S. 2013, ApJ, 762, 78
- [235] Zwicky F. 1933, Helv. Phys. Acta, 6, 110
- [236] Zwicky F. 1937, ApJ 86:217-246
- [237] Zwicky F., Herzog, E., Wild, P. 1961, *Catalogue of galaxies and of clusters of galaxies*, Vol. 1 Pasadena: California Institute of Technology
- [238] Zwicky F., Herzog, E., Wild, P. 1966, *Catalogue of galaxies and of clusters of galaxies*, Pasadena: California Institute of Technology
- [239] Zwicky F.& Kowal, C. T. 1968, *Catalogue of galaxies and of clusters of galaxies*, Volume VI Pasadena: California Institute of Technology